UNIVERSITY OF CALGARY

Near-surface Characterization Using Seismic Refraction and Surface-wave Methods

by

Khaled Al Dulaijan

A THESIS
SUBMITTED TO THE FACULTY OF GRADUATE STUDIES
IN PARTIAL FULFILMENT OF THE REQUIREMENTS FOR THE
DEGREE OF MASTER OF SCIENCE

DEPARTMENT OF GEOSCIENCE
CALGARY, ALBERTA
SEPTEMBER, 2008

UNIVERSITY OF CALGARY

FACULTY OF GRADUATE STUDIES

The undersigned certify that they have read, and recommend to the Faculty of Graduate Studies for acceptance, a thesis entitled " Near-surface Characterization Using Seismic Refraction and Surface-wave Methods " submitted by Khaled Al Dulaijan in partial fulfilment of the requirements of the degree of Master of Science.

Supervisor, Dr. R. R. Stewart
Department of Geoscience

Dr. D. W. Eaton
Department of Geoscience

Dr. R. D. Jacobson
Department of Geography

Date

ABSTRACT

Varying thicknesses and velocities of near-surface layers cause serious problems for seismic reflection imaging of the deeper subsurface. Static corrections, calculated from near-surface velocity models, are used to remove the effects of the variable topographic near surface. In this thesis, near-surface layers are studied and characterized using two methods: Generalized Linear Inversion (GLI) of first arrival times and Multi-channel Analysis of Surface Waves (MASW). The first is a widely used and proven method for obtaining near-surface velocity models for both P and S waves. The second is mainly used for geotechnical engineering purposes and is based on the dispersion properties of Rayleigh waves.

Two sites (at the Rothney Observatory and Spring Coulee, Alberta) are investigated. In the Rothney case, the S-wave velocities of the near surface (obtained by the MASW method) range from 200 to 1200 m/s and roughly correlate to the lithology log of a well drilled on site. In Spring Coulee, the S-wave near-surface models (obtained by GLI of first arrival times method) had different velocity layering and base of weathering from those of P waves. The MASW S-wave velocity model of Spring Coulee, Alberta correlates well to the GLI model. P-wave velocities range from 900 to 3600 m/s, while S-wave velocities range from 420 to 1966 m/s. Static corrections are calculated using near-surface models and are applied prior to stacking of PP and PS data. P-wave static corrections range from -25 ms to 27 ms, and those for S-wave range from -65 ms to 12 ms.

ACKNOWLEDGEMENTS

For his creative thoughts, inspiration, guidance, and encouragement, my sincere gratitude goes to my supervisor Dr. Robert R. Stewart. I also would like to thank my instructors Dr. Gary F. Margrave, Dr. Laurence R. Lines, Dr. John C. Bancroft, and Dr. Ed Krebes for teaching courses that made this project easier. I also would like to thank Dr. Joe Wong and Mark Kirtland for proofreading this thesis. For solving all system-related issues, I would like to extend my gratitude to Kevin Hall and Dr. Rolf Maier. I am thankful to Han-Xing Lu, and Dr. Helen Isaac for their help with ProMAX. Also, I would like to thank Dr. Peter Manning and Louise Forgues from CREWES project. Also, I would like to extend my thanks to my fellow students at the Department of Geoscience: Mohammed Al-Duhailan, Salman Bubshait, Abdulla Al-Shuhail, Maria Quijada, Michael Hons, Soo-Kyung Miong, and Alejandro Alcudia. Also, I would like to thank all of the staff, students and sponsors of CREWES project.

I extend my gratitude to my Advanced Degree Program mentor at Saudi Aramco Dr. Timothy Keho for valuable advice. From Saudi Aramco, I am thankful to Dr. Panos Kelamis, Dr. Christopher Liner (currently at the University of Houston), and Thierry-Laurent Tonellot for guidance. To the greatest extent, I thank Saudi Aramco for sponsoring my program.

Finally, I would like to thank my wonderful parents and fiancé for prayers, love, and support.

DEDICATION

Without her love, support, and prayers, this work would not be completed, so I dedicate my work to my mother.

TABLE OF CONTENTS

LIST OF FIGURES AND ILLUSTRATION

LIST OF TABLES

LIST OF SYMBOLS, ABBREVIATIONS AND NOMENCLATURE

ρ	Density
λ	Lamé constant
k	Bulk modulus
μ	Shear modulus
V_P and α	P-wave velocity
V_S and β	S-wave velocity
σ	Poisson’s Ratio
U	Particle displacement
t	Time
x	distance
h	Thickness
z	Depth
f	Frequency
λ	Wavelength
V_R	Rayleigh-wave velocity in elastic half space
C	Rayleigh-wave phase velocity
V	Rayleigh-wave group velocity
ω	Angular frequency
p	Slowness
τ	Intercept time
RMS	Root Mean Square
D	Spread length
x_1	Near offset
E	Elevation above sea level
T_k	Model breaks
P_k	Observed breaks
CDP	Common Depth Point
CCP	Common Conversion Point
AGC	Automatic Gain Control
NMO	Normal Moveout
GLI	Generalized Linear Inversion
MASW	Multichannel Analysis of Surface Waves
LVL	Low Velocity Layers
t_{LVL}	LVL static correction
t_E	Elevation static correction
t_{Datum}	Datum static correction
V_{rep}	Replacement velocity
PP	Incident P-wave to reflected P-wave
PS	Incident P-wave to reflected S-wave

CHAPTER ONE: INTRODUCTION AND BACKGROUND

1.1 Near surface and weathering

The ground is often covered with unconsolidated sediments called the weathered layer. Sheriff (1991) defines the weathered layer:

> "A near-surface, low-velocity layer, usually the portion where air rather than water fills the pore spaces of rocks and unconsolidated earth. Seismic weathering is usually different from geologic weathering (the result of rock decomposition). The term LVL (low-velocity layer) is often used for the seismic weathering. Frequently the base of the weathering is the water table. Sometimes the weathering velocity is gradational, sometimes it is sharply layered."

From Sheriff's definition, seismic weathering is related to the velocity of seismic waves in the near surface. Because the velocity of some seismic waves can be relatively high in water, the water table defines boundaries of the weathered layer or the base of weathering. That is generally correct for the P-waves that geophysicists use the most, but not accurate for all types of seismic waves as can be seen in the following pages.

In seismic imaging, the near surface can be a cause of problems since variations in the thicknesses and velocities of the weathered layer can cause large time delays for rays passing through it. As a result, deeper reflections in seismic images may show time structure effects, and that can be misleading for the interpretation of seismic data. Figure 1-1(a) shows a geologic model with two reflectors. The first reflector is the base of the weathered layer. Rays traveling in the weathered layer will be significantly delayed, and the amount of delay will be different for different rays due to variations in the thickness and velocity of the weathered layer. In seismic time sections, the differences in the amount of delay for traces passing through the weathered layer will cause an apparent structural effect on deeper reflection events as shown in Figure 1-1(b). The second reflector might be wrongly interpreted as a syncline if the near-surface problem is not handled properly. Common-midpoint stacking is an effective process, which geophysicists expect to significantly improve the signal-to-noise ratio of the seismic data. Consider again rays traveling through a weathered layer of a varying thickness and velocity as shown in Figure 1-2 (left). After normal moveout (NMO) correction, common midpoint events will not be aligned, and will still have time differences due to differences in vertical ray path times as shown in Figure 1-2 (right). Therefore, common-midpoint stacking will cause distortion, instead of enhancement, in the signal quality (Farrell et al., 1984).

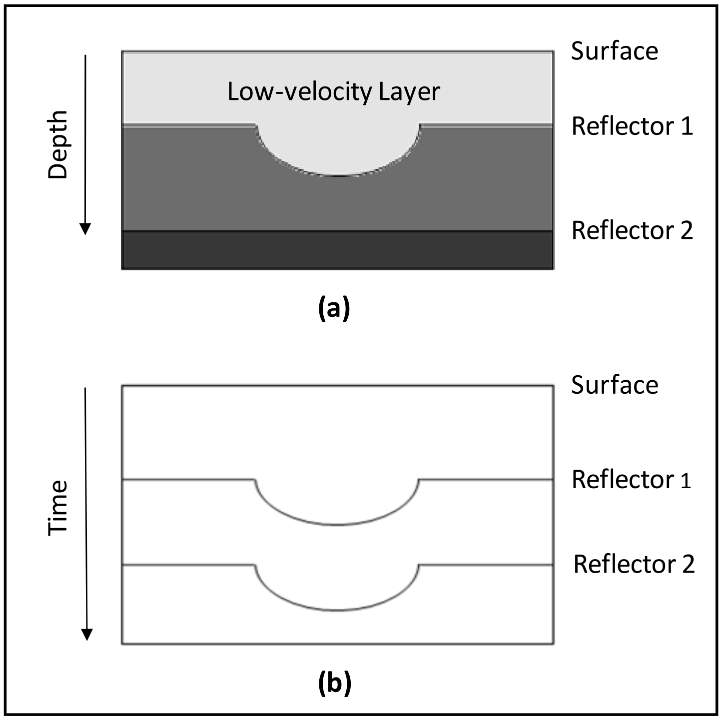

Figure 1-1. (a) Earth model. (b) Seismic time model showing delayed or "pushed down" reflections underneath the near-surface anomalies (modified after Farrell et al., 1984).

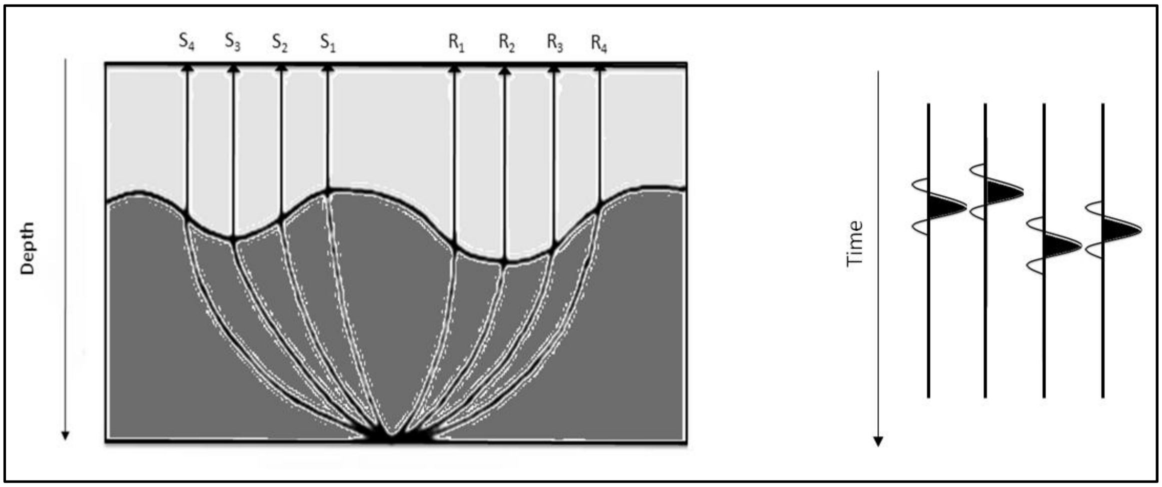

Figure 1-2. Ray paths from shots (S_1, S_2, S_3, and S_4) to receivers (R_1, R_2, R_3, and R_4) of a common depth point (left), and time differences in NMO-corrected events due to differences in vertical ray-path times (right) (modified after Farrell et. al., 1984).

For geophysicists, accurate knowledge of the near surface can be crucial and can significantly upgrade or downgrade the quality of their product. For that reason, it is essential to understand and correctly analyse the near-surface effects.

1.2 Seismic waves and velocity

Seismic energy propagation can be classified into two broad categories: body waves and surface waves. In exploration seismology, body waves are considered signals, while surface waves are usually considered as noise. Body waves are of two types: compressional (P-waves) and shear (S-waves). The upper section of Figure 1-3 shows the wave propagation and the particle motion of P-waves. The particle motion is parallel to the direction of the wave propagation. The P-wave (primary wave) is the fastest of all seismic waves. Sheriff and Geldart (1995) showed that P-wave velocities, V_P, can be derived from Newton's second law of motion and Hooke's law of elasticity. P-wave velocity can be expressed in terms of density (ρ), bulk modulus (k), and shear modulus (μ):

$$V_P = \sqrt{\frac{k + 4/3\mu}{\rho}}\ . \tag{1.1}$$

The bulk modulus can be considered as the incompressibility of the material, and the shear modulus is considered as the rigidity or the resistance of the material to shear. S-waves (secondary or shear waves) are slower than P-waves, and their particle motion are perpendicular to propagation directions. The middle section of Figure 1-3 shows the wave propagation and the particle motion of S-waves. The S-wave velocity, V_S, is expressed as:

$$V_S = \sqrt{\frac{\mu}{\rho}} \tag{1.2}$$

Equation (1.2) shows that the greater the shear modulus, or the more resistant to shear the material is, the greater S-wave velocity. Because fluids have no resistance to shearing, the S-wave velocity is zero in fluids. Therefore, the S-waves are less affected by the water table than P-waves, and the water table does not define the base of weathering for S-waves, as it does for P-waves.

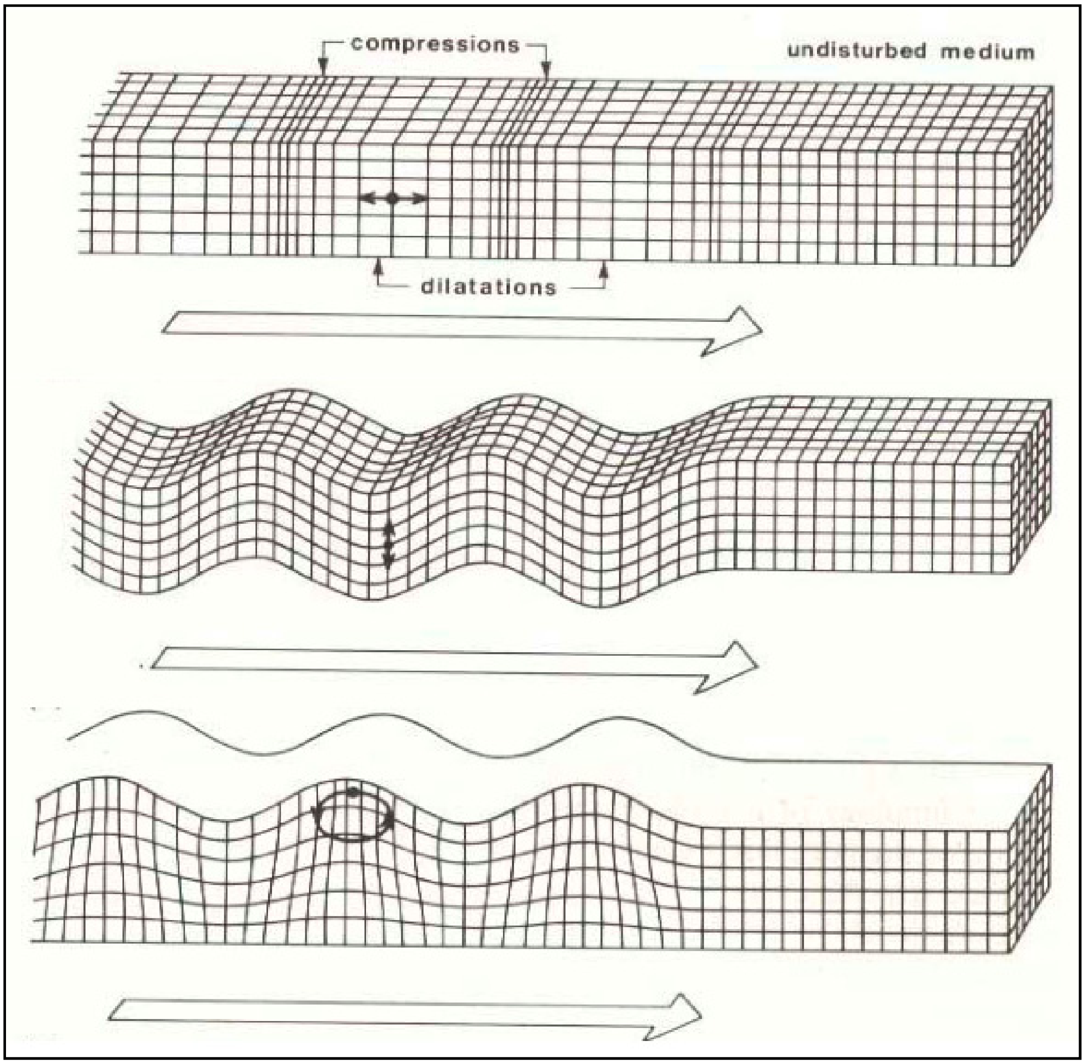

Figure 1-3. Particle motion and wave propagation of P-wave (upper), S-wave (middle), and Rayleigh wave (lower). The large white arrow indicates the direction of wave propagation, and the small black arrow shows particle motion (modified after Brown and Mussett, 1976).

Commonly considered surface waves are generally of two types: Rayleigh waves and Love waves. In this thesis, I only analyse Rayleigh waves. Rayleigh waves propagate along and only in the presence of a free boundary. The particle motion of Rayleigh waves is elliptical in a plane perpendicular to the surface, and retrograde (particle motion is opposite to the propagation direction in the top of its elliptical path). The lower section of

Figure 1-3 shows the wave propagation and the particle motion of Rayleigh waves (Xu, 2004). Some properties of Rayleigh waves are summarized below.

1.2.1 Properties of Rayleigh wave

The Rayleigh wave, named after Lord Rayleigh (1885), can form more than two thirds of the total seismic energy when a P-wave source is used in seismic surveys (Park et al., 1999). Miller and Pursey (1955) showed that 67% of the seismic energy is imparted into Rayleigh waves when vertically vibrating source is used. The particle motion of Rayleigh waves is not as simple as parallel or perpendicular to the direction of propagation, but rather a combination of both forming an elliptical and retrograde motion (Lin, 2007).

The amplitude of Rayleigh waves decreases with distance, *r*, from the source proportional to $\frac{1}{\sqrt{r}}$. On the other hand, the amplitude of body waves decreases more rapidly $(\frac{1}{r})$ with distance from the source than Rayleigh waves. Therefore, Rayleigh waves are more noticeable than body waves at greater distances from the source (Lin, 2007). Rayleigh waves have amplitudes that also decay exponentially with depth from the free surface, but they are believed to be influenced by earth materials at depths up to one wavelength (Xu, 2004).

We are interested in the Rayleigh wave's velocity and, in particular, the velocity change with frequency (dispersion). In the case of an isotropic homogeneous half space, Rayleigh waves are non-dispersive or, in other words, different frequencies travel at the same velocity. However, in a real layered earth, Rayleigh waves are dispersive (velocity is dependent on frequency) with multiple modes. Surface-wave dispersion has been studied by many authors (i.e. Rayleigh, 1887; Sezwa, 1927; Thompson, 1950; Dobrin, 1951; and Haskell, 1953). The dispersion properties of Rayleigh waves can be used to estimate the S-wave velocities of the near-surface earth materials (Pelton, 2005).

1.2.2 Rayleigh- and S-wave velocities

Richart el al. (1970) illustrated the relationship between the velocities of S-waves and Rayleigh waves propagating in an elastic half space as follows:

$$\left(\frac{V_R}{V_s}\right)^6 - 8\left(\frac{V_R}{V_s}\right)^4 + \left(24 - 16\frac{1-2\sigma}{2-2\sigma}\right)\left(\frac{V_R}{V_s}\right)^2 + 16\left(\frac{1-2\sigma}{2-2\sigma} - 1\right) = 0 . \qquad (1.3)$$

Here, V_R is the Rayleigh wave velocity, and σ is the Poisson's ratio given by:

$$\sigma = \frac{V_P^2 - 2V_S^2}{2\left(V_P^2 - V_S^2\right)} \qquad (1.4)$$

(Grand and West, 1965). Sheriff (1991) suggested that ordinary values of Poisson's ratio range from 0 for very stiff solids to 0.5 for fluids. For that range of Poisson's ratio, a graph of the ratio of Rayleigh wave velocity to S-wave velocity versus the Poisson's ratio is plotted, and shown in Figure 1-4. The figure shows that Rayleigh wave velocity ranges from 0.87 to 0.96 of S-wave velocity.

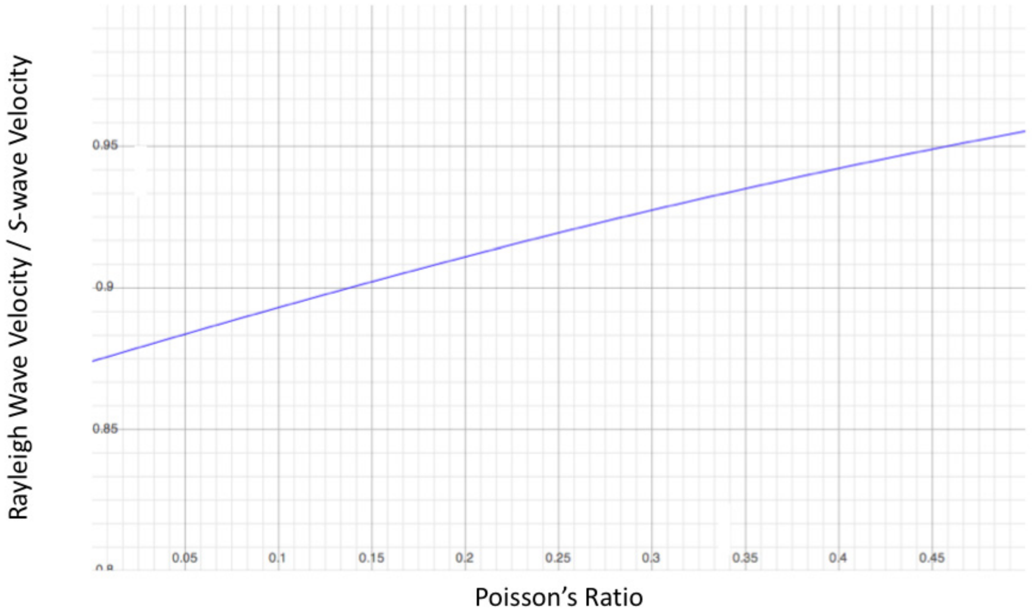

Figure 1-4. Ratio of Rayleigh wave velocity to S-wave velocity versus Poisson's ratios. Earth materials with Poisson's ratio of 0.5 to 0.0 have velocities that range from 0.84 to 0.96 of S-wave velocities.

1.3 Surface-wave methods

Estimation of subsurface mechanical properties by using surface waves was proposed by seismologists for the investigation of the earth crust and upper mantle (Ewing et al, 1957; Dorman et al, 1960; Dorman and Ewing, 1962; Bullen, 1963; Knopoff 1972; Kovach 1978; Mokhtaret al., 1988; Keilis-Boroket al., 1989; Al-Eqabi and Herrmann, 1993). Practical near-surface applications of surface-wave methods, based on the dispersion properties of Rayleigh waves, were developed by the engineering community for geotechnical engineering purposes. Nazarian and Stokoe (1984) have strongly contributed by introducing the SASW (Spectral Analysis of Surface Waves) method. Since then, there have been many multi-station methods introduced with different field setup or analysis techniques (Strobbia, 2003). Multi-channel analysis of surface waves (MASW) was introduced by Park et al. (1999). The SASW method, and the MASW method are two primary techniques for field data acquisition and estimation of the dispersion curve (Pelton, 2005).

The implementation of surface-wave methods involves recording Rayleigh waves on vertical-component receivers, estimating the phase-velocity dispersion curves of the recorded Rayleigh waves, and applying geophysical inversion methods to the dispersion curves for estimating S-wave velocity as a function of depth. Inversion techniques of current surface-wave methods assume a horizontally layered earth model consisting of homogeneous and isotropic layers. These techniques are different in the computation of the forward model and the method of optimization. Derived S-wave velocity information can be useful in foundation dynamics, pavement analysis, soil improvement, static correction of S-wave reflection data (Pelton, 2005).

1.4 Refraction methods

The refraction method is the oldest and most extensively practised near-surface seismic method. It is considered to be the conventional method of mapping near-surface structures. Ray theory is often used for simplicity in seismic refraction. The key concept in seismic refraction is that seismic rays are bent when they strike a geological boundary at certain angle. The amount of bending, θ_2, is function of the velocities of the two geological layers, v_1 and v_2, and the angle of incidence, θ_1 according to Snell's law:

$$\frac{\sin\theta_1}{\sin\theta_2}=\frac{v_1}{v_2}. \tag{1.5}$$

In the case where the velocity of the upper layer is smaller than that of the lower layer, as the incident angle increases, the refracted angle increases and finally equals 90 degrees. At this point, the refracting wave will travel along the interface between the two layers and form refraction. The interpretation methods of seismic refraction for estimating near-surface layer have consistently been a topic of intense interest. In general, those techniques can be classified into the following categories (Russell, 2003):

- The slope-intercept method;
- The reciprocal method;
- The delay time method;
- The least squares method;
- The time-term method.

Refraction methods are described in many geophysical books including Sheriff and Geldart (1982), and Pelton (2005). I am interested here in the application of the Generalized Linear Inverse (GLI) method, which falls under the category of a least squares method. Precise first arrival time picks are required for all methods.

1.5 Static corrections

Static corrections, or statics, are constant time shifts applied to seismic traces to correct reflection arrival times as if all sources and receivers had been located on a specified plane with no weathered layer present. This specified plane is often referred to as the seismic datum. Static corrections are significant because they improve the signal-to-noise ratio of seismic data, and give a better image of the subsurface. Also, they remove the time structure effects for seismic time sections. After the application of statics, reflection events, from intersecting 2D lines or overlapping 3D survey blocks, tie better because all data are corrected to the same datum. Also, the application of statics improves other processing steps, such as velocity analysis. Static corrections are sometimes obtained by uphole surveys. An uphole survey is made by locating successive sources or receivers at varying depths in a borehole to estimate the velocities of the near surface, often a single receiver above a buried dynamite source to give an uphole time. Refraction methods also are widely used to estimate the velocities of the near surface too (Russell, 1993).

1.6 Thesis motivation

Variations in thickness and velocities of near-surface layers can significantly degrade the quality of the seismic image. Static corrections are used to solve for the near-surface problem. Calculation of static corrections, from a near-surface velocity model, is simple and straight forward procedure. However, obtaining an accurate model of the near-surface velocity structure is challenging. For that reason, I have focused my research on the characterization, modeling, and correction of the near surface. Also, another reason is to create near-surface images for water exploration.

1.7 Thesis outline

Chapter One provides an introduction and background to the near surface, the near-surface problem, seismic waves traveling in the near surface, their properties and velocities, static corrections, and some methods for the characterization of the near-surface.

Chapter Two focuses on forward modeling and inversion of a given near-surface earth model. For the modeling part, elastic finite difference techniques are used to numerically model a near-surface earth model, and create synthetic seismic traces. For the inversion part, the goal is to go back to the earth model by refraction analysis and inversion of surface-wave dispersion curves.

Chapter Three characterizes the near surface of our Priddis, Alberta test site. To do so, the lithology is described from shallow well data. Also, the MASW method was applied to 2D seismic refraction data to create an S-wave velocity structure map of the near surface. All data were collected as part of the 2007 University of Calgary Geophysics Field School.

Chapter Four applies the Generalized Linear Inversion (GLI) of first arrival times method to the 2-D reflection seismic survey of Spring Coulee, Alberta. This method is applied to P-wave impulses in the vertical-component data, and to S-wave impulses in the radial component data. The goal is to find near-surface velocity models of P- and S-waves.

Chapter Five applies the MASW to part of the 2D seismic reflection data of Spring Coulee. The goal is to invert dispersion curves of Rayleigh for S-wave velocities, obtain S-wave velocity near-surface model, and compare to the GLI model,

Chapter Six presents the calculation of static corrections method of P-wave data and converted wave data. For both GLI and MASW near-surface models, static corrections are calculated, applied, and compared. P-wave and converted stack sections, with static correction applied, are created.

Chapter Seven summarizes and concludes the thesis.

1.8 Software used

For my thesis, I have used the following software:

- Microsoft Office for writing, sketches, and calculating static corrections
- Grapher for graphing
- Matlab for numerical forward modeling
- ProMAX for seismic processing
- SurfSeis 2.05 for MASW processing
- Hampson Russell (GLI3D) for near-surface modeling and calculating static corrections.

CHAPTER TWO: FORWARD MODELING AND INVERSION OF NEAR SURFACE SEISMIC DATA

2.1 Introduction

Forward-modeling techniques in seismology implement numerical solutions to various wave equation forms to compute synthetic seismograms for a given geological model. Numerical modeling is useful in testing the earth model obtained by the geophysicist by comparing a computed synthetic seismogram to real seismic data. In this chapter, synthetic seismic traces are computed for a near-surface model. From those traces, an estimated model of earth will be created by inversion, and then compared to the original model.

A near-surface model of a single layer over half space is shown in Figure 2-1. This model represents a layer of clay over weathered bedrock. Then, the objectives of this chapter are:

1. To numerically model the seismic wavefield using finite-difference modeling. An elastic model should include surface-wave energy along with body-wave energy.
2. To analyze the variations of first P-wave arrival times with increasing offsets to find P-wave velocities of the near surface.
3. To invert for S-wave velocity and thickness of the clay layer using surface-wave methods, assuming no knowledge about the earth model.
4. To compare the velocity and thickness resulting from inversion to the velocity and thickness of the original geological model shown on Figure 2-1.

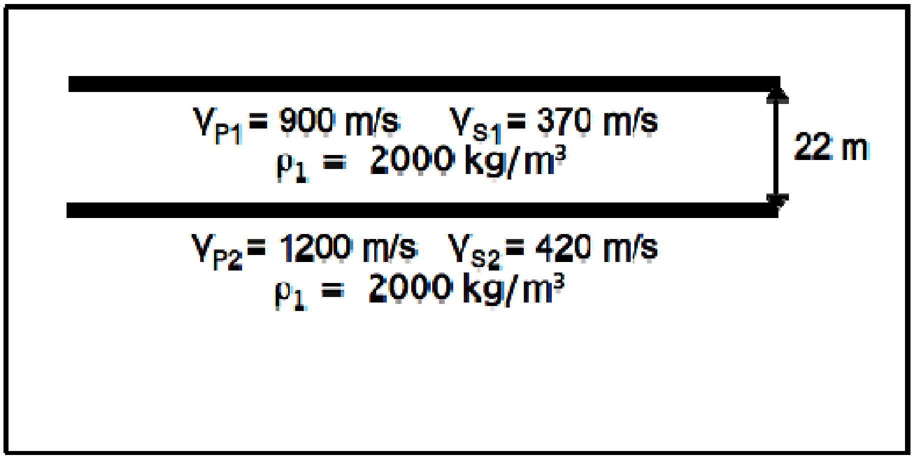

Figure 2-1. Earth model of a single layer over a half-space. This model represents a layer of clay over weathered bedrock (modified after Pelton, 2005).

2.2 Finite-difference modeling

The theory of finite-difference modeling is summarized in Appendix A. The *elastic* finite-difference modeling method, which is used here, models earth material better, but is more complicated than the acoustic modeling method. Acoustic models represent well materials which resist deformation by compression only. These models are efficient because P-wave is the most important type of energy that propagates into earth materials. On the other hand, elastic models resist deformations by both compression and shear, and therefore more accurate represent earth materials.

The numerical modeling code I use was written by Manning (2007), and solves the coupled two-dimensional elastic wave equations for an isotropic medium (ultimately layered):

$$(\lambda+2\mu)\frac{\partial^2 U_z}{\partial z^2}+(\lambda+\mu)\frac{\partial^2 U_x}{\partial x\partial z}+\mu\frac{\partial^2 U_z}{\partial x^2}=\rho\frac{\partial^2 U_z}{\partial t^2},$$

and

$$(\lambda+2\mu)\frac{\partial^2 U_x}{\partial x^2}+(\lambda+\mu)\frac{\partial^2 U_z}{\partial x\partial z}+\mu\frac{\partial^2 U_x}{\partial z^2}=\rho\frac{\partial^2 U_x}{\partial t^2}, \tag{2.1}$$

where λ is the Lamé constant. The horizontal and vertical components of the particle displacement are U_x and U_z respectively. P-wave velocity, V_P, and S-wave velocity, V_S, can be expressed in terms of the Lamé constant, as is shown in Equation (1.1) and Equation (1.2).

Based on the earth model that we are dealing with, $v_{\max}$ in Equation (A.6), given in Appendix A, is equal to 1200 m/s. We chose the time sample rate to be 0.0002 s and the space sample rate to be 1 m in order for $\frac{v_{\max}\Delta t}{\Delta x}$ to be $\leq\frac{1}{\sqrt{2}}$, and satisfies the condition of Equation (2.6). The shot depth is set to be 4 m. A 30 Hz Ricker wavelet was used to construct the wavefield. The wavefield was computed for 3334 time steps to construct a 0.67 s record length at 0.2 ms sample rate. The earth model has been set large enough to represent a half space, and not have interference due to reflections from boundaries. There were 200 channels with 1 m of spacing recorded at the surface. The near offset (source-receiver offset of first receiver) is 10 m.

The upper and lower sections of Figure 2-2 show the wavefield at different time steps. The colors represent the direction of the particle motion of the wavefield. The P-wave energy is indicated by the black box, and the black arrow indicates the direction of the wave propagation. P-wave has particle motion parallel to the direction of wave propagation. The S-wave and Rayleigh wave energy are indicated by the brown and orange boxes respectively, with the direction of wave propagation indicated by brown and orange arrows. The particle motion is perpendicular to the direction of the wave propagation.

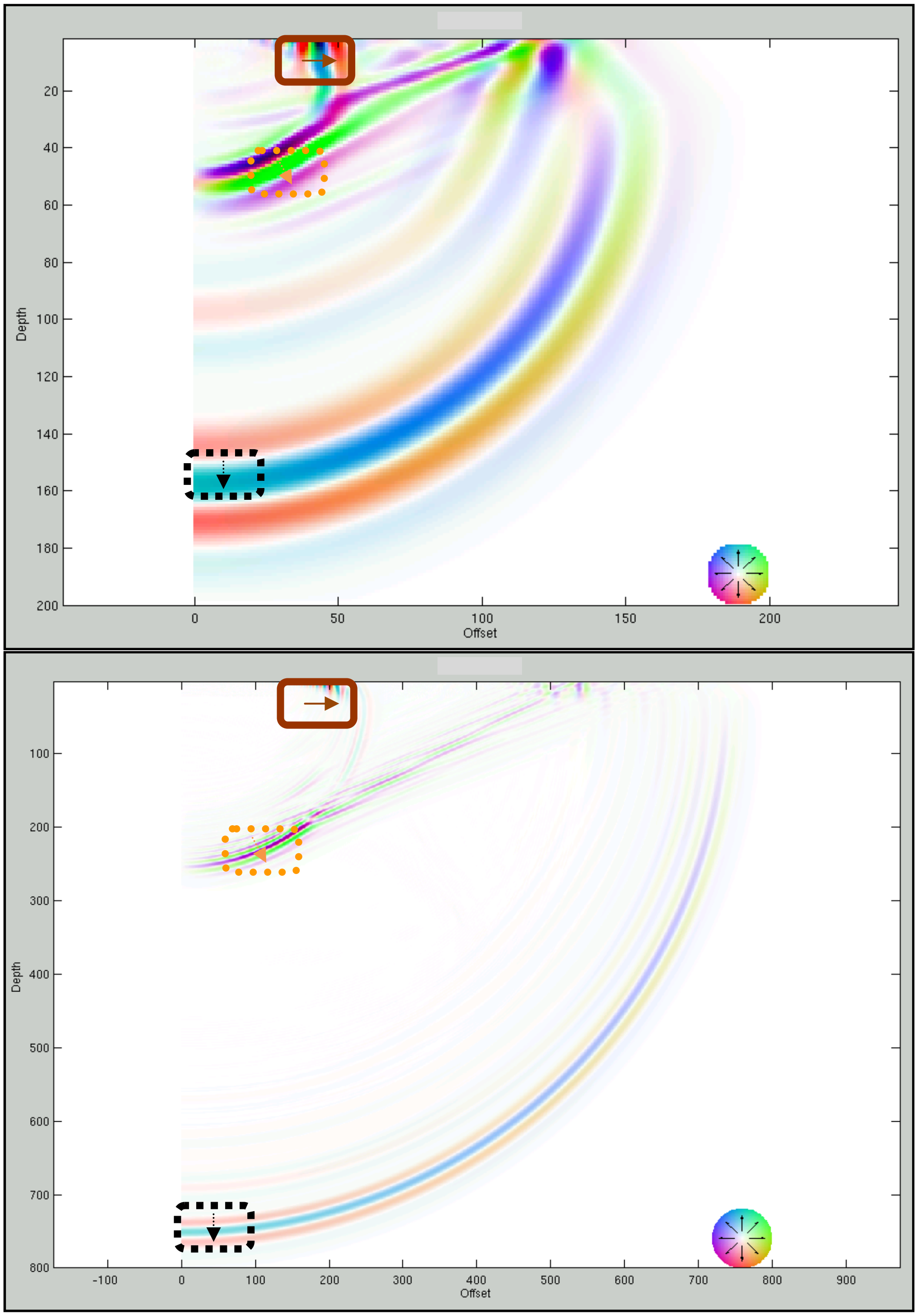

Figure 2-2. A snapshot of the wavefield at (upper) an early time step (time = 171.2 ms), and (lower) the last time step (time = 666.8 ms). Offset and depth are in metres. Colors represent the direction of the wavefield particle motion, as indicated by the label on the lower right corner. P-wave, S-wave, and Rayleigh wave energy are indicated by dashed black, dotted orange, and solid brown boxes respectively. Arrows, inside boxes, represent the direction of wave propagation.

A synthetic shot gather is recorded by 200 channels at the surface and shown in Figure 2-3. Different P-wave events (direct arrivals, refraction, and reflection) are indicated. Dispersive Rayleigh waves are indicated too.

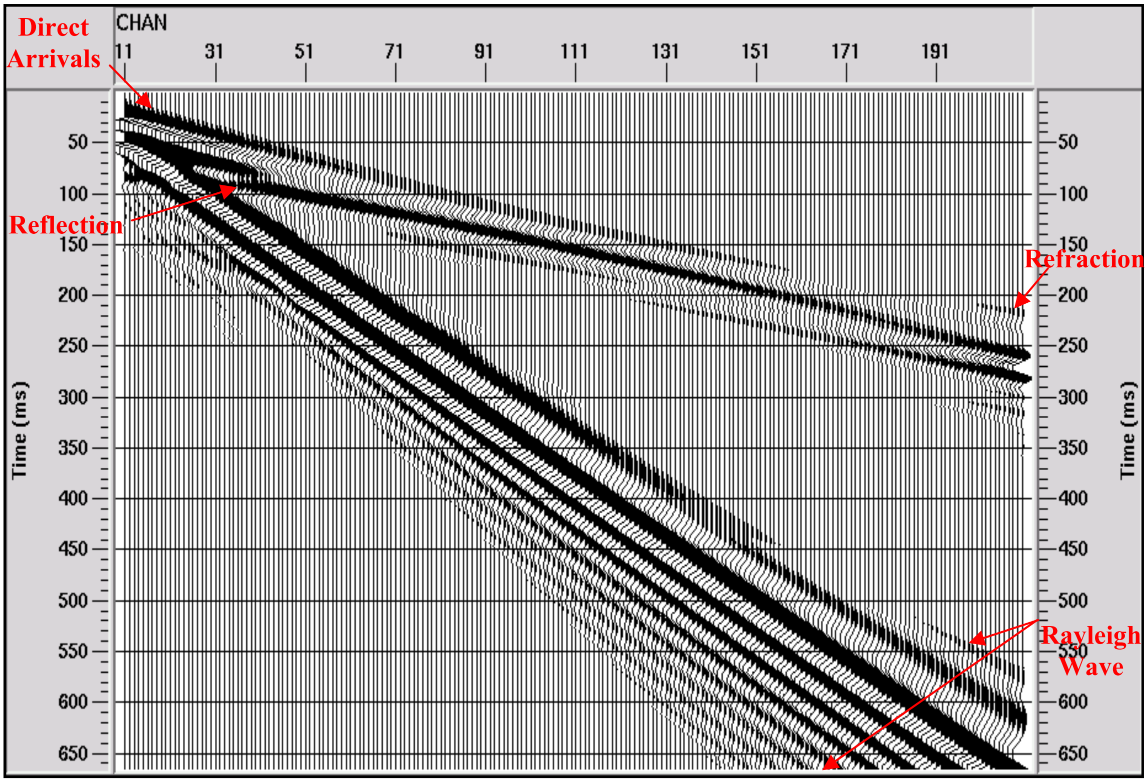

Figure 2-3. An interpreted synthetic shot gather created by finite-difference modeling through the earth model, shown in Figure 2-1. The direct arrivals, reflection, refraction, and Rayleigh wave energy are indicated. The receiver spacing is 1 m.

2.3 Refraction method

Assuming no knowledge about the earth model, we want to use the synthetic shot, shown in Figure 2-3, to find the P-wave velocity structure for the near surface. The easiest approach to solve the inverse problem of finding the velocity as a function of depth is from the variation of arrival times with increasing offsets. The first arrivals are caused by direct arrivals for small offsets, and by refraction or head wave for large offsets. The seismic refraction method , the oldest near-surface method, will be used. The key concept in seismic refraction is that the seismic ray will get refracted if it encounters a geological boundary at certain angle, called the critical angle. The distance that corresponds to the offset required for the refraction to occur is called the critical distance. Ray theory is often used for simplicity when explaining the refraction theory.

The synthetic shot gather, which was created earlier in Matlab, was imported to ProMAX for more display options, and then geometry was created for it. From the slopes of the first breaks, a model of one layer, of thickness h , over half space is assumed. Also, a flat layer of uniform P-wave velocity, α_1 , rather than a dipping layer of varying velocity, is assumed as shown in Figure 2-4. The P-wave velocity of the half space is α_2 . Figure 2-5 shows the same shot gather, but zoomed in, and with two slopes of first breaks indicated.

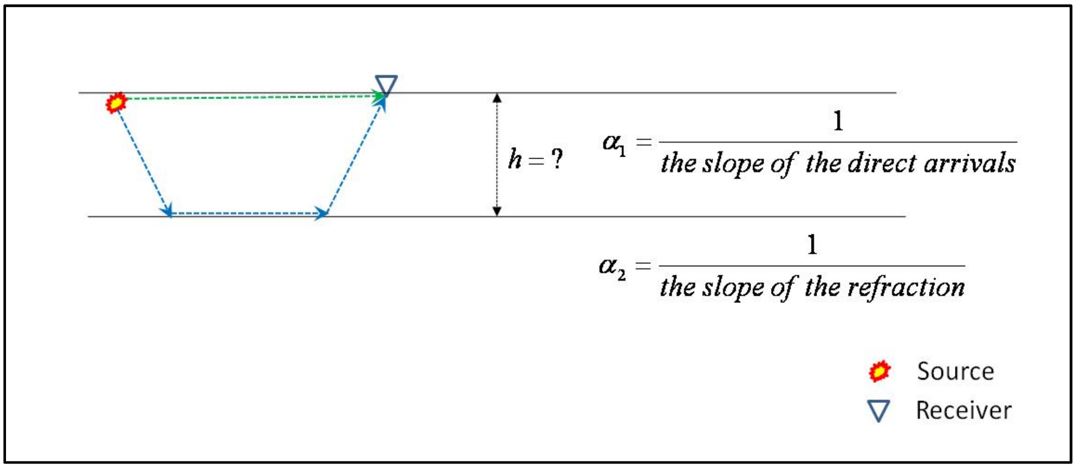

Figure 2-4. A model of a flat single layer over a half space, used for refraction interpretation. α_1 is the P-wave velocity of the first layer, and α_2 is the P-wave velocity of the half space. Direct arrivals and refraction energy are indicated by dashed green line, and dashed blue line respectively.

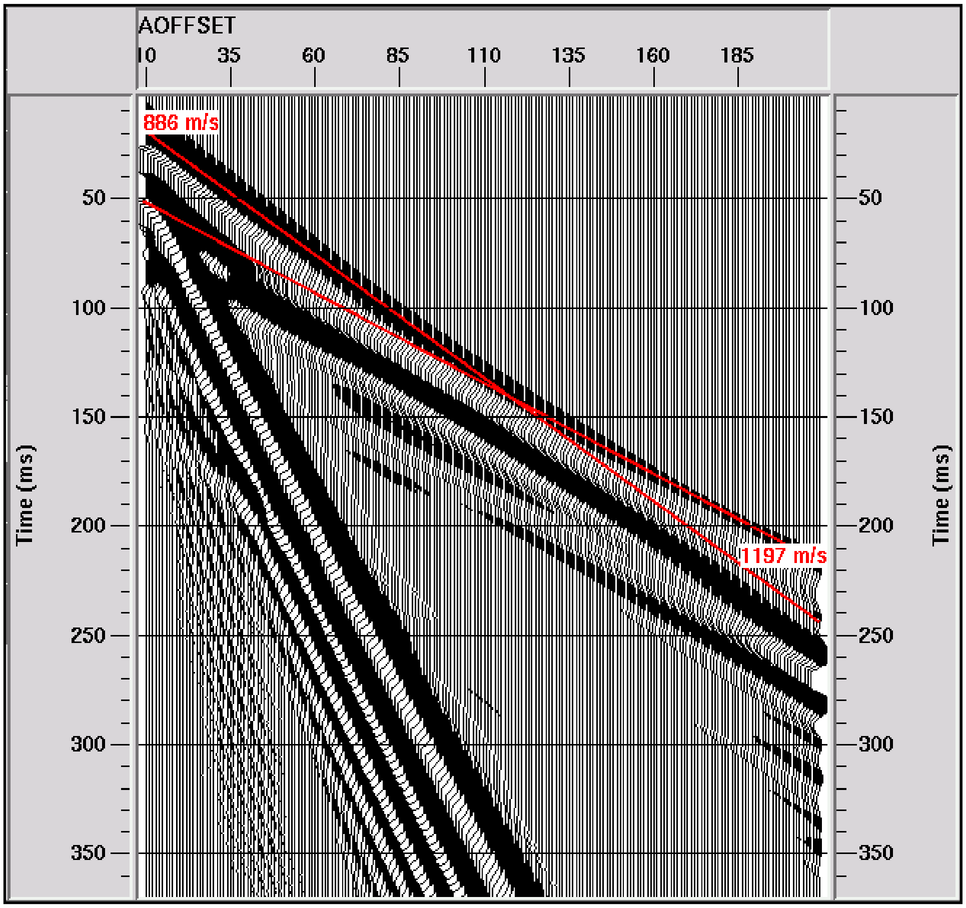

Figure 2-5. A zoomed image of Figure 2-3 with two slopes of first breaks indicated. The two slopes indicate velocities of 886 m/s and 1197 m/s.

On Figure 2-5, the slope at small offsets corresponds to the direct arrivals through the first layer and is related to the first layer velocity, α_1. The second slope at far offsets corresponds to the refracted arrivals through the half space and is related to the half space velocity, α_2. The slope values indicated that the velocity of the first layer is 886 m/s, and the velocity of the underlying half space is 1197 m/s. The distance point where the two slopes intersect is the cross over distance.

From Figure 2-5, the crossover distance is about 117 m. From Snell's law and the geometry of Figure 2-4, a relation between the thickness of the first layer, h, the velocities of the first layer and the half space, and the crossover distance, x_c can be derived

$$h = \frac{x_c}{2}\sqrt{\frac{\alpha_2 - \alpha_1}{\alpha_2 + \alpha_1}} \tag{2.2}$$

Substituting 886 m/s, 1197 m/s, and 117 m for α_1, α_2, and x_c respectively in equation (2.2) will yield in a thickness of about 22.6 m for the first layer. Those values are very close to the earth model, which was used for creating the synthetic data (shown in Figure 2-1; α_1 .= 900 m/s; α_2 = 1200 m/s; h = 22 m).

2.4 Surface-wave method

In this section, the synthetic shot gather that was created earlier for a single layer over a half space, using elastic finite difference modeling, will be used to find the S-wave velocity as a function of depth. Again, no knowledge of the earth model is assumed. In elastic-layered media (more than one layer of S-wave velocity), surface waves are dispersive with multiple modes. The dispersion properties of surface waves and MASW are used here for estimating S-wave velocity. The MASW method was introduced in Chapter 1 of this thesis. The process workflow used here is

1) Read SEG-Y file in SurfSeis 2.05 (software create by Kansas Geological Survey).
2) Create geometry.
3) Mute first breaks.

4) Generate dispersion image of the Rayleigh waves.
5) Pick the fundamental mode dispersion curve.
6) Invert for S-wave velocities using 2 initial models: one that is based on the P-wave model derived earlier using the refraction method and a constant Poisson's ratio, and one that is derived from the dispersion curve.

2.4.1 Dispersive surface waves

Rayleigh waves propagate along the free surface of the earth. The particle motion is elliptical in a plane perpendicular to the surface, and retrograde (particle motion is opposite to the propagation direction in the top of its elliptical path). The amplitude of Rayleigh waves decays exponentially with depth. Unlike the case of isotropic homogeneous half space, Rayleigh waves are dispersive with multiple modes in the case of a real layered earth. In another word, phase velocities vary for different frequencies. The phase velocity, *C*, and the group velocity, *V*, are related as follows

$$C = V\left[1 - \frac{f}{C}\frac{dC}{df}\right], \tag{2.3}$$

where f is the frequency. If no dispersion is present, then the phase and the group velocities are equal. If the phase velocity is decreasing when the frequency increases, then the phase velocity is greater than the group velocity, and that is called normal dispersion (Al-Husseini et al., 1981).

Figure 2-6 shows the synthetic shot, created earlier, with the first breaks muted, and the Rayleigh waves highlighted between two slopes that indicate the phase velocities range. The range of the phase velocities is 300 m/s to 330 m/s.

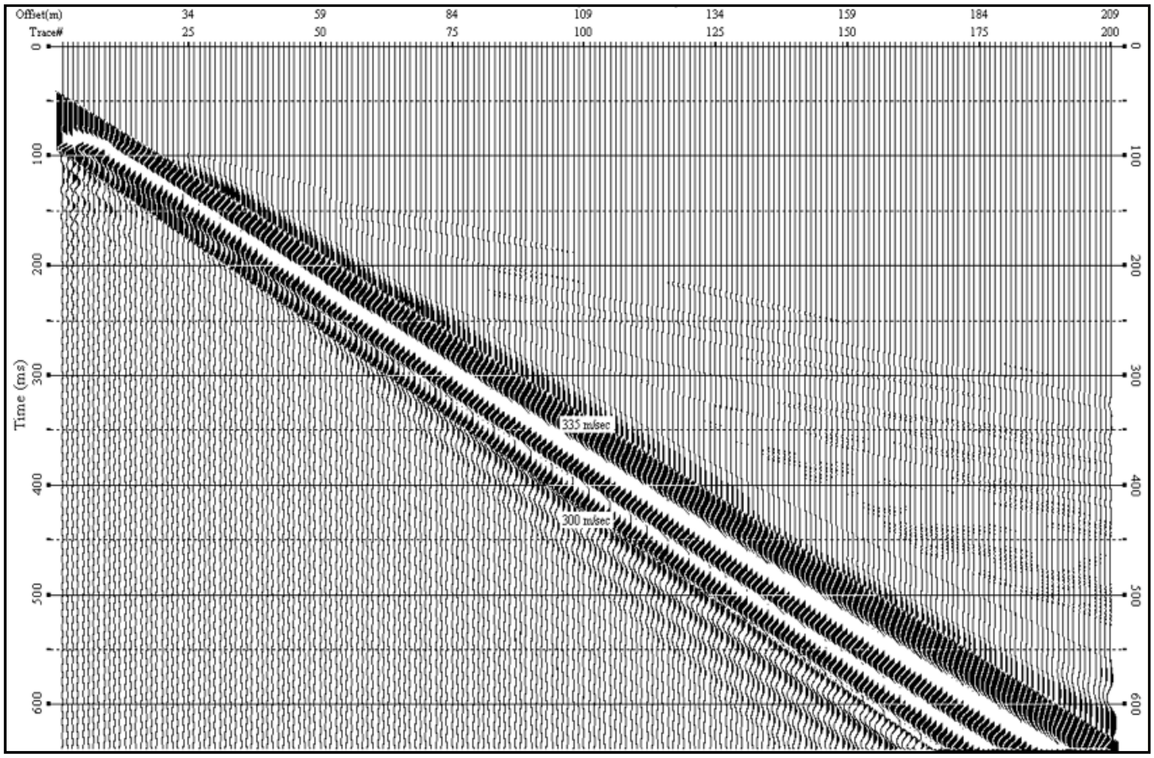

Figure 2-6. The synthetic shot gather, created by finite difference modeling, with first breaks muted and with the Rayleigh wave highlighted.

The phase velocity of surface waves of a layered earth model is a function of frequency and four earth parameters, which are P-wave velocity (α), S-wave velocity (β), density (ρ), and the layer thickness (h) The Rayleigh-wave phase velocity is most sensitive to the S-wave velocity. Analysis of the sensitivity of Rayleigh wave phase velocity to S-wave velocity, P-wave velocity, and density can be found in Xia et al., (1999).

In a homogeneous half space (non-dispersive case), Rayleigh-wave velocity, C_R, is constant and given by Equation (1.6). For a real layered earth (dispersive case), the Rayleigh-wave phase velocity is determined by the characteristic equation, F (Anderson et. al, 2003),

$$F(f_j, C_{Rj}, \beta, \alpha, \rho, h) = 0 \qquad (j = 1, 2, \ldots., m), \tag{2.5}$$

where

f_j is the frequency in Hz,

C_{Rj} is the Rayleigh-wave phase velocity at frequency f_j,

$\beta = (\beta_1, \beta_2, \ldots.., \beta_n)^T$ is the S-wave velocity vector, where β_i is the S-wave velocity of the ith layer,

$\alpha = (\alpha_1, \alpha_2, \ldots.., \alpha_n)^T$ is the P-wave velocity vector, α_i is the P-wave velocity of the ith layer,

$\rho = (\rho_1, \rho_2, \ldots., \rho_n)^T$ is the density vector, ρ_i is the density of the ith layer,

$h = (h_1, h_2, \ldots., h_{n-1})^T$ is the thickness vector, where h_i is the thickness of the ith layer, and

n is the number of layers within the earth model.

The inversion for the S-wave velocity (β) is described briefly later in this chapter.

2.4.2 Dispersion curves

The dispersion curves (plots of velocity versus frequency) are used to separate different modes of surface waves. The most widely used method for creating dispersion curves is the slowness-frequency $(p-\omega)$ method of McMechan and Yedlin (1981). A shot gather in the offset-time (x-t) is transformed to the intercept time-slowness $(\tau - p)$ wavefield by slant stacking. Then, by 1-D Fourier transform the wavefield is transformed to the slowness-frequency $(p-\omega)$ domain. An example of this method is shown in Figure 2-7.

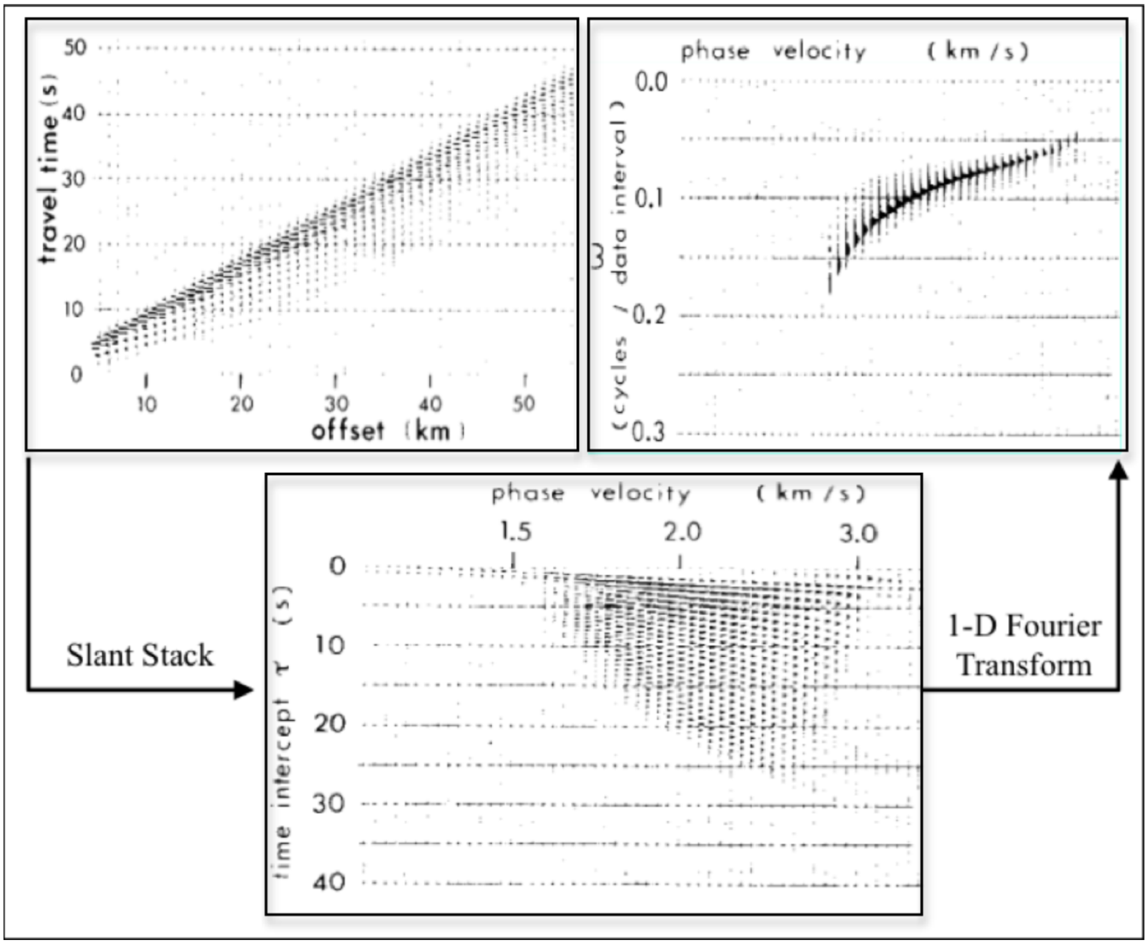

Figure 2-7. Slowness-frequency transformation method. Top left is a shot gather in offset-time domain, bottom is in the intercept time-slowness, and top right is the slowness-frequency (modified after McMechan and Yedlin, 1981).

The method, used here was developed by Park, et al. (1998). A shot gather in space-time domain, *u(x,t)*, is transformed to the space-angular frequency domain, $U(x,\omega)$, using forward Fourier Transform as follows

$$U(x,\omega) = \int u(x,t)e^{i\omega t}dt, \qquad (2.6)$$

where ω is the angular frequency. $U(x,\omega)$ can be represented as the multiplication of the phase spectrum [$P(x,\omega)$] and the amplitude spectrum [$A(x,\omega)$].

$$U(x,w) = A(x,w)\,P(x,w)\,. \tag{2.7}$$

The phase spectrum contains the dispersion information, and the amplitude spectrum contains all other information, such as attenuation. $U(x,\omega)$ can be expressed as follows:

$$U(x,\omega) = A(x,\omega)e^{-i\phi x}, \tag{2.8}$$

where $\phi = \frac{\omega}{c_\omega}$, and c_ω is the phase velocity. Now, we apply the following integral transformation:

$$S(\omega,\theta) = \int e^{i\theta x}\left[\frac{U(x,\omega)}{|U(x,\omega)|}\right]dx = \int e^{-i(\phi-\theta)x}\left[\frac{A(x,\omega)}{|A(x,\omega)|}\right]dx\,. \tag{2.9}$$

This transformation can be thought of as summing over the offset of the wavefields of a frequency after applying offset-dependent phase shift, θ, determined for an assumed phase velocity , c_ω. This transformation is equivalent to slant stacking of the equivalent time expression of $\frac{U(x,\omega)}{|U(x,\omega)|}$ for a single frequency. Then for a given frequency (ω), *S* will have a maximum at $\phi = \theta = \frac{\omega}{c_\omega}$, and, c_ω can be estimated where peak of *S* occurs. If higher modes have significant amount of energy, then more than one peak will appear. The wavefield $I(\omega,c_\omega)$ is obtained by changing the variables such that $c_\omega = \frac{\omega}{\theta}$. The peaks along the c_ω axis, in $I(\omega,c_\omega)$, will determine the dispersion curve.

The resolution of the dispersion image obtained by this method is superior to that obtained by the slowness-frequency $(p-\omega)$ method particularly for small number of traces collected over a limited range of offsets (Park et al., 1998). This method was used to create a dispersion image of the synthetic shot gather modeled earlier. Figure 2-8 shows the dispersion curve with the fundamental mode picked and indicated by white square dots. The frequencies of the fundamental mode range from 5 Hz to 50 Hz, and the phase velocities range from 300 m/s to 330 m/s.

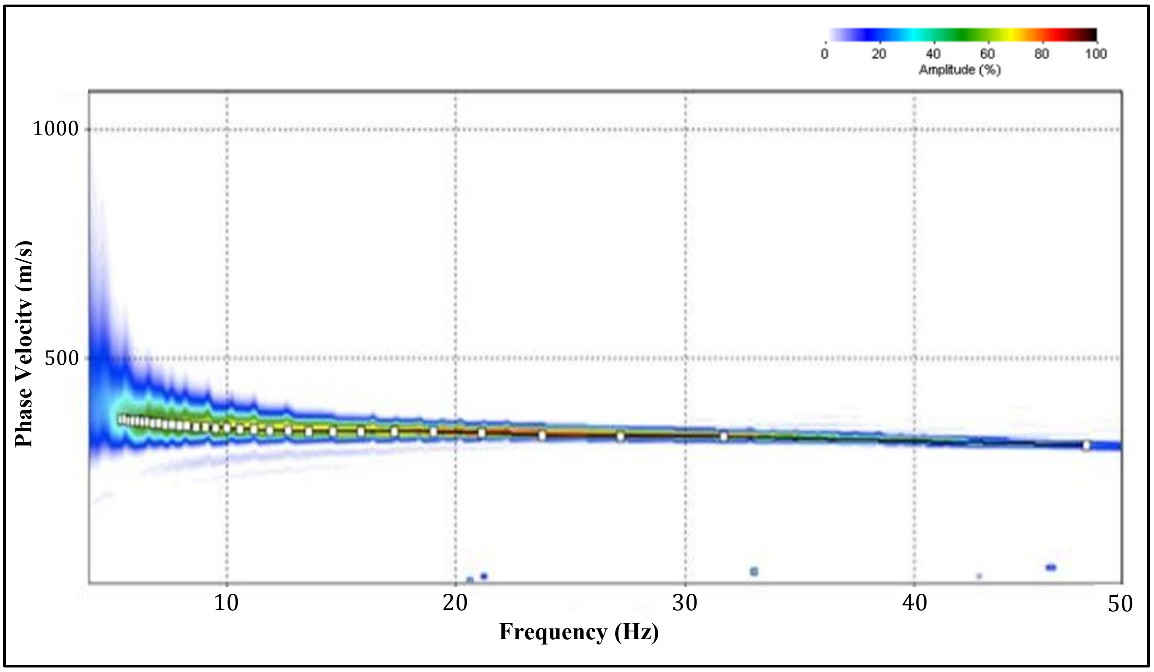

Figure 2-8. A dispersion curve of the synthetic shot gather, which was created by finite difference modeling, with fundamental mode picked and indicated by square white dots. The image is obtained in SurfSeis 2.05, using the method of Park et al. (1998). The vertical axis is phase velocity in m/s, and the horizontal axis is frequency in Hz.

The cut-off frequency of the fundamental mode can be estimated. The cut-off frequency, f_{cn}, of the nth mode is given by (Krebes, 1989):

$$f_{cn} = \frac{V_s(n+\frac{1}{2})}{2h}, \tag{2.10}$$

where *h* is the layer thickness, and *n* is the mode (*n* = 0, 1, 2 for the fundamental mode, 1st higher mode, 2nd higher mode respectively). The S-wave velocity of the first layer, which was used to create the synthetic seismograms, is 370 m/s, and the first layer thickness is 22 m. Then, substituting those values and 0 for the mode in Equation (2.10) gives 4.2 Hz for the cut-off frequency. Therefore, frequencies below 4.2 Hz should not propagate through the first layer, and that agrees with our picked fundamental mode dispersion curve, for which the lowest frequency is 5 Hz.

2.4.3 Inversion of the dispersion curve

The unknown system is parameterized and described by a finite set (*m*) of model parameters. The unknown model parameters (*m*) are the S-wave velocity (β) the P-wave velocity (α) the density (ρ) and the thickness (*h*) of *n* layers:

$$m = [\beta_1, \alpha_1, \rho_1, h_1; \beta_2, \alpha_2, \rho_2, h_2; ...; \ \beta_n, \alpha_n, \rho_n, h_n]. \tag{2.11}$$

For *n* layers, the number of model parameters is $4n-1$because the last layer is a half space and its thickness is a priori information. The measured data (*d*) are Rayleigh-wave phase velocities (C_R) for *j* values of frequencies:

$$d = [C_{R1}, C_{R2}, ..., C_{Rj}]. \tag{2.12}$$

For each frequency, a function (G) of the model parameters gives the Rayleigh-wave phase velocity:

$$\begin{aligned}
C_{R1} &= G_1[\beta_1,\alpha_1,\rho_1,h_1;\beta_2,\alpha_2,\rho_2,h_2;...;\beta_n,\alpha_n,\rho_n,h_n] \\
C_{R2} &= G_2[\beta_1,\alpha_1,\rho_1,h_1;\beta_2,\alpha_2,\rho_2,h_2;...;\beta_n,\alpha_n,\rho_n,h_n] \\
&\vdots \\
C_{Rj} &= G_j[\beta_1,\alpha_1,\rho_1,h_1;\beta_2,\alpha_2,\rho_2,h_2;...;\beta_n,\alpha_n,\rho_n,h_n]
\end{aligned} \tag{2.13}$$

The forward problem is to compute the data when the model parameters are known, while the inverse problem is to estimate the model parameters if the data (Rayleigh-wave phase velocities for different frequencies) were measured. As mentioned earlier, the Rayleigh-wave phase velocities are more sensitive to the S-wave velocities and thicknesses than other model parameters. In the inversion process, the other model parameters are assumed as a priori information (Strobbia, 2003). From an initial guess model, Rayleigh-wave phase velocities of different frequencies (dispersion curves) are calculated, and then compared to the measured dispersion curves. Then the initial model will be updated until some acceptable agreement with the measured dispersion curves is reached. The inversion of S-wave velocity (*β*) is obtained by an automated iterative process. The process is automated (or driven) by a least-square criterion. After each iteration, only the S-wave velocity (*β*) gets updated while the other model parameters (*m*) remain unchanged (Park et al., 1999).

The SurfSeis 2.05 software is used for the inversion. Two initial models were created:

1. **Model (A)**: based on the P-wave velocity model derived earlier using the refraction analysis.
2. **Model (B)**: derived from the dispersion curve.

Both models will be inverted with 8 iterations, and the inversion results will be compared to each other to see how the initial model affects the results of the inversion, and will be compared as well to the near-surface model, used for creating the seismic data.

Model (A) is a simple 1-layer model that is based on P-wave velocity data, obtained by the refraction analysis. From the refraction analysis, a one-layer over half space model was constructed. The thickness of this layer is 22.6 m. To calculate the initial S-wave velocities, a Poisson's ratio of 0.405 is used to calculate the S-wave velocity values from P-wave velocity values, as shown in Table 2-1.

Table 2-1. Initial S-wave velocity model (A): based on P-wave velocity model and a fixed Poisson's ratio of 0.405.

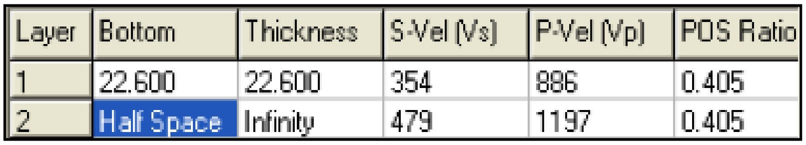

Layer	Bottom	Thickness	S-Vel (Vs)	P-Vel (Vp)	POS Ratio
1	22.600	22.600	354	886	0.405
2	Half Space	Infinity	479	1197	0.405

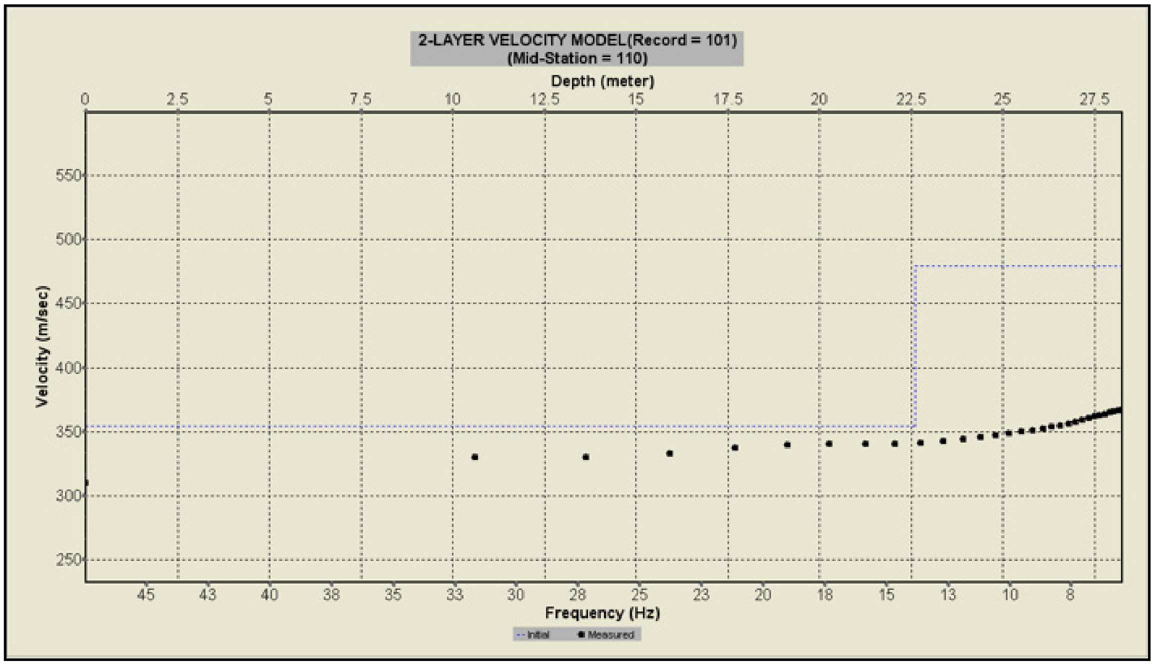

Figure 2-9. Initial S-wave velocity model (A) in dashed blue line; the black dots are the fundamental mode dispersion curve picks. Note frequencies are plotted in descending value, and depth is along the top horizontal axis.

An S-wave velocity profile was created by the inversion of Rayleigh waves and shown in the solid blue line in Figure 2-10. On the same Figure, the initial model is indicated by the dashed blue line. The dispersion curve of the fundamental mode for the inverted model is indicated by the solid purple line in Figure 2-11. On the same figure, the fundamental mode dispersion curve of the initial model is indicated by dashed purple line, and the original fundamental mode picks of Figure 2-8 are indicated by the black dots. The fundamental mode dispersion curve of the inverted model is considerably closer to the original picks than that of the initial model.

In the S-wave velocity profile, obtained by MASW, the thickness of the first (clay) layer was fixed to 22.6 m, and the S-wave velocity was estimated to be 357 m/s. The velocity of the weathered bedrock is estimated to be 422 m/s. Comparing those values to the earth model, used for creating the synthetic data (shown in Figure 2-1), velocities are very close.

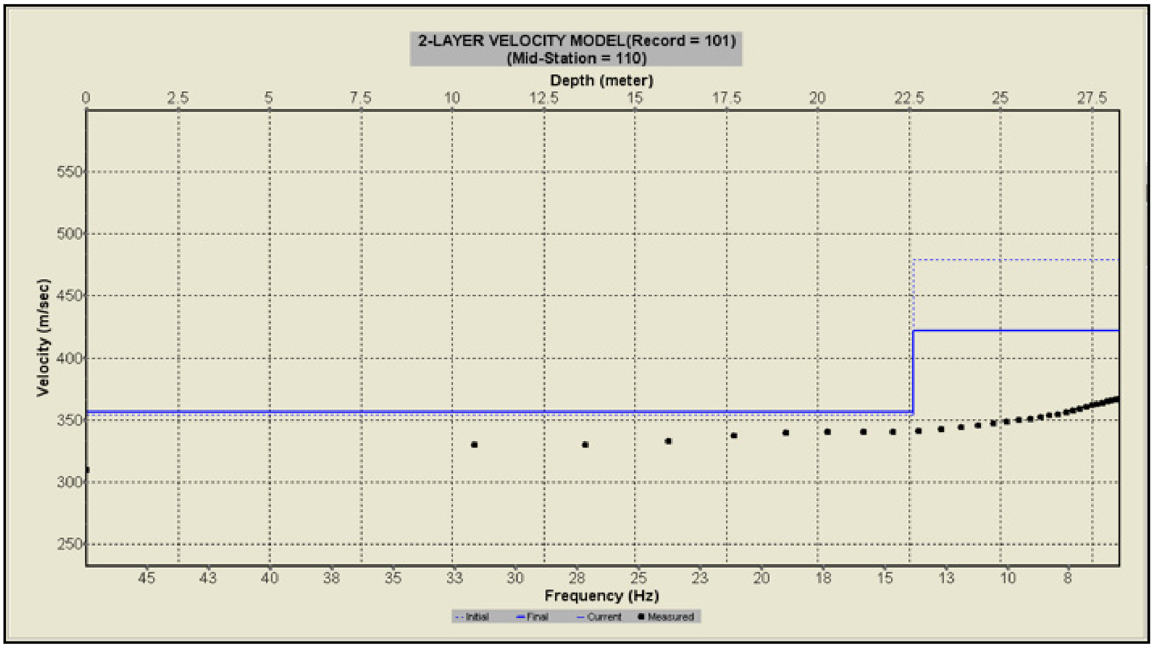

Figure 2-10. Initial model (A) in dashed blue line, and final inversion result in solid blue line. Again, picked fundamental mode is indicated by black dots. Frequencies are plotted in descending value, and depth is along the top horizontal axis.

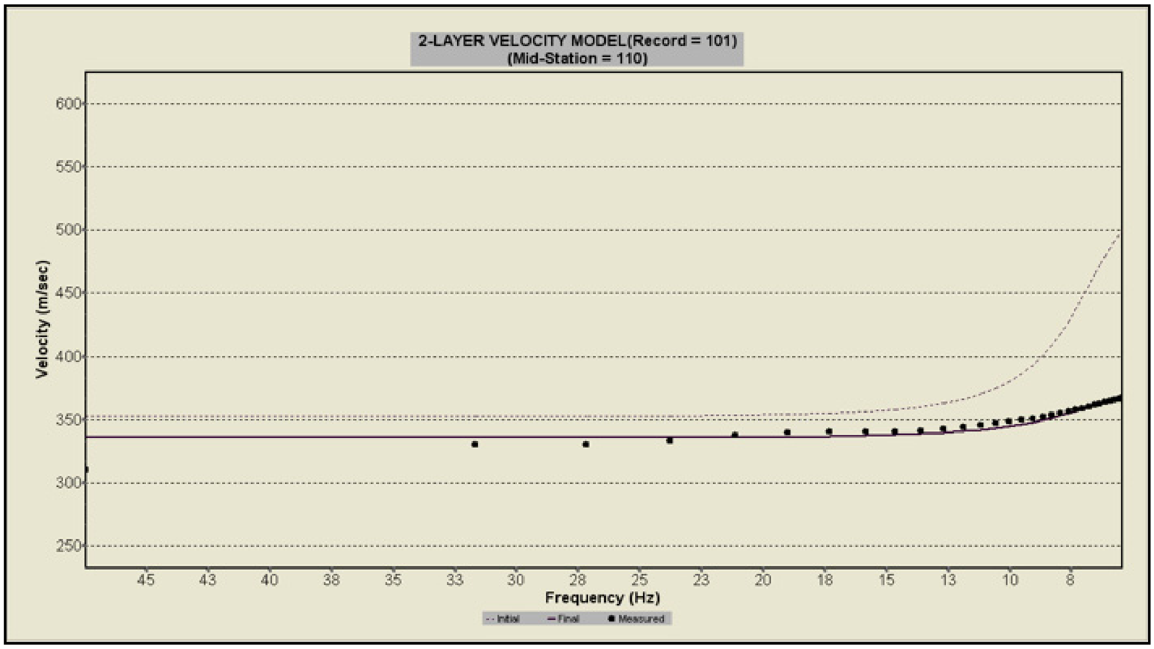

Figure 2-11. The dispersion curve of the fundamental mode for initial model (dashed purple line) and inverted model (solid purple line). Original picks are the black dots.

I repeated the inversion of surface waves, but using initial model (B). This model is a 10-layer model and created from the fundamental mode dispersion curve by SurfSeis 2.05. In some cases, S-wave velocity layering of the near surface is independent of P-wave velocity layering. In such cases, if layer thicknesses of the S-wave velocities were fixed, a model with a larger number of layers is more suitable. The 10-layer initial model (B) is indicated by the dashed blue line in Figure 2-12.

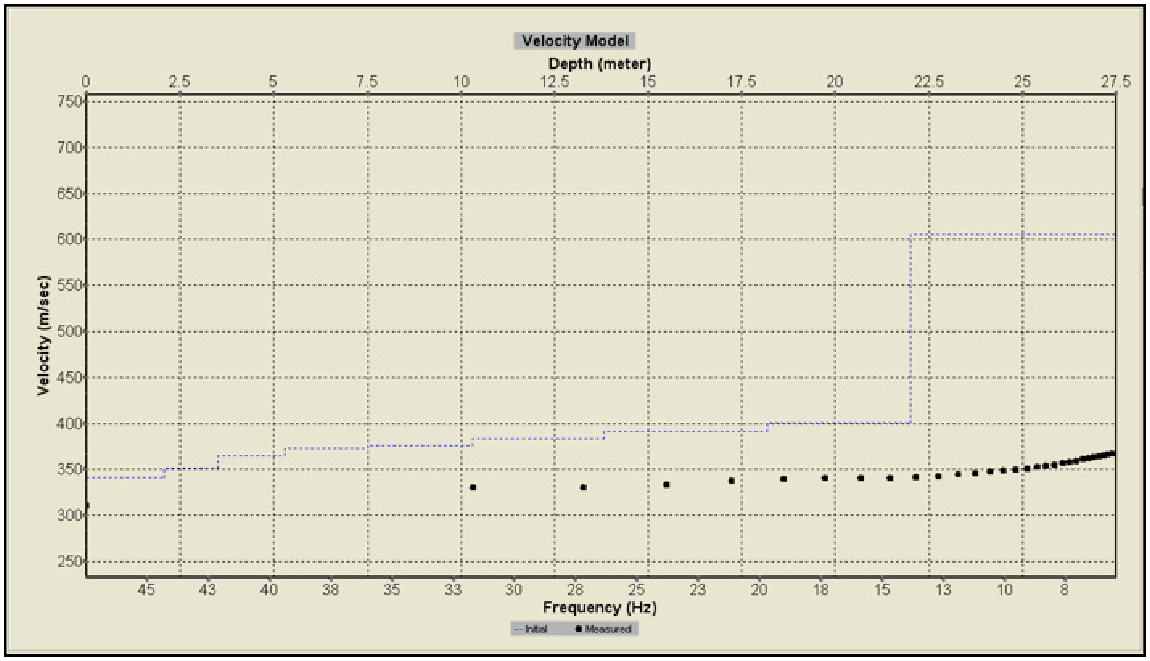

Figure 2-12. Initial S-wave velocity model (B) is indicated by dashed blue line. The black dots are the fundamental mode dispersion curve picks. Note frequencies are plotted in descending value, and depth is along the top horizontal axis.

The S-wave velocity profile created by MASW inversion using the 10-layer initial model (B) is indicated by the blue solid line in Figure 2-13. The inversion results can be divided into two distinct layers. The clay layer has an S-wave velocity of 360 m/s and thickness of 22 m. The second layer has an S-wave velocity of 420 m/s. Comparing those values to the earth model, used for creating the synthetic data (Figure 2-1), we can see velocities and thickness are very close. The difference between the actual and the inverted S-wave velocities is shown in Table 2-2. The Root Mean Square is calculated by:

$$E_{RMS} = \sqrt{\frac{1}{n}\sum_{i=1}^{n} E_i^2}\,, \tag{2.14}$$

where n is the number of layer, and E_i is the difference between the actual and inverted S-wave velocities for the i^{th} layer. Then, substituting those values of Table 2-2 in Equation (2.14) gives an RMS of 17.5 m/s (~ 4.6% error) for the whole S-wave profile. If we exclude the first 5 m, the RMS would decrease to 9.8 m/s (~ 2.6% error).

In general, whatever initial model (A) or (B) was used, the results of the inversion were very close to the earth model.

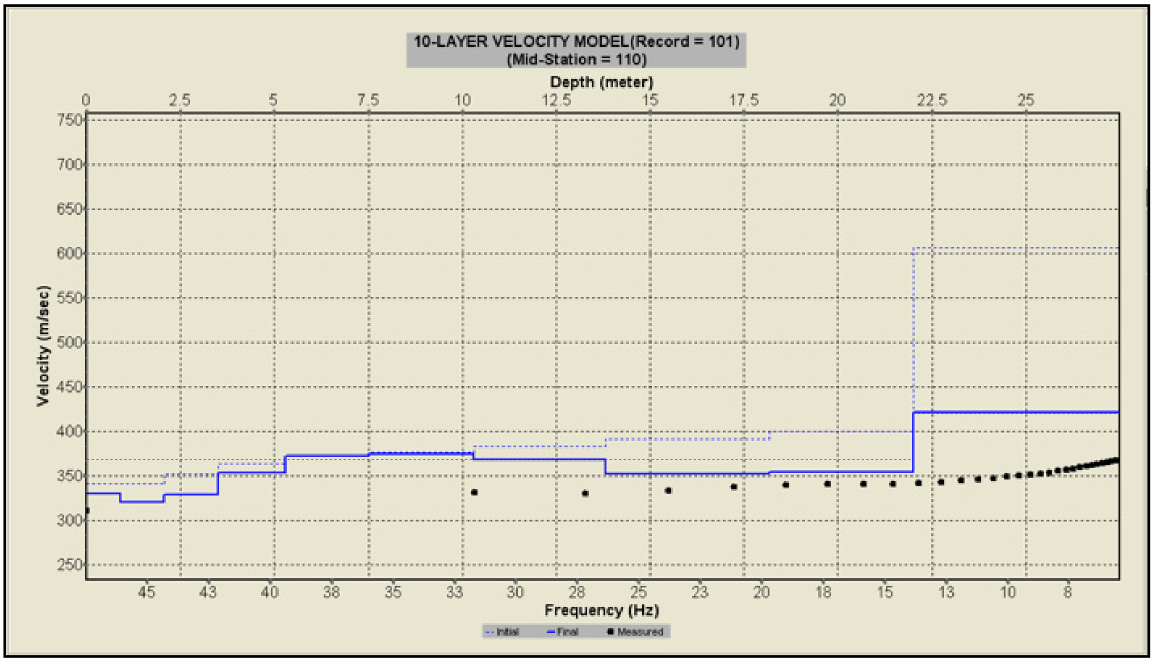

Figure 2-13. Initial S-wave velocity model (B) is the dashed blue line. Final inverted model is the solid blue line, and the original earth model is dashed red. The black dots are the fundamental mode dispersion curve picks. Note frequencies are plotted in descending value, and depth is along the top horizontal axis.

Table 2-2. Average error between actual and inverted S-wave velocities of Figure 2-13.

Depth (m)	Average error between actual and calculated V_s in m/s
2.5	41
5	28
7.5	-4
10	-7
12.5	-5
15	6
17.5	17.5
20	17
22.5	12
25	0
27.5	0

2.5 Discussion and conclusion

Modeling by finite difference techniques is a useful tool that geophysicists use for testing their earth models, and the methods by which they obtains their earth models. This tool has been successfully used in this part of my thesis to create synthetic seismograms through a simple earth model. An analysis of the variations of first P-wave arrival times with increasing offsets was carried out to obtain a P-wave velocity profile. The P-wave velocity profile obtained by the refraction analysis was close to the original earth model.

Surface-wave methods were successfully used to obtain an S-wave velocity profile by the inversion of the fundamental mode dispersion curve. The dispersion curve is obtained by the wavefield transformation developed by Park, et al. (1998). Two initial S-wave velocity models were built: based on P-wave velocity information obtained by refraction analysis with a fixed P- to S-wave velocity ratio; and derived from normal dispersion curve of Rayleigh wave. Whatever initial model was used, the results of the surface-wave inversion for S-wave velocities were close to the earth model.

CHAPTER THREE: LITHOLOGICAL AND SURFACE-WAVE NEAR-SURFACE ANALYSIS AT THE ROTHNEY TEST WELL SITE

3.1 Introduction

As mentioned earlier, the properties of surface waves can be useful for estimating S-wave velocities of the near surface. The MASW method was applied to obtain a near-surface S-wave velocity map at a study site located on property owned by the University of Calgary, the Rothney Astrophysical Observatory near Priddis, Alberta. The implementation of the MASW method involves recording Rayleigh waves on vertical-component geophones, estimating phase-velocity dispersion curves for Rayleigh waves, and then inverting these dispersion curves to estimate S-wave velocity as a function of depth. The process workflow for our surface-wave analysis in Priddis is outlined in Figure 3-1. The data was processed using SurfSeis 2.05. The purpose of our study is to obtain S-wave velocity for the near surface.

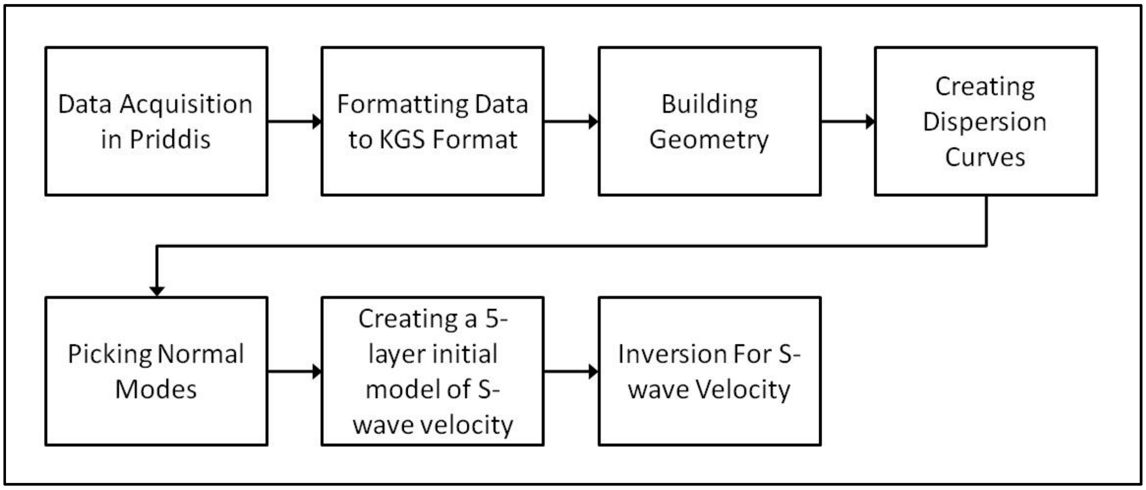

Figure 3-1. Process workflow for S-wave velocity mapping by surface-wave analysis in Priddis.

The lithology of the near surface was studied. Samples from well-cuttings were described as part of this near-surface study. The drilled well and the acquired seismic data were from the 2007 University of Calgary Geophysics Field School.

3.2 Study area

The study area is located near Priddis, Alberta, at the Rothney Astrophysical Observatory site, 25 km southwest of Calgary. The study area is indicated by the red circle, shown on the surface geology map in Figure 3-2. As an activity of the 2007 University of Calgary Field School, hammer seismic data were obtained along the two-dimensional seismic line shown on Figure 3-2. This line was located near (~ 2.5 m from) a 127-m test well whose location is indicated by the red dot on Figure 3-2. Rock cuttings obtained when the well was drilled gave an estimate of the near-surface lithology near the seismic line. Figure 3-3 shows a photograph of Priddis site with the well indicated by the red “A”. Figure 3-4 shows the elevation profile along the line. The line is 403 m long from southeast to northwest. The elevation is highest (1268 m above sea level) in the south-eastern part of the line, and lowest (1252 m above sea level) in the north-western part of the line. The blue line, shown in Figure 3-4, indicates the area for which an S-wave velocity profile (~ 252 m long) will be created by the MASW method.

The surface geology, of the study area, consists of the Paskapoo formation. The Paskapoo formation, which is dominated by shale and sandstone, is the largest groundwater source in the Canadian Prairies (Grasby, 2006).

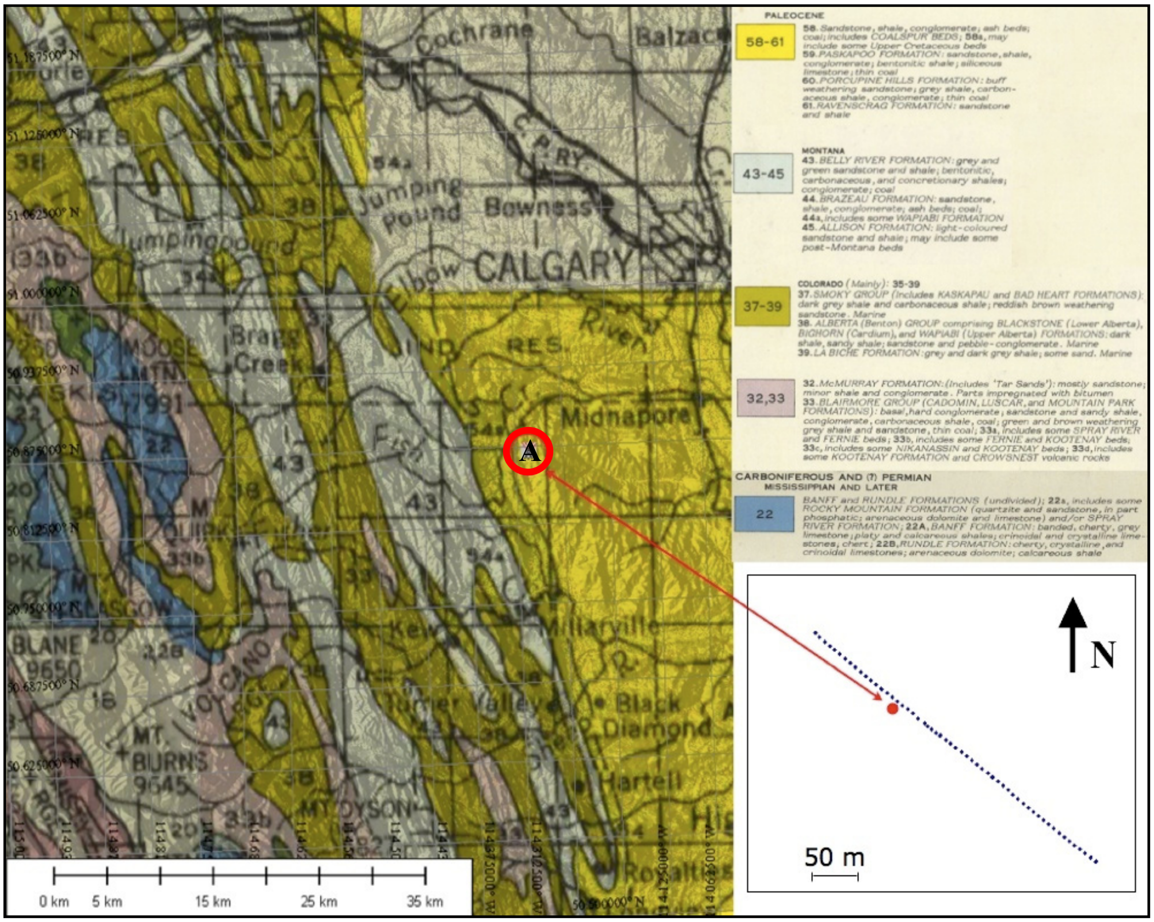

Figure 3-2. Location map showing: surface geology, well, and two-dimensional refraction seismic line (modified after Geological Survey Division, 1951). The zoomed area shows the line configuration and location of the well (red dot).

Figure 3-3. Priddis site: looking west (R. R. Stewart photo). "A" indicates the well.

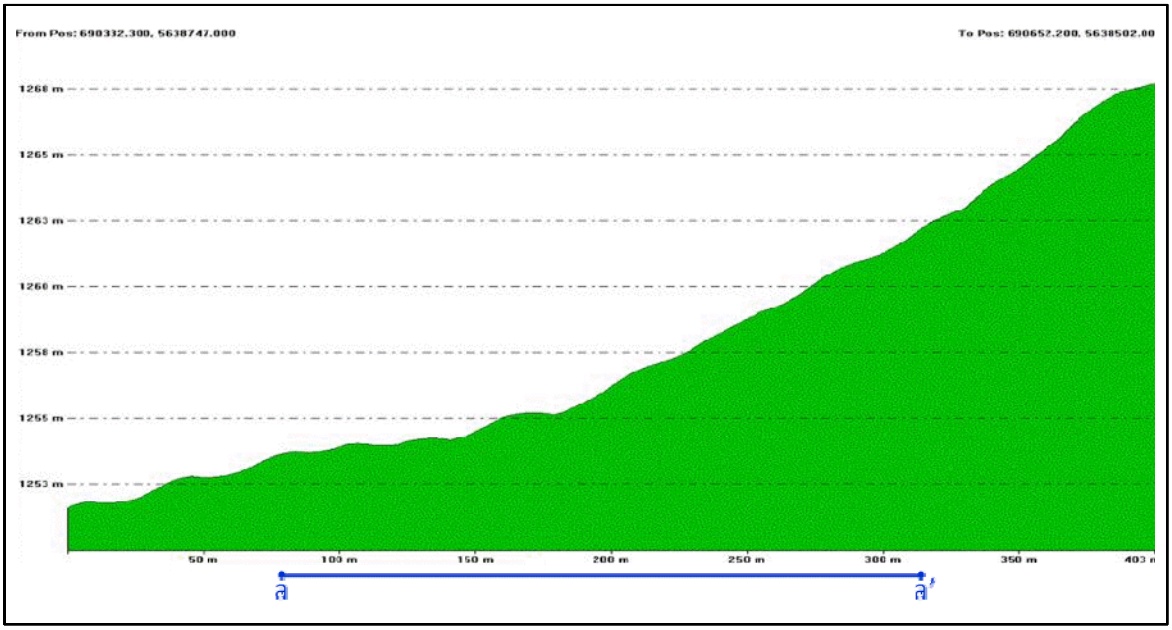

Figure 3-4. Elevation profile. The blue line indicates the area for which an S-wave velocity profile will be created by the MASW method.

3.3 Lithology description

From the shallow well, shown in Figure 3-2, well-cutting samples were collected, and then washed in the laboratory. Then under the microscope, I undertook a description of the lithology type, grain color, and grain size. For sandstone, roundness, sorting, compaction, and porosity were described as well. For shale, fissility, and induration were described too. In Table 3-1, I summarize the description of all samples from the surface to 31. 1 m deep:

Table 3-1. Samples (from well cuttings) descriptions.

Depth (m)	Sample Description
0-2.1	**50% Sandstone:** Transparent, translucent in part, very fine to medium, sub-angular to sub-rounded, moderately sorted, loose, and low porosity. **50% Clay**: Tan to brown, friable, and calcareous.
2.1-4.0	**70% Sandstone:** Transparent, translucent in part, fine to medium, sub-angular to sub-rounded, moderately to well sorted, loose, and low porosity. **30% Clay**: Tan to brown, soft, and calcareous.
4.0-18.0	**100% Sandstone:** Mainly translucent, transparent and white in part, very fine to coarse, angular to sub-rounded, moderately sorted, moderately compacted, and low porosity.
18.0-22.0	**100% Shale**: Gray, blocky, sub-fissile in part, moderately indurated,

	and highly calcareous.
22-23.2	**80% Sandstone:** Transparent, tan, very fine to medium, angular, moderately sorted, well compacted with calcareous cement in part, and low porosity. **20% Shale**: Gray, blocky to sub-blocky, and well-indurated.
23.2-23.8	**100% Shale**: Gray, blocky, well indurated, and calcareous.
23.8-28.3	**100 % Siltstone:** light gray, tan in part, blocky, moderately indurated, and slightly calcareous.
28.3-31.1	**100 % Siltstone:** light gray, tan in part, blocky, moderately to well indurated, and calcareous.

Then, a lithology log of the near surface was created from the description of the samples. Figure 3-5 shows the lithology log of the near surface (first 31.1 m). The near surface consists of the Paskapoo clastics. P-wave velocities of the near surface were calculated from the sonic log of the well, and shown in Table 3-2. The P-wave velocity log calculated from the sonic log is shown in Figure 3-6. The upper 3.9 m are missing from the sonic log, but are estimated, from direct arrivals (Figure 3-8), to be about 400 m/s. This overburden layer consists of sandstone and clay particles. The lower layers are more compacted clastics, and have higher P-wave velocities.

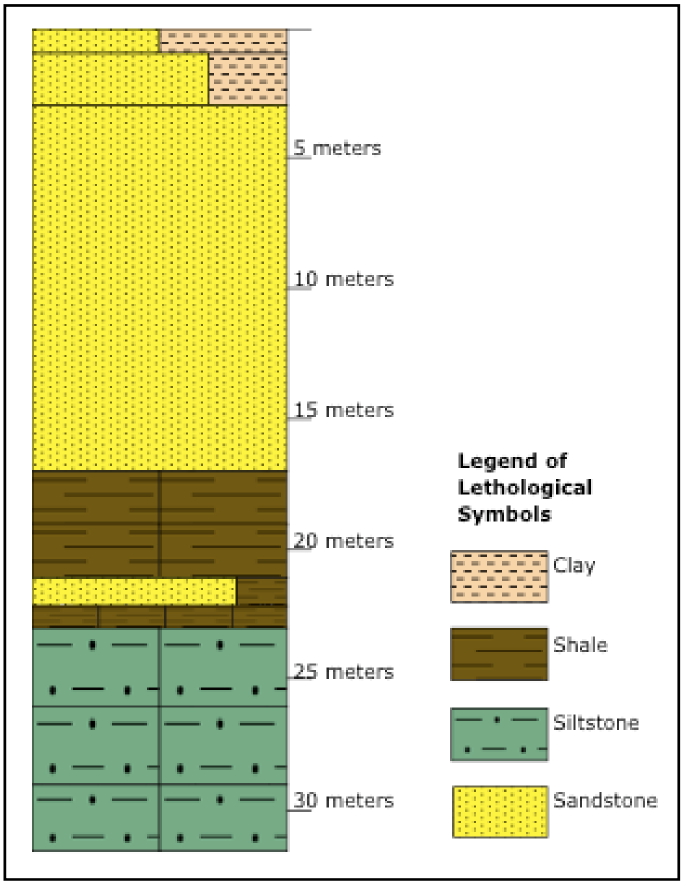

Figure 3-5. Lithology log from the Priddis well.

Table 3-2. Average interval P-wave velocities (from the sonic log).

Depth (m)	P-wave velocity (m/s)
0-3.9	Not Available
3.9-17.6	1900
17.6-28.3	2080
28.3-39.3	2250

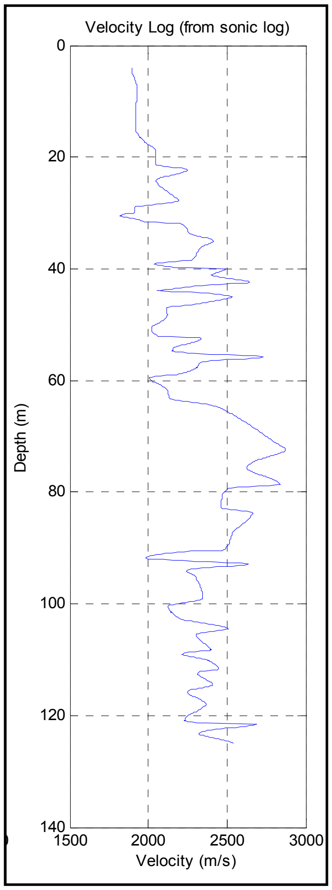

Figure 3-6. Velocity log (calculated from the slowness sonic log) in the Priddis well.

3.4 Data acquisition

Students of the 2007 University of Calgary Geophysics Field School and I have acquired refraction seismic data to be used for near-surface studies. The source used for this two-dimensional seismic line is a 12-pound sledgehammer. Single 10-Hz vertical geophones were used as receivers. A fixed array was used with 180 m spread length, and 72 receivers. Receiver spacing is 2.5 m, and source spacing is 12.5 m. Near offset ranges between 0 and 37.5 m. Figure 3-7 illustrates the field layout. The record length is 600 ms with 0.125 ms sampling rate. The record length is short, and that will negatively affect the accuracy of the inverted S-wave velocity profile of the near surface. Figure 3-8 shows a raw shot gather. Most of the energy on this shot gather is surface wave with no obvious body waves present.

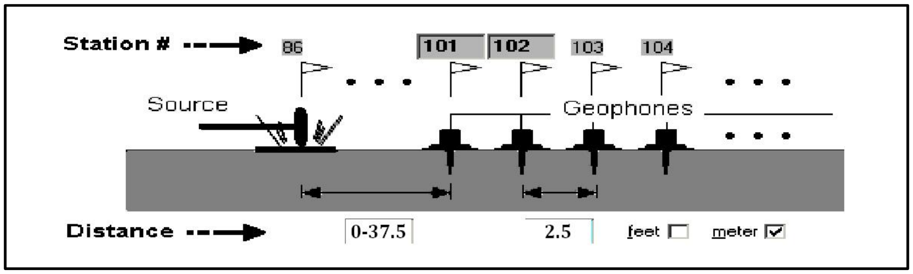

Figure 3-7. Field acquisition layout from the 2007 University of Calgary Geophysics Field School.

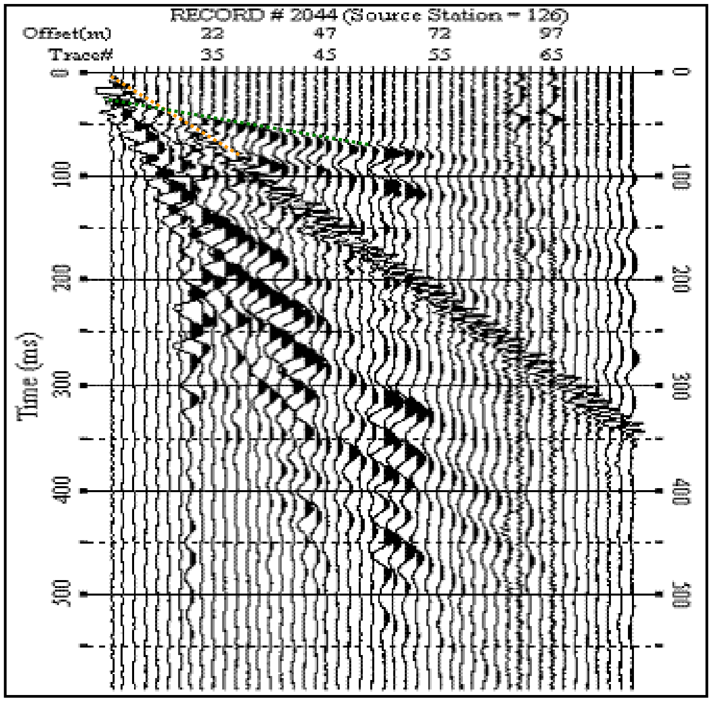

Figure 3-8. A raw shot gather, acquired with a sledgehammer source, and single vertical geophone from the the 2007 University of Calgary Geophysics Field School. Total record length is 600 ms. The orange dotted line show the direct arrivals, and the green dotted line show the refracted arrivals.

The P-wave velocity of the first layer is estimated to be 400 m/s from the direct arrivals (the reciprocal of the direct arrivals indicated by the orange dotted line in Figure 3-8). Also, the P-wave velocity of the second layer is estimated to be 1724 m/s from the refracted arrivals. The cross-over distance is 10 m. Therefore, substituting those values into equation (2.2) gives an estimate of 3.9 m for the first layer thickness.

3.5 Dispersion curves

A dispersion image, for the shot gather shown in Figure 3-8, was created using *SeisSurf 2.05* and shown in Figure 3-9. The dispersion curve, shown in Figure 3-9, has two strong amplitude trends. Our interpretation of the fundamental mode was the first strong trend that has lower velocities. The other strong trend, which has higher frequencies is the first higher mode.

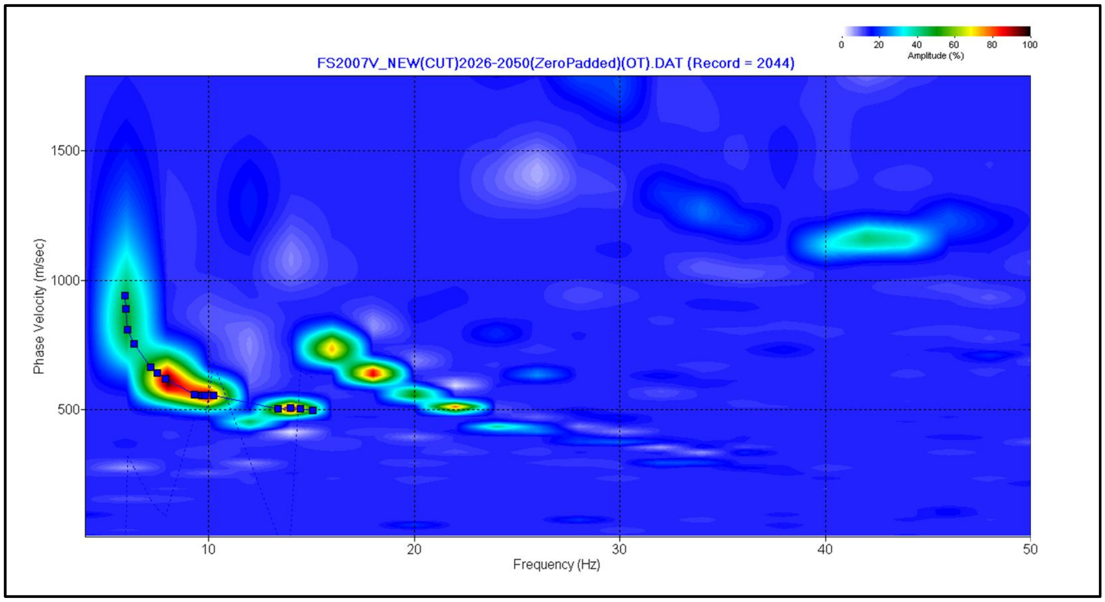

Figure 3-9. Dispersion curve of the shot gather shown in Figure 3-8. Fundamental mode is picked and indicated by the dark blue squares.

3.5.1 Velocity dispersion of Rayleigh waves

Having success in recording a significant amount of Rayleigh waves, we suspect lower frequencies will penetrate deeper, have greater phase velocity, and be more sensitive to deeper layers. Higher frequencies will have less phase velocity and are more sensitive to the physical properties of the near-surface layers.

The phase velocity of surface wave of a layered earth model is a function of frequency and four earth parameters, which are P-wave velocity (V_P), S-wave velocity (V_S), density (ρ), and the thickness (h). The Rayleigh waves propagate in several discrete modes. In the Priddis case, the phase velocity and the group velocity of each mode depend on frequency, and phase velocity is decreasing when the frequency increases. The dispersion image (Figure 3-9) shows normal dispersion of Rayleigh waves.

3.6 Inversion of dispersion curves

The P-wave velocities are calculated from the sonic log for five layers. A five-layer S-wave velocity model was then created by using a Poisson’s ratio of 0.405 to construct our initial S-wave velocity model that is shown in Table 3-3. This five-layer model is used as the initial guess model for the inversion. Figure 3-10 shows the initial model, indicated by the dashed blue line, against the inversion results for S-wave velocities, indicated by the solid blue line.

Table 3-3. Initial model. The bottom (depth) and thickness are in m. The P- and S-wave velocities are in m/s. S-wave velocity is calculated from P-wave velocity and a fixed Poisson's ratio of 0.405.

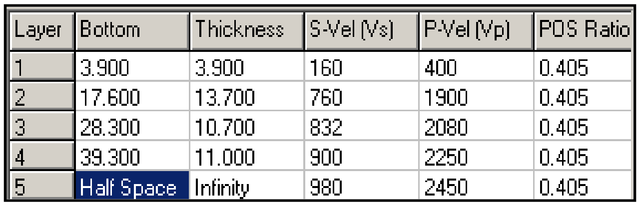

Layer	Bottom	Thickness	S-Vel (Vs)	P-Vel (Vp)	POS Ratio
1	3.900	3.900	160	400	0.405
2	17.600	13.700	760	1900	0.405
3	28.300	10.700	832	2080	0.405
4	39.300	11.000	900	2250	0.405
5	Half Space	Infinity	980	2450	0.405

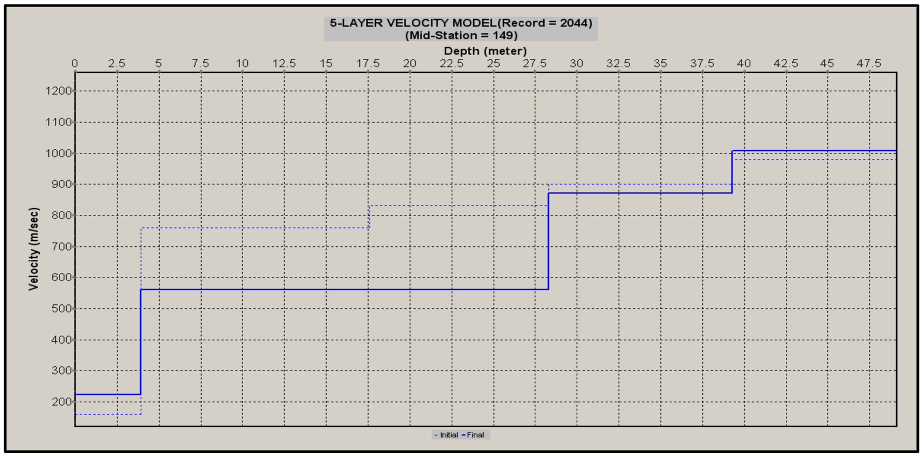

Figure 3-10. Inverted S-wave velocity indicated by the solid blue and initial S-wave velocity indicated by the dashed blue line.

A 2-D S-wave velocity profile is constructed by bilinear interpolation, where S-wave velocity values are interpolated first in depth, and then spatially between different locations. Stacking velocities are often interpolated by this method (Sheriff, 1991). Figure 3-11 shows a two-dimensional S-wave velocity profile across the line. S-wave velocities range from about 200 m/s to 1200 m/s, and generally increase with depth. This S-wave velocity profile can be related to the (a-a') segment of the elevation profile shown in Figure 3-4. The lithology log is positioned on the well location of the S-wave velocity profile, shown in Figure 3-11. The lithology log roughly correlates to the S-wave velocity profile.

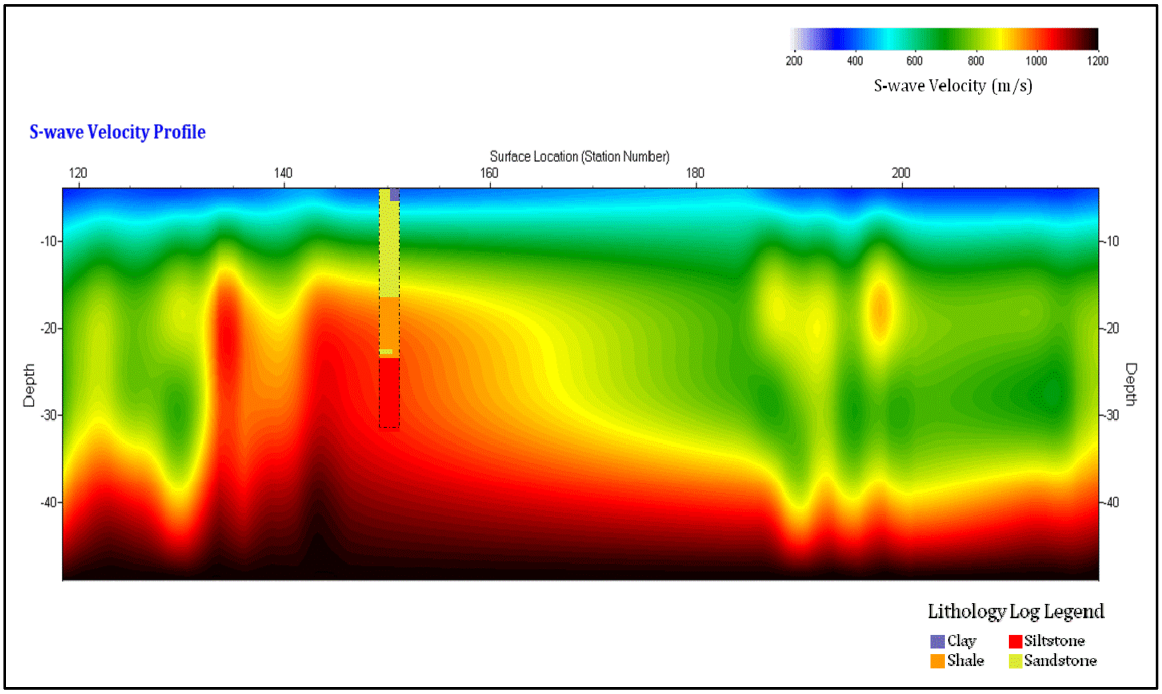

Figure 3-11. S-wave velocity two-dimensional profile. The lithology log is inserted inside the dashed black line at station number 150.

3.7 Discussion and conclusion

In this part of my thesis, I have investigated the near-surface lithology of the Priddis site by examining and describing rock cuttings collected during the drilling of a shallow test well. Also, I applied the MASW method to a 2-D seismic line (with 2.5 offset from the well) to obtain the near-surface S-wave velocity structure map. From this study, I conclude:

- In this real seismic data, Rayleigh waves show normal dispersive behaviour (higher frequencies have lower phase velocities) with low frequencies (~7 Hz) having an 890 m/s phase velocity, and high frequencies (~17 Hz) having a 490 m/s phase velocity.

- S-wave velocities are related to the lithology, and the S-wave velocity map (obtained by the MASW method) roughly correlates to the lithology log (obtained from the description of the well-cutting samples).

The record length of the seismic data, used for this study, was only 600 ms. For the MASW method, a record length of 2 seconds is recommended (Park, 2006), and 600 ms is relatively short. Therefore, using a longer record length would possibly improve the dispersion image used for the inversion.

CHAPTER FOUR: NEAR-SURFACE REFRACTION ANALYSIS AT THE SPRING COULEE SITE

4.1 Introduction

In January 2008, an extensive 2D multi-component seismic survey was acquired by the CREWES Project in the Spring Coulee, Alberta area. The mineral rights to the land are owned by the University of Calgary. The objective of the survey was to explore for potential hydrocarbon within the land. The data used for the near-surface study in this chapter are from one of those lines.

The Spring Coulee area is located in southern Alberta west of the town of Magrath, as shown in Figure 4-1. The 2D-3C seismic line, used for this study, is indicated by the red line on the surface geology map, shown in Figure 4-1. The surface geology of the site consists of the St. Mary River sandstone, and shale. The St. Mary River Formation is in the upper Cretaceous.

The purpose of this study is to create P-wave and S-wave near-surface models of the earth using the refraction methods. A Generalized Linear Inversion (GLI) algorithm is used for the inversion of first arrival time picks by GLI3D (Hampson-Russell Software). Those models will be compared, and then used later in this thesis for calculating and then applying static corrections.

4.2 Acquisition parameters

The line used here is a 2-D line, about 6.54 km long, which goes from northeast to southwest. A dynamite source of 2 kg in weight and buried at depth of 16 m was used for the shots. Receivers were single 3-component geophones. Receiver spacing was 10 m, and the shot interval was 30 m. A total of 654 live receivers for 54 shots compose the data. Figure 4-2 shows shot locations, indicated by light blue, and receiver locations, indicated by black. The shots are in the middle of the line, and cover 25% of the line. The fold map is shown in Figure 4-3: the full fold is 54. Figure 4-4 show the elevation profile across the line. The elevation range is about 150 m, and the line is lower to the north-east and higher to the south-west.

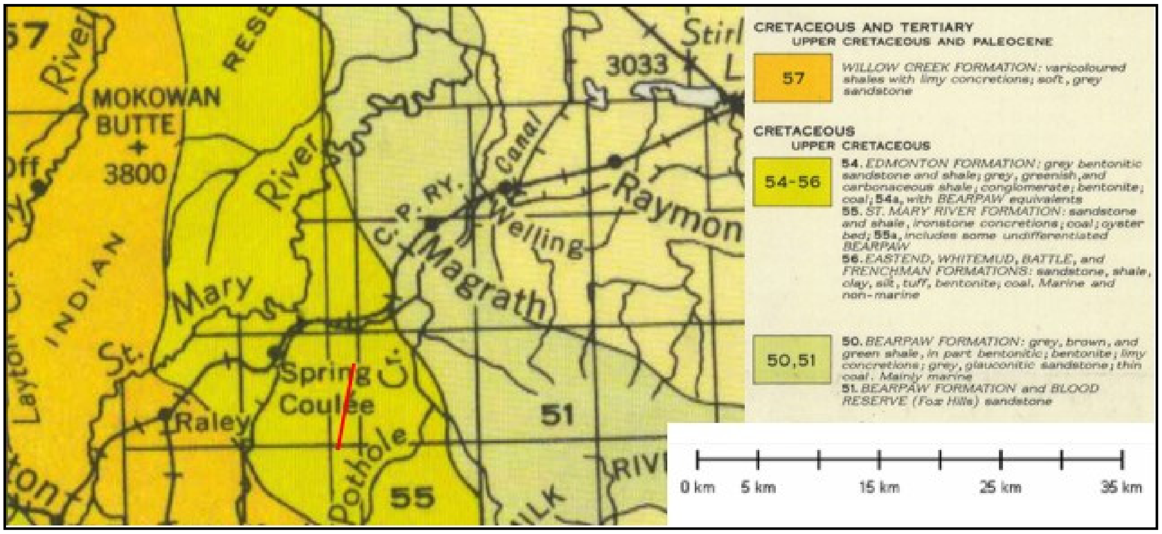

Figure 4-1. Location and surface geology map. The seismic line is indicated by the red line (Modified after Geological Survey Division, 1951).

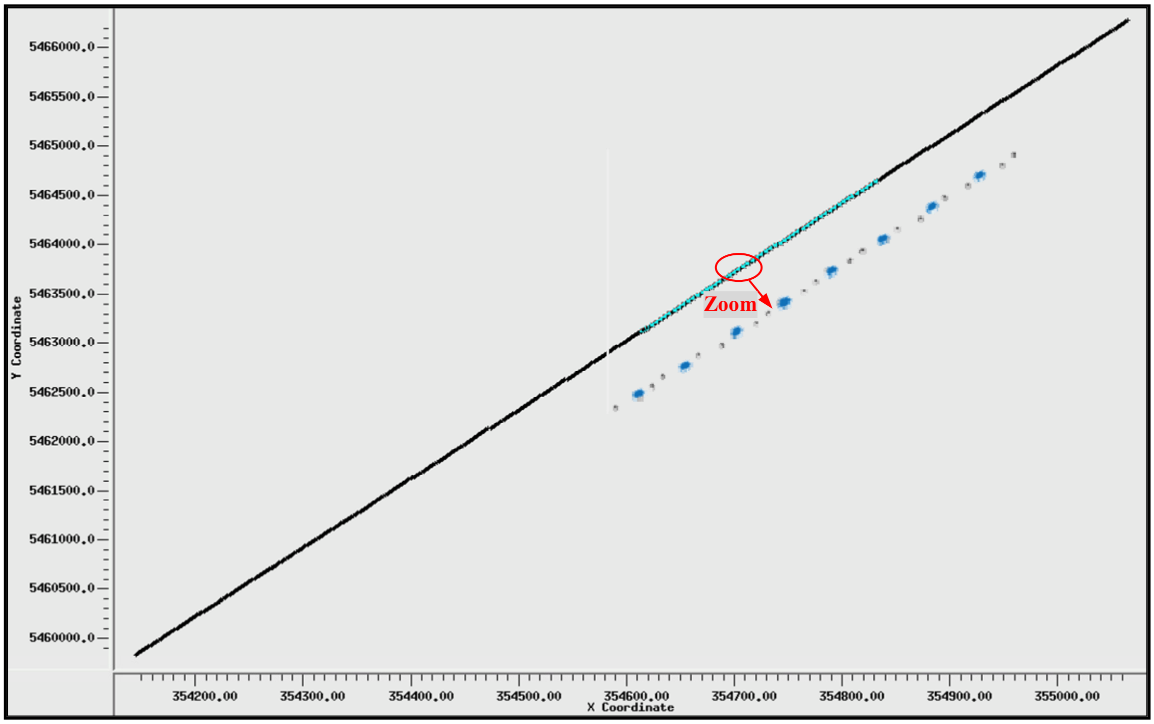

Figure 4-2. Shot locations in light blue, and receiver locations in black. Vertical and horizontal axes are Y and X coordinates respectively.

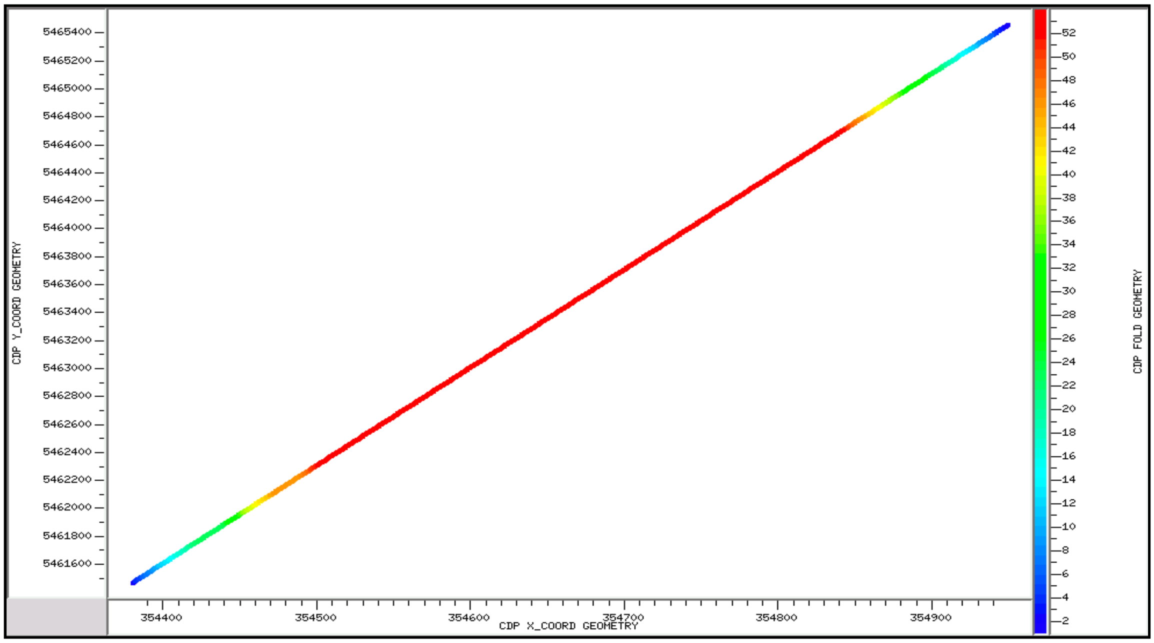

Figure 4-3. Fold map. The color bar indicates the CDP fold. Vertical and horizontal axes are Y and X coordinates respectively.

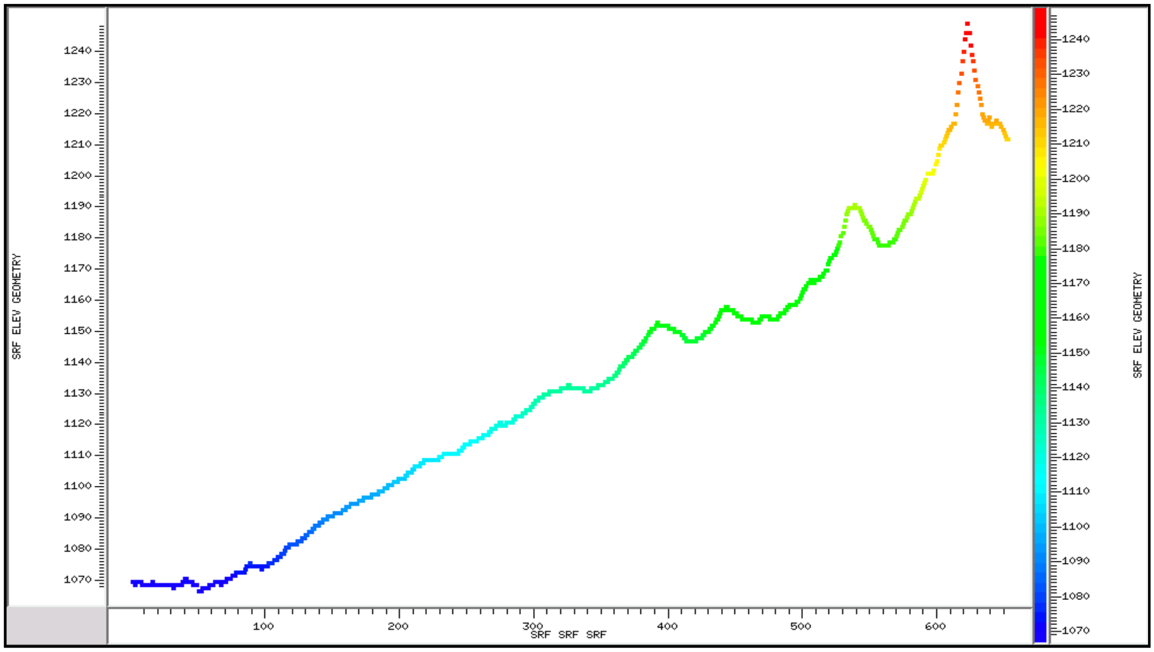

Figure 4-4. Elevation profile. The vertical axis is elevation above sea level in m, the horizontal axis is the station number, and the color bar indicated elevation.

4.3 Method

Refraction methods are the most widely used methods for determining thicknesses and velocities of the near-surface layer. This method requires accurate picks of first arrival times. The process workflow to create P-wave and S-wave near-surface models of the earth using the refraction methods is divided into two parts: (1) Identifying time-offset pairs for first P- and S-wave arrivals in ProMAX, and (2) Deriving near-surface earth model in GLI3D.

4.3.1 Identifying time-offset pairs for first arrivals

The process workflow for identifying time-offset pairs for first P-wave and S-wave arrivals is shown in Figure 4-5. The SEG-Y file, containing the data, was read in ProMAX, and then geometry was built for the data. Figure 4-6, and Figure 4-7 show the vertical- and radial-components respectively of the one shot with amplitude and phase spectra. From the amplitude spectra, I consider the useful frequency band for the vertical-component to be 8 to 80 Hz, and to be 5 to 30 Hz for the radial-component.

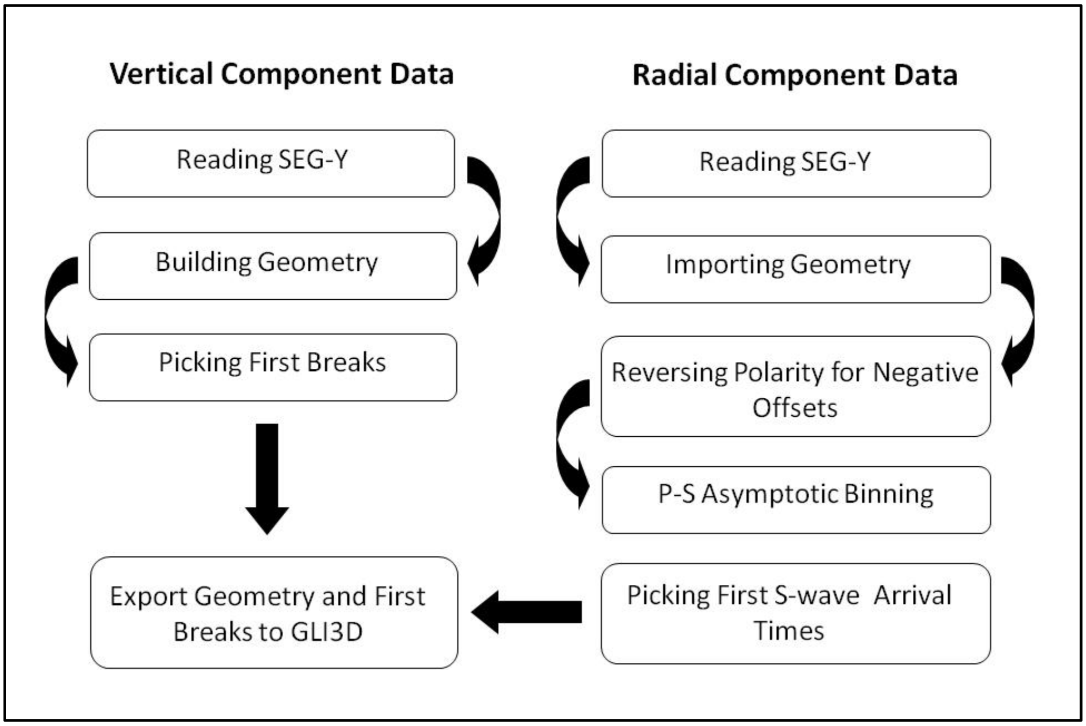

Figure 4-5. Workflow Part (1): Identifying time-offset pairs for first P-wave, and S-wave arrivals in ProMAX.

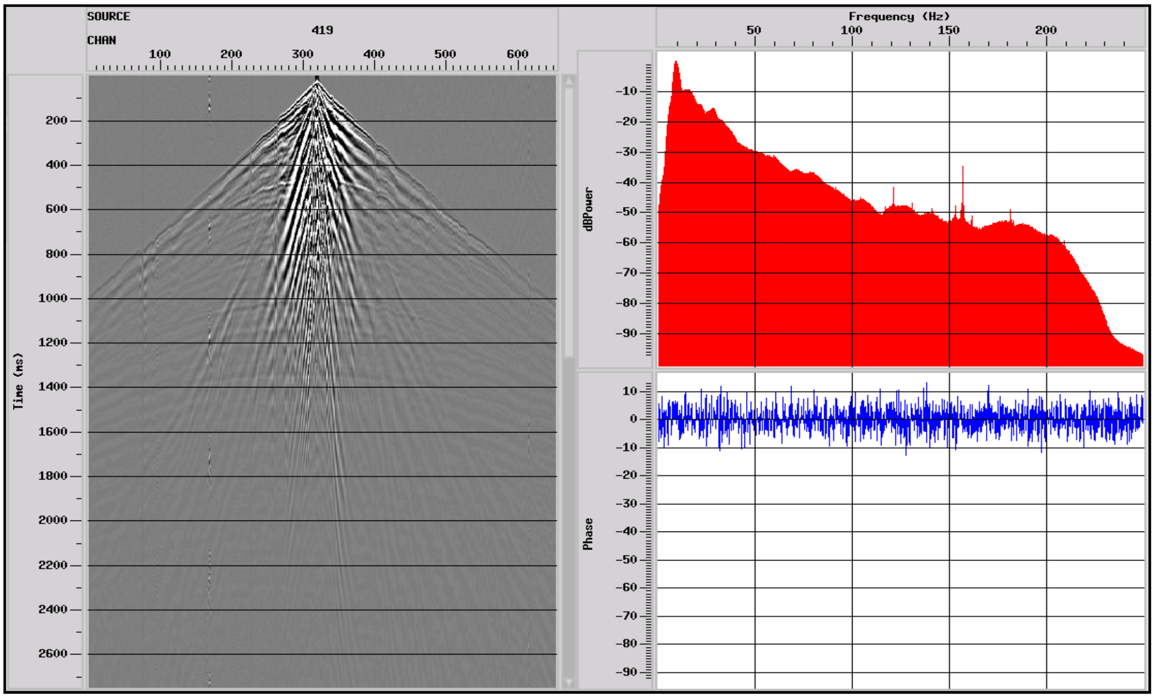

Figure 4-6. A vertical shot gather (left) with its amplitude (upper right) and phase spectra (lower right).

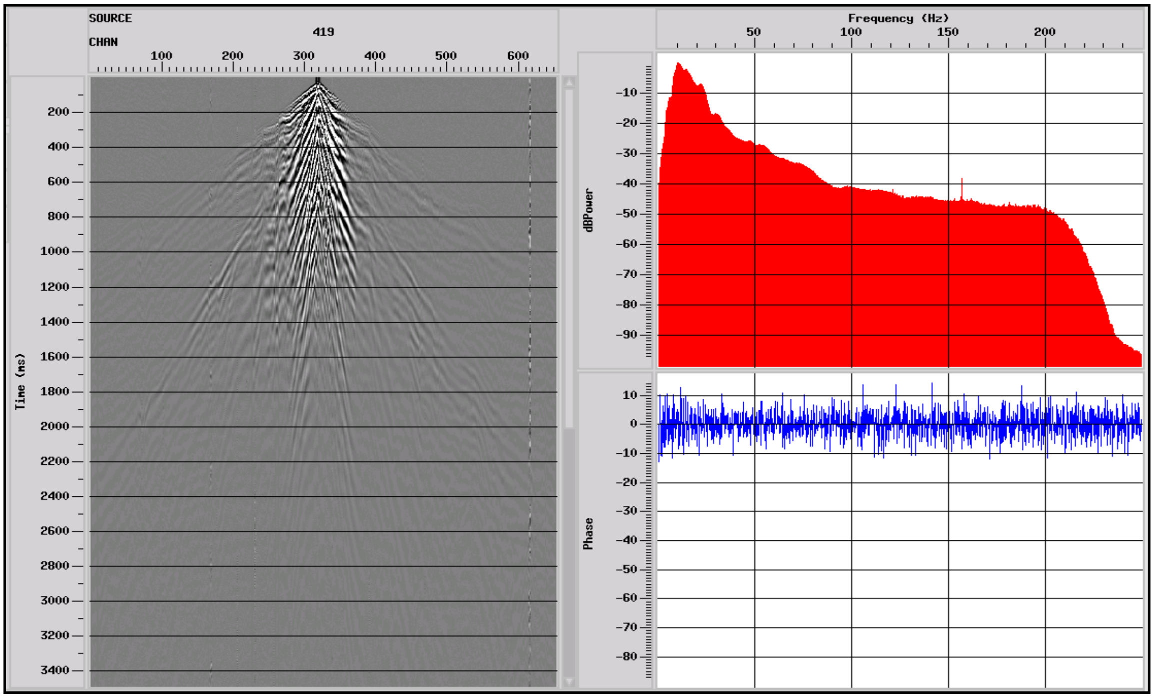

Figure 4-7. A radial shot gather (left) with its amplitude (upper right) and phase spectra (lower right).

For vertical and radial components, bad traces had to be killed for all shots. Then, for the radial component, the polarity of traces on the left side of the sources is reversed. That is because on radial-component shots, traces from different sides of the source have opposite polarity. For example on Figure 4-8, the first breaks are troughs on the left side of the source, and are peaks on the right side of the source. Reversing traces, which are to the left of source, will make all first breaks peaks, making the polarity consistent for the entire gather.

The CDP (Common Depth Point) location is different than the CCP (common conversion point) for the same source-receiver pair, and that is because P-wave velocity is different than that of S-wave. To account for the conversion point movement when gathering and stacking the data, the method of P-S asymptotic binning is used. The conversion offset, x_c, is approximated by

$$x_c = \frac{x(V_p / V_s)}{1 + (V_p / V_s)}, \qquad (4.1)$$

and 1.9 is used for V_p / V_s. 1.9 is a typical value of V_p / V_s in southern Alberta. Figure 4-9 shows the fold build-up for the vertical-component data, and Figure 4-10 shows the fold build-up for the radial-component data after the asymptotic approximation.

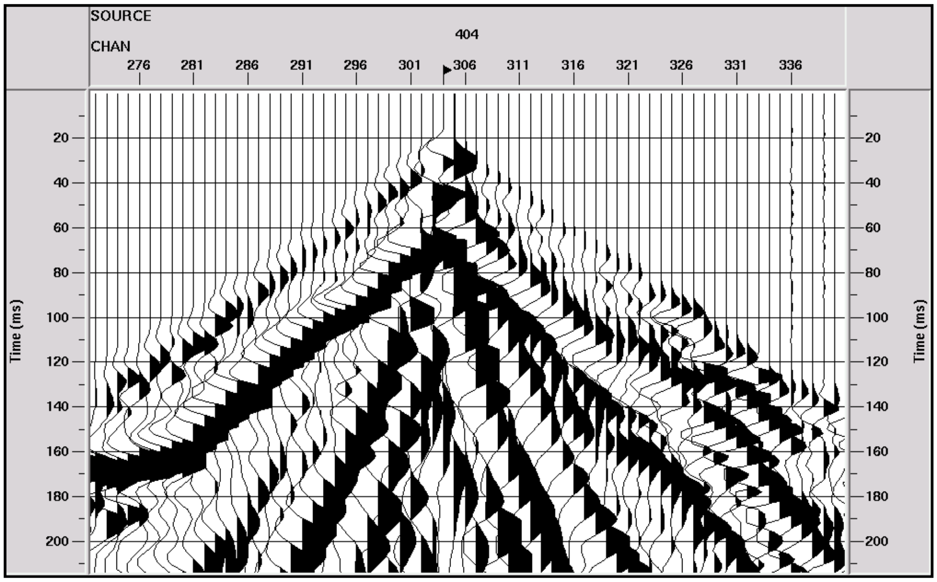

Figure 4-8. A radial-component shot gather with opposite polarity on different sides of the source.

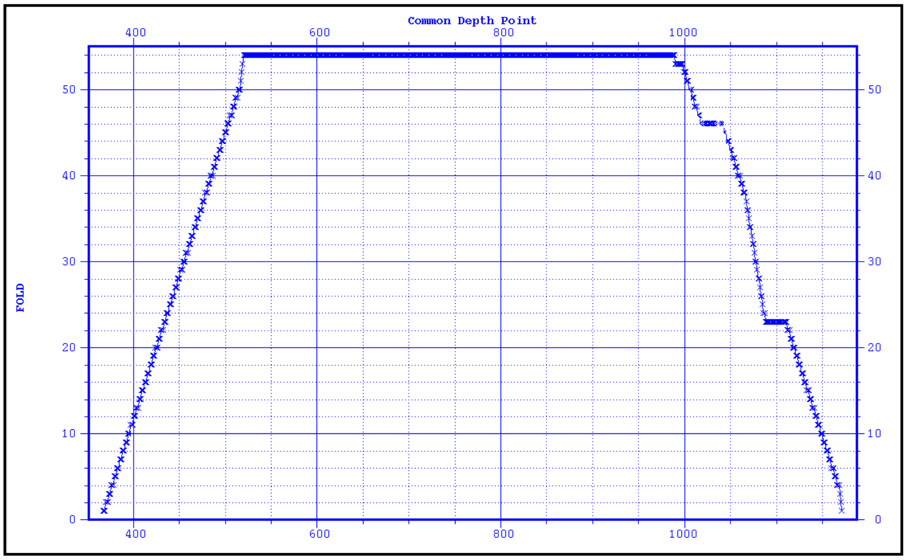

Figure 4-9. Vertical-component data fold.

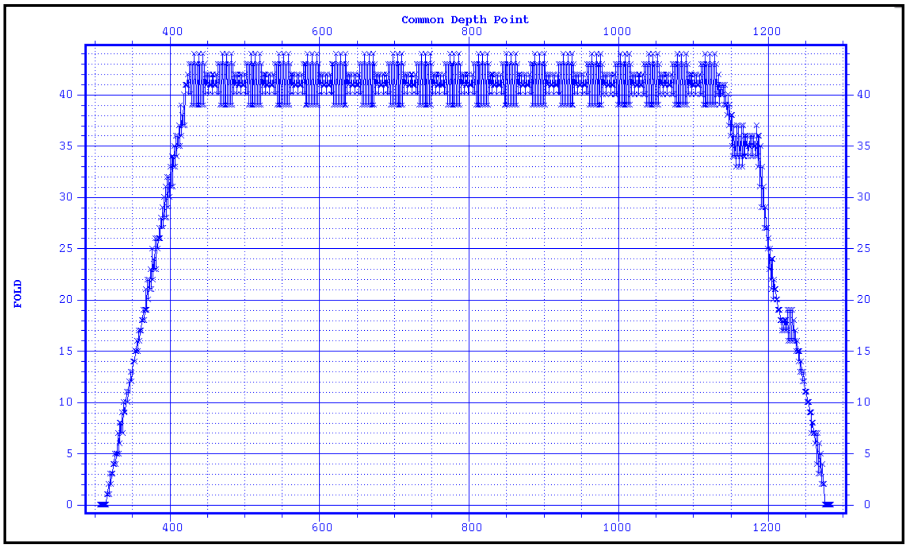

Figure 4-10. Radial-component data fold.

For signal enhancement, AGC (Automatic Gain Control) was applied for amplitude recovery. A bandpass filter was applied to vertical- and radial-component data. The four frequencies used for the bandpass filter were 10, 14, 60, and 80 for the vertical component data, and 4, 10, 20, and 30 Hz for the radial-component data.

First P-wave arrivals are picked for a vertical-component shot, as shown in Figure 4-11. The slope of pulses that travel directly from source to receiver with the velocity of the first layer is hard to estimate. Beyond the critical distance, first arrivals are refractions. Two slopes of first arrivals, which can be seen in Figure 4-11, correspond to the velocity of the first refractor (second layer), and the velocity of the second refractor (third layer). Velocities of the first and second refractors are 2750 m/s, and 3536 m/s respectively. P-wave first arrivals were picked automatically for all vertical-component shots, and then edited manually.

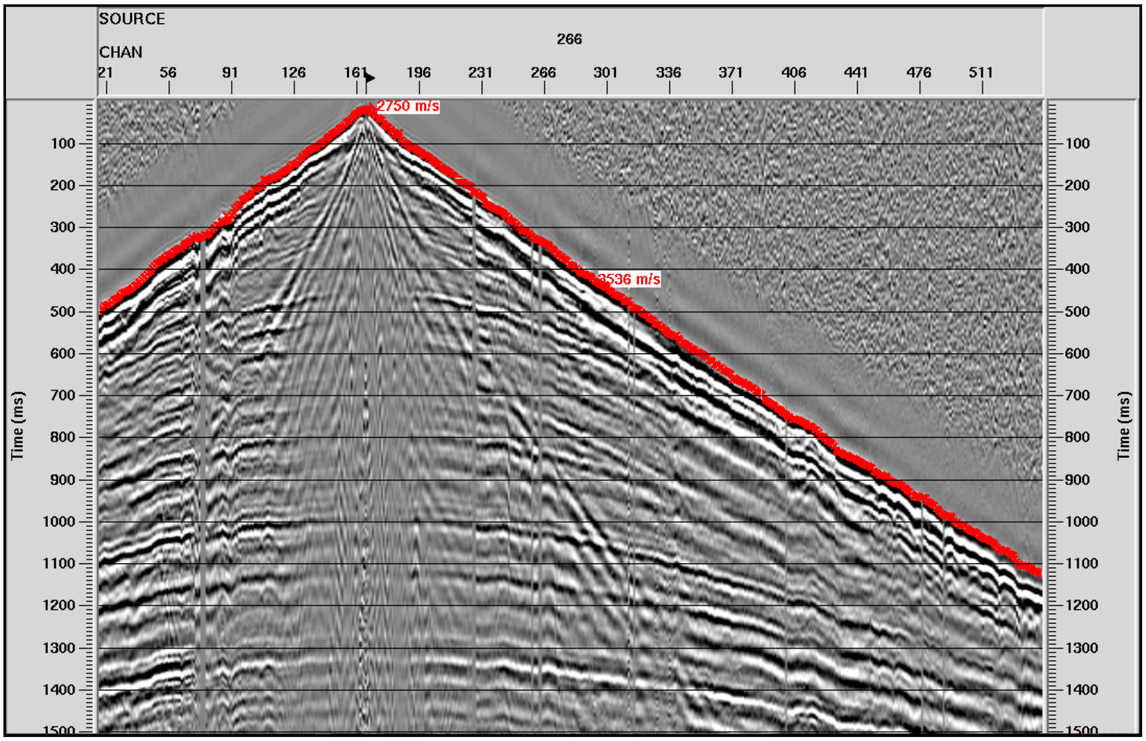

Figure 4-11. First P-wave arrivals on vertical-component data. Slope velocities (apparent) are annotated.

A similar procedure was applied to pick the first S-wave arrivals in a radial-component shot; the results are shown in Figure 4-12. The velocities of the first and second S-wave refractors are 1307 m/s, and 1601 m/s, respectively. It is easy to confuse first S-wave velocity arrivals with Rayleigh waves, due to velocities being very close. Therefore, special care has to be taken when picking first S-wave arrivals, and automatic picking is not effective. To confirm S-wave picks, hodograms of S and Rayleigh waves were analyzed. Hodograms are plots of the motion of the particles as a function of time, and can be useful in multi-component recordings (Sheriff, 1991).

For hodogram analysis, all three components (vertical, radial, and traverse) of the seismic data were read from the SEG-Y files, and then geometry was assigned. To create hodograms, a time window was designed around the event to be analysed. An example hodogram created for this window is shown on Figure 4-13.

Three panels are shown on Figure 4-13. The first panel shows the S-wave first arrival at one geophone position recorded as three-component traces, the second shows the traces after horizontal rotation, and the third shows the traces after both horizontal and vertical rotation. On the upper right is the horizontal plane. This plane and the horizontal traces after horizontal rotation are used to find the orientation of the pure radial. After that, the vertical plane and the traces after both horizontal and vertical rotation are used to trace the particle motion as function of time, as is shown on the lower right panel. The particle motion is mostly horizontal and perpendicular to the propagation direction, characteristic of S-wave energy.

Another window was designed for Rayleigh waves also using the radial component trace, and shown in Figure 4-14. Using this window and all three components, the hodogram was created and shown on Figure 4-15. The particle motion on the vertical plane (displayed the lower right of the Figure) is elliptical, characteristic of a Rayleigh waves.

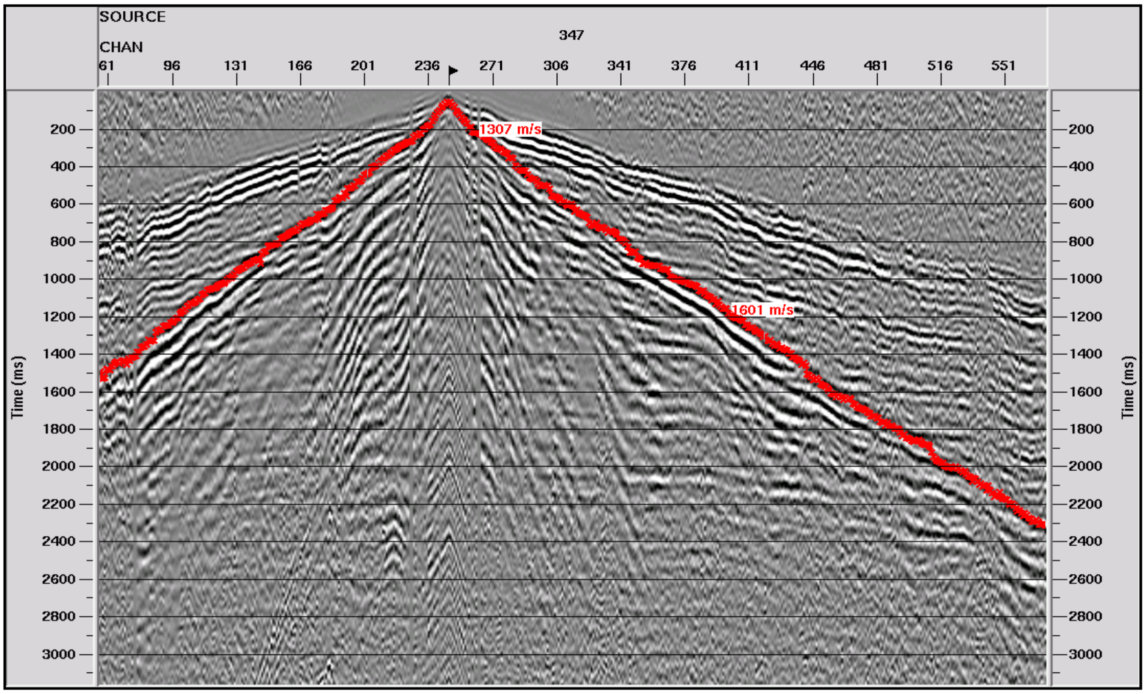

Figure 4-12. First S-wave arrivals on radial-component data. Slope (apparent) velocities are annotated.

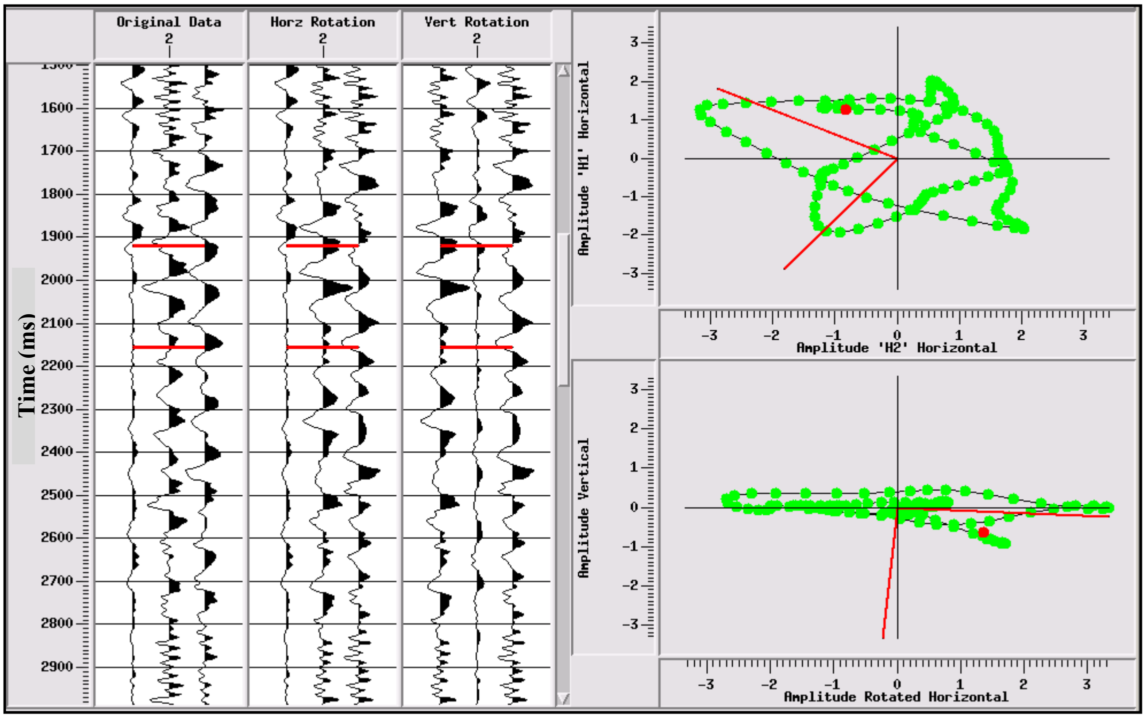

Figure 4-13. S-wave hodogram. Red lines on left define the hodogram window.

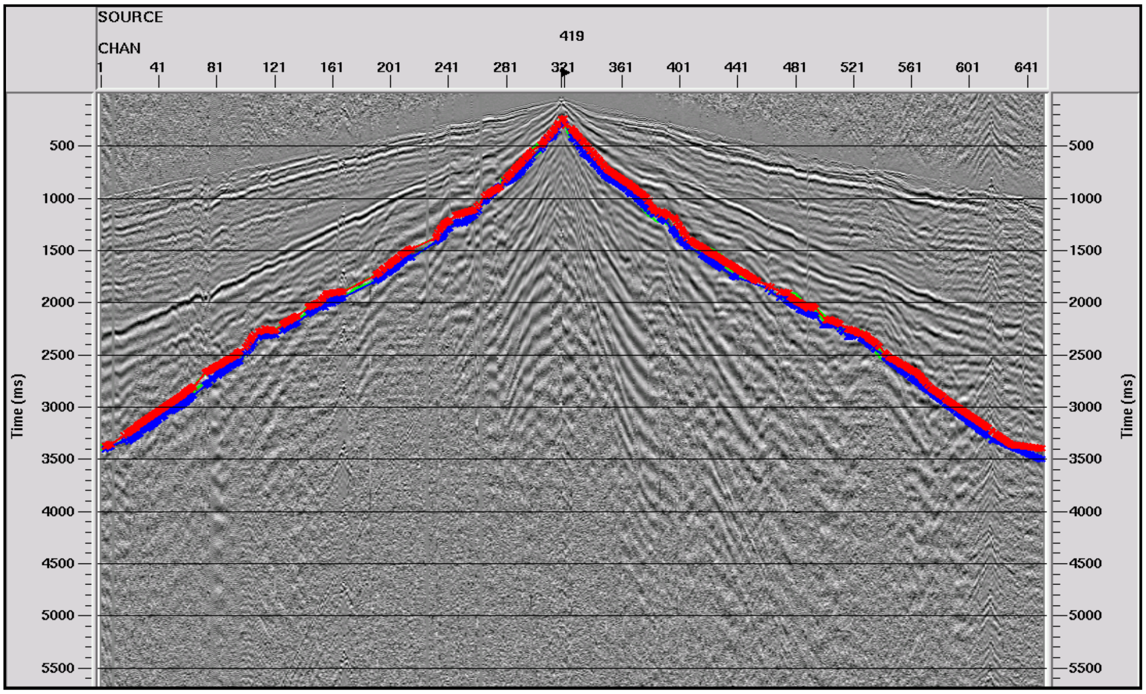

Figure 4-14. Rayleigh waves observed on a radial-component common shot gather.

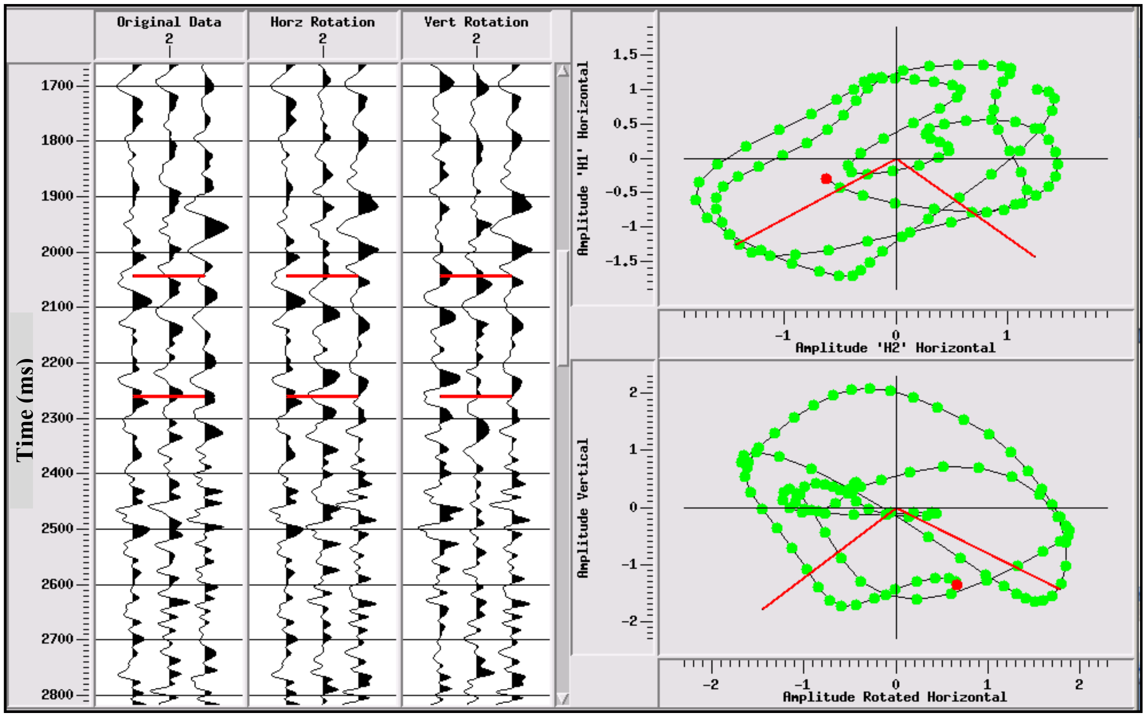

Figure 4-15. Rayleigh-wave hodogram. Red lines on left define the hodogram window.

After picking all first P-wave arrivals on vertical-component shot gathers, and all first S-wave arrivals on radial-component shot gathers, geometry and first arrival picks were exported to GLI3D for refraction analysis to obtain near-surface layers thicknesses and velocities.

4.3.2 Generalized Linear Inversion of first arrivals

The Generalized Linear Inversion (GLI) method by Hampson and Russell (1984) consists of estimating an initial near-surface velocity model from observed first arrival times in a manner similar to that used in Chapter 2. Then, using that initial velocity model, theoretical first arrival times are calculated by ray-tracing. If the initial velocity model was right, then observed time breaks and model time breaks would match. Otherwise, corrections to the initial model are needed to improve the fit between observed breaks and model breaks (Hampson and Russell, 1984). See the workflow shown on Figure 4-16. Our goal here is to produce a velocity model for which first break times calculated by ray-tracing will be close to the observed first break times.

If P_k are the observed breaks, and T_k are the model breaks, then the inverse problem is found by minimizing the objective function, J

$$J = \sum_{k} (P_k - T_k)^2 ,$$

$$T_k = M_k(E, D_i, v_i) , \tag{4.2}$$

where E, D_i, and v_i are model parameters. The model parameters, $E(x)$, $D_i(x)$, and $v_i(x)$, are continuous functions denoting the elevation of the free surface, the elevation of the base of the i^{th} layer, and the velocity of the i^{th} layer, respectively (Yordkayhun, 2007).

Similar to most inverse problems, two problems arise when solving Equation (4.2). The first is the non-uniqueness problem: more than one set of model parameters will minimize J. The trade-off between the thickness and the velocity is the main source for the non-uniqueness problem. However, if the main goal is to use the near-surface velocity model to solve the statics problem, then the trade-off between layer thickness and velocity is not serious. However, it may be serious for near-surface imaging purposes. The second problem is that Equation (4.2) is non-linear in the unknown parameters. This problem is solved by Generalized Linear Inversion, where the equation is linearized in the vicinity of initial guess, and the thickness and velocities of the layers is updated. This procedure will be repeated until some acceptable agreement between observed breaks and model breaks is reached (Hampson-Russell Software Services Ltd., 2004).

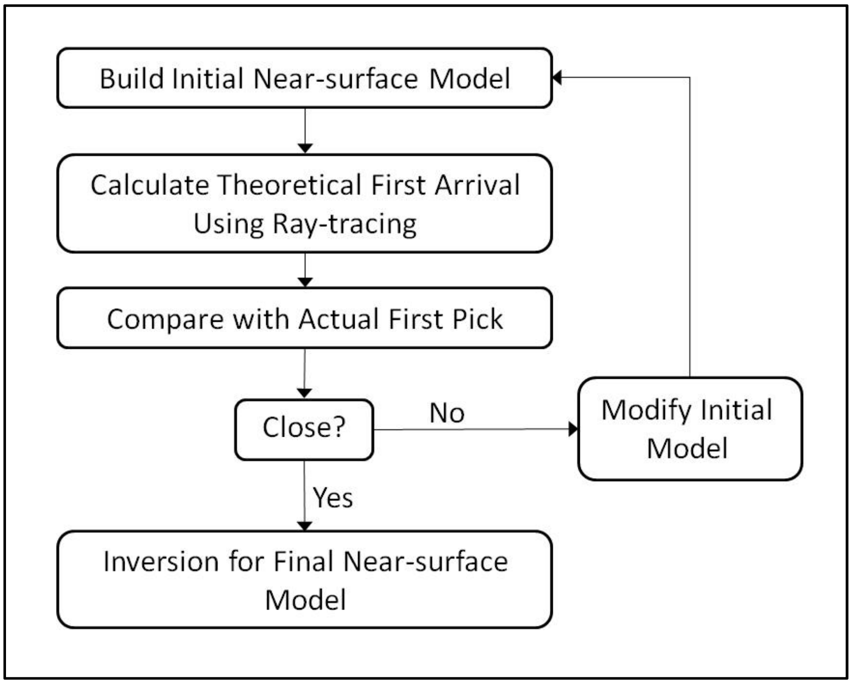

Figure 4-16. Workflow Part (2): Deriving near-surface earth model in GLI3D (modified after Hampson and Russell, 1984).

P-wave first arrivals were picked for all vertical-component shot gathers, and then imported to GLI3D. Similarly, S-wave first arrivals were picked for all radial-component shot gathers, and then imported to GLI3D. The first P-wave arrivals and first S-wave arrivals are shown in Figure 4-17 and Figure 4-18 respectively. The travel times of the S-wave first arrivals are significantly larger than those of the P-wave (as expected).

Then, the initial depth-velocity model for P waves is constructed by analyzing curves of first break arrival times versus offset for each vertical-component shot. Those curves were fitted with three straight lines, in effect limiting our desired P-wave velocity model to 2 near-surface weathered layers overlying a half space. From the straight lines, I can estimate starting values for the layer velocities and thickness as well as the half-space velocity. The initial model is critical for obtaining a good final model, because the nonlinear equation is solved by iterative linear inversion, and the solution is not guaranteed to yield an acceptable minimum of the objective function *J* if a poor initial model is used to begin the inversion (Yordkayhun, 2007).

I fixed the velocity of the first layer at 900 m/s, a value typical of the P-wave velocity of the unconsolidated overburden layer in southern Alberta. This gave me the initial P-wave velocity-depth model shown on Figure 4-19.

Similarly, for the S-wave refraction events for each radial-component shot gather, the S-wave first arrival times versus offset curves were fitted with three straight lines from which I can estimate thicknesses and velocities of 2 near-surface layers and the velocity of the base of weathering. The number of layers turned out to be the same for the P-wave and the S-wave case, but this is not always the case. I assigned a fixed velocity value of 420 m/s to the topmost unconsolidated overburden layer. This gave me the initial S-wave velocity model shown on Figure 4-20.

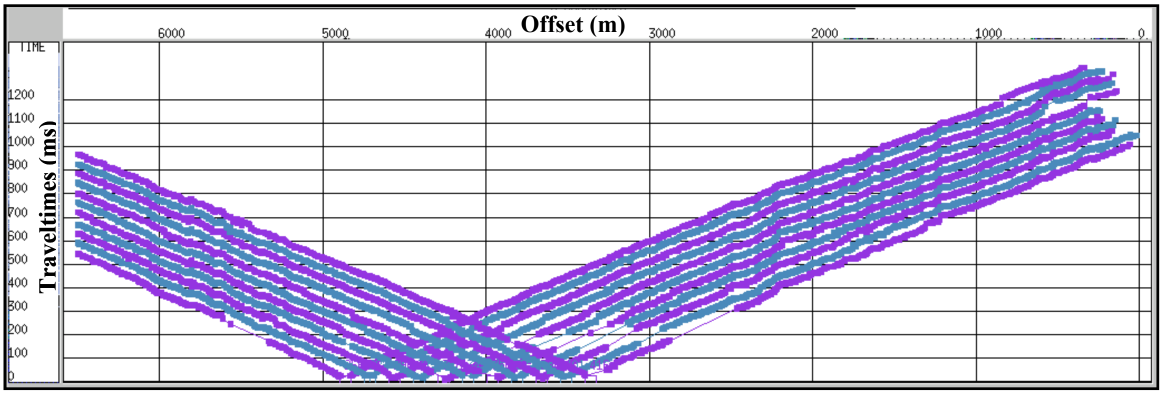

Figure 4-17. P-wave first arrival times in ms versus offset in m from vertical-component data.

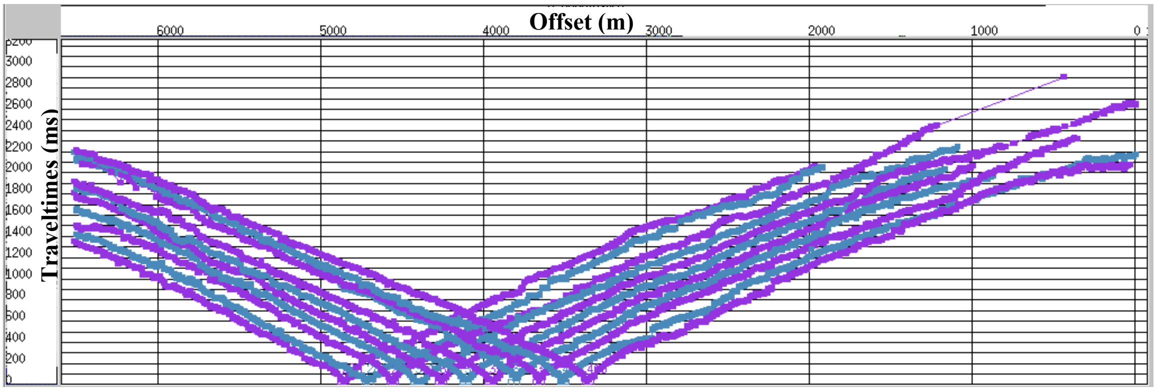

Figure 4-18. S-wave first arrival times in ms versus offset in m from radial-component data.

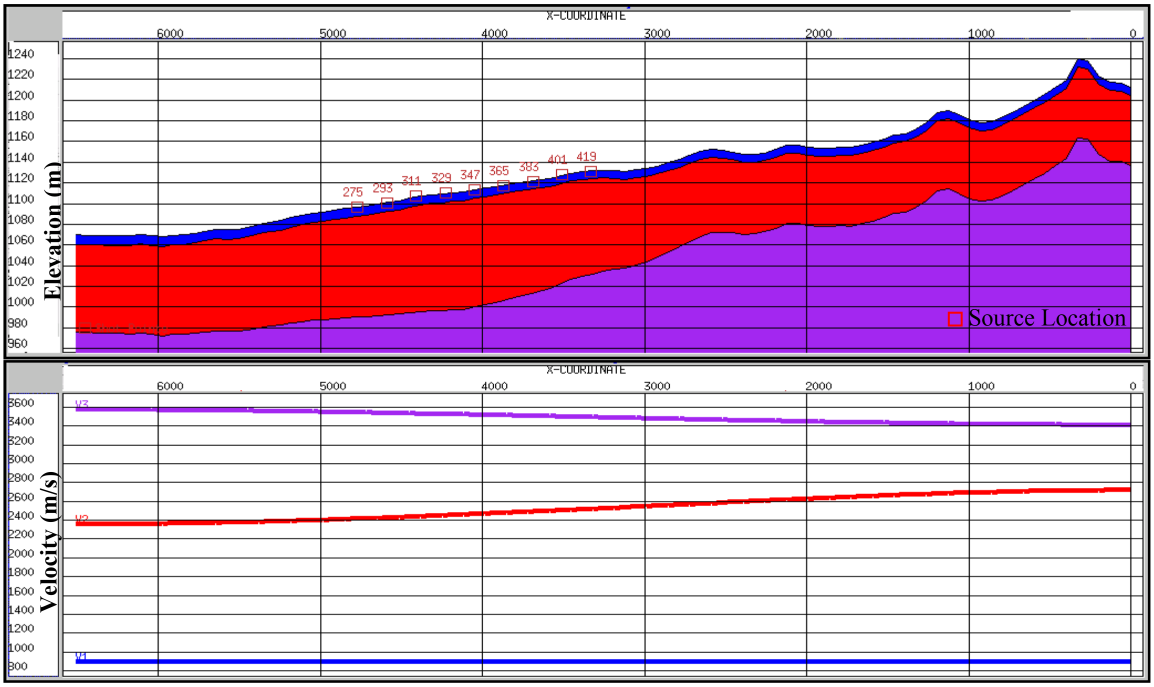

Figure 4-19. Initial P-wave earth model (upper), and P-wave velocity profile (lower).

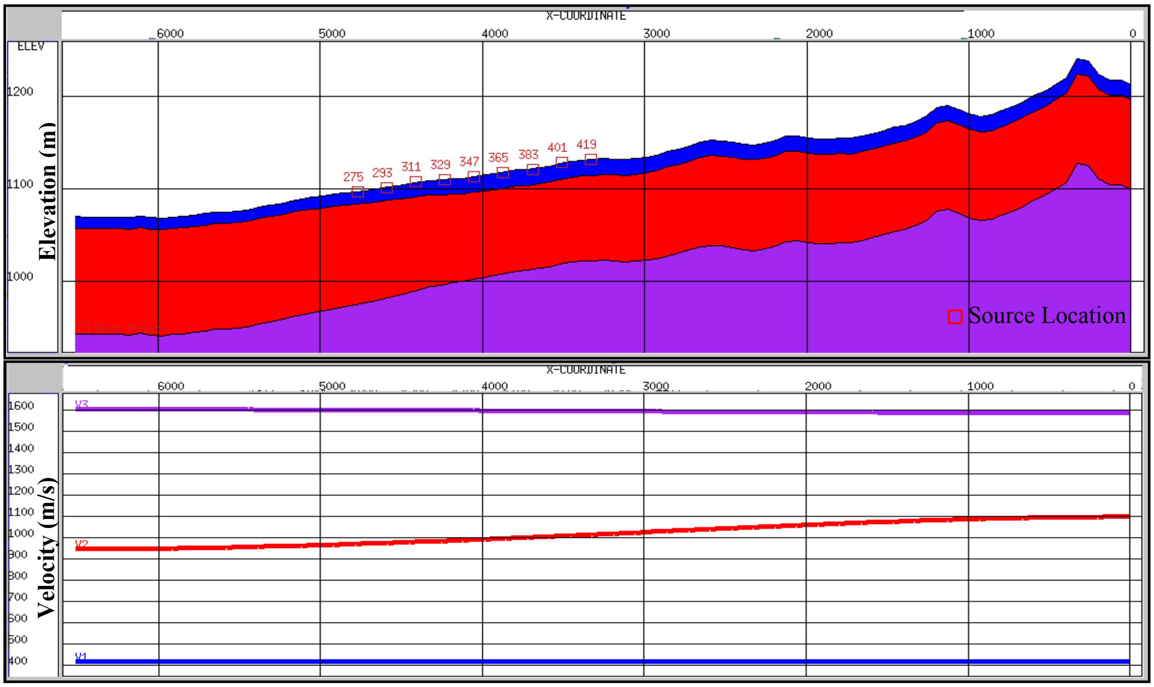

Figure 4-20. Initial S-wave earth model (upper), and S-wave velocity profile (lower).

By comparing the two initial P-wave and S-wave velocity-depth models, two conclusions can be drawn. The first one is that S-wave velocities are significantly smaller than P-wave velocities (as anticipated), about 37% to 47% of P-wave velocities. Therefore, the static correction values are expected to be larger for S-waves than for P-waves. The second is that the velocity layering and the base of weathering are not identical in the P- and S-wave initial velocity models but have similar trends. It is possible that the inverted model will have different velocity layering and base of weathering for P-waves and S-waves.

4.4 Results

The model time breaks, T_k, are calculated from the initial model by ray-tracing, and then compared to the observed breaks, P_k. Normally, the model times will be in error, and velocities and thicknesses need to be modified. The error is found by subtracting the model breaks from the observed breaks. The correction or the update to the model can be estimated by analyzing the error. The update is generally calculated by the Gauss–Seidel and conjugate-gradient algorithms (Hampson-Russell Software Services Ltd., 2004). A series of iterations is performed until the model breaks and the observed breaks are in some agreement. For the P-wave and S-wave cases, three update iterations were needed to give acceptable fits. The final P- and S-wave velocity-depth models are shown in Figure 4-21 and Figure 4-22, respectively.

Comparing Figure 4-19 and Figure 4-21, we see that the velocities, the velocity layering, and the base of weathering are all different for the initial and final models. At the top of the hill the unconsolidated overburden layer is absent, which could be interpreted as erosion. In addition, the near-surface velocity converges to the base of weathering velocity, and that is due to the geological uplift of more consolidated materials. Unlike the initial model, the base of weathering in the final model does not follow the elevation trend. When comparing the initial and final velocity-depth earth models of the S-wave (Figure 4-20 and Figure 4-22), it is obvious that the near-surface velocities are higher. Again, the base of weathering in the final S-wave velocity model does not follow the elevation trend in the final depth-velocity model.

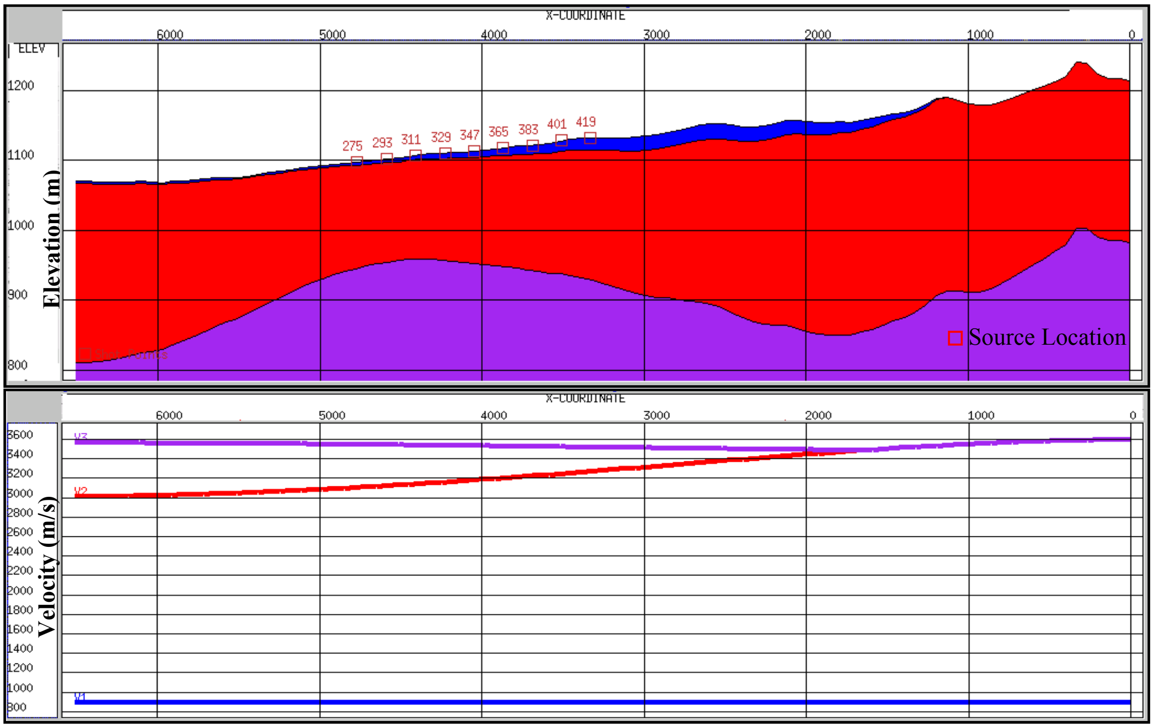

Figure 4-21. Earth model for P-wave (upper), and P-wave velocity profile (lower).

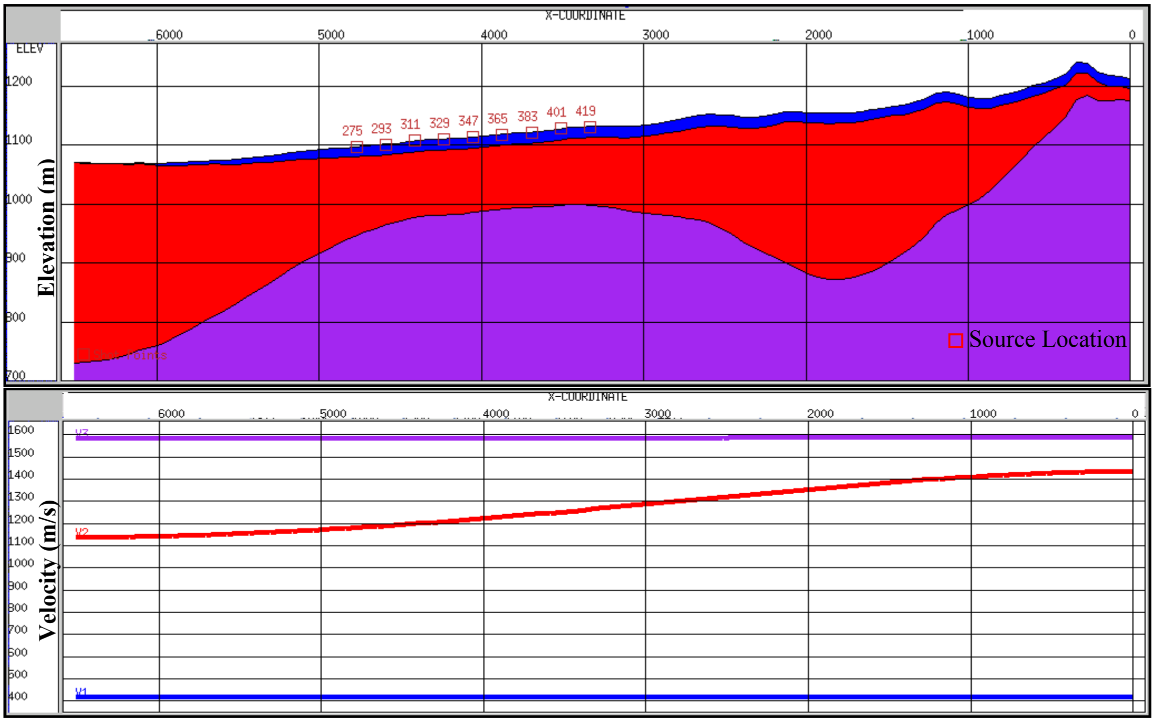

Figure 4-22. Earth model for S-wave (upper), and S-wave velocity profile (lower).

From the P- and S-wave velocity near-surface model, P- to S-wave velocity ratios (V_P/V_S) and Poisson's ratios (σ) were calculated for different stations at different elevations using equation (1.4) and shown in Table 4-1. In general, the P- to S-wave velocity ratios (V_P/V_S) of the sub-weathered layers (~2.6) are higher than the consolidated layers beneath (~2.25). According to a study of the St. Mary River formation in Spring Conlee-Magrath area, Alberta conducted by Williams (1951), the formation has a thickness of slightly less than 300 m and consists of clay, sandstone, and shale in the upper part. Castagna et al. (1993) showed that in shale, an increase in P-wave velocity from 3100 m/s to 3600 m/s can yield in a drop of V_P/V_S ratio from 2.2 to 1.9. In our cause, the higher values of the V_P/V_S ratios can be caused by clay content.

Table 4-1. P- to S-wave velocity and Poisson's ratios calculated from P- and S-wave near-surface models.

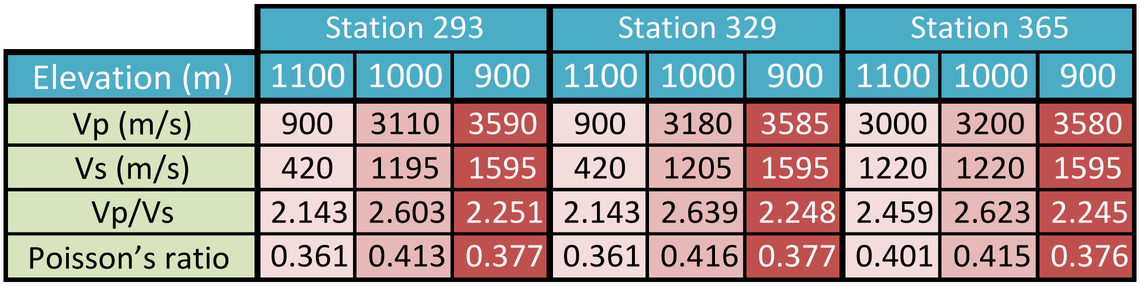

	Station 293			Station 329			Station 365		
Elevation (m)	1100	1000	900	1100	1000	900	1100	1000	900
Vp (m/s)	900	3110	3590	900	3180	3585	3000	3200	3580
Vs (m/s)	420	1195	1595	420	1205	1595	1220	1220	1595
Vp/Vs	2.143	2.603	2.251	2.143	2.639	2.248	2.459	2.623	2.245
Poisson's ratio	0.361	0.413	0.377	0.361	0.416	0.377	0.401	0.415	0.376

4.5 Discussion and conclusion

Refraction analysis using generalized linear inversion (GLI) of first-arrival times was applied successfully to the vertical and radial component of Spring Coulee data to obtain near-surface P-wave and S-wave velocity models. These near-surface velocity models were used to make static corrections for multi-component data.

Although the starting P-wave and S-wave velocity models used in the inversion process had the same structure and trend, the final inverted models had different velocity layering and different base of weathering. Different velocity layering and base of weathering for P-wave and S-wave make static corrections of multi-component data more complicated.

The main challenge in applying refraction analysis to the radial data was identifying first S-wave arrival times and picking them. Existing automatic picking programs are not adequate for first S-wave arrival times. However, manual identification and picking of first S-wave arrivals is difficult and very laborious. For this reason, even though good S-wave velocity models for the near surface can be obtained by refraction analysis, a faster, more automated method for creating near-surface S-wave velocity models from field data is needed. In the next chapter, I will describe how multi-channel analysis of surface waves (MASM) can be used to more easily obtain the required near-surface S-wave velocity model.

CHAPTER FIVE: SURFACE-WAVE ANALYSIS OF THE SPRING COULEE SEISMIC DATA

5.1 Introduction

The Multichannel Analysis of Surface Waves (MASW) method was developed originally for geotechnical purposes. We aspire to use this method for the purpose of static corrections. It was used earlier in this thesis for estimating S-wave velocities on synthetic seismic data and on data from Priddis, Alberta. In this chapter, the method will be applied to some of the Spring Coulee 3C data to obtain S-wave near-surface model, suitable for calculating static corrections.

Our objectives are to:

- Construct a 2-D S-wave velocity profile of the near surface for calculating static corrections used in PS reflection imaging.
- Compare 2-D S-wave velocity profile obtained by MASW to the one obtained by the refraction method (GLI model).

To apply the MASW method to the Spring Coulee data, a special configuration of the data is required, before carrying over with the regular MASW process workflow which involves estimating phase-velocity dispersion curves for Rayleigh waves, and then inverting these dispersion curves to estimate S-wave velocity as a function of depth. Also, the dataset must be converted from SEG-Y format to the special KGS format required by SurfSeis 2.05. This formatting of the seismic dataset is done using a software module kindly supplied by the Kansas State Geological Survey.

5.2 Method

The MASW method is applied to part of the Spring Coulee data. The MASW processing is performed in SurfSeis 2.05. The process work for MASW processing of Spring Coulee data is shown in Figure 5-1.

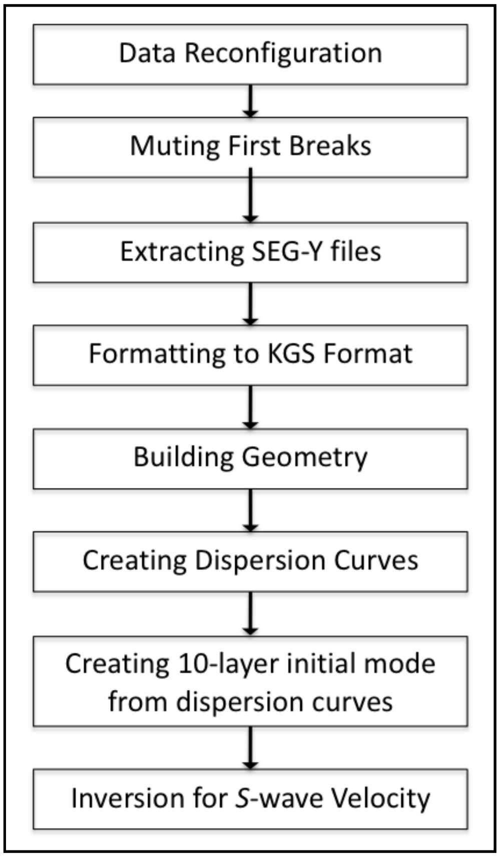

Figure 5-1. Process workflow of Spring Coulee MASW processing.

5.2.1 Data configuration

Although surface waves are dominant in seismic recordings, a recording configuration that favours the fundamental mode of surface waves is preferred for

MASW methods. A single low-frequency vertical geophone per channel is preferred over an array of geophones per channel (Park et. al, 1999). Rayleigh waves propagating within a short distance from the source generally act in a complex nonlinear pattern and should not be regarded as plane waves. Because of the near-field effects, Rayleigh waves of certain wavelengths can only be treated as horizontally-traveling plane waves after they travel a certain distance from the source, x_1 (Richart et al., 1970). According to Stokoe et al. (1994), plane wave propagation of surface waves usually occurs until the near-offset, x_1, exceeds half the maximum desired wavelength, $\lambda_{\max}$

$$x_1 \leq 0.5\lambda_{\max} . \tag{5.1}$$

In our case the length of the receiver spread (D) will be set to 300 m. The length of the receiver spread (D) determines the maximum useable wavelength (Park et al., 2006). The rule of thumb is that the penetration depth of surface waves is roughly equal to their wavelength, and the maximum depth of investigation, for which shear-wave velocity can be estimated, $z_{\max}$, is determined by half the longest wavelength

$$z_{\max} \leq 0.5\lambda_{\max} \tag{5.2}$$

(Park et. al., 1999). The receiver spacing, dx, determines the shallowest depth of investigation, $z_{\min}$ (Park et al., 2006)

$$z_{\min} \approx dx \tag{5.3}$$

The seismic data used for this study is part of the Spring Coulee vertical-component data that has been shown previously in this thesis. Prior to extracting the data for MASW processing, a number of tests were conducted to find the parameters that result in lowering the risk of higher mode contamination. Traces of each shot were divided into two groups, based on their position from the source, left and right. Then, two off-end shot gathers were extracted from each shot with the following parameters:

- Receiver spacing (*dx*) is 10 m ➔ $z_{\min} \approx 10$ m
- Receiver spread, *D*, is 300 m ➔ $z_{\max} \leq 150$ m
- Near-offset, x_1, is 150 m.

These off-end gathers were extracted for multiple shots at a shot interval of 30 m. Figure 5-2 shows a schematic representation of the geometry of a right off-end gather.

As mentioned earlier, a dynamite source of 2 kg buried at depth of 16 m, was used. The data extracted for MASM processing were the vertical-component acquired with 10 Hz multi-component geophones. The record length was reduced to 3 seconds, and the sample rate was kept at 2 ms. Based on those parameters, the shallowest depth of investigation is 10 m, and the maximum depth of investigation is 150 m.

From each shot, two off-end gathers were extracted: (1) 30 traces left to source with near-offset of 150 m, and (2) 30 traces right to the source with near-offset of 150 m. Figure 5-3 shows one shot gather with receivers being to the left side of the source. AGC (Automatic Gain Control) has been applied for display. Those parameters were tested to produce the best dispersion curves with lower risk of higher modes contamination. The SEG-Y file containing the data were then extracted, and formatted to KGS format in order to be readable in SurfSeis 2.0.

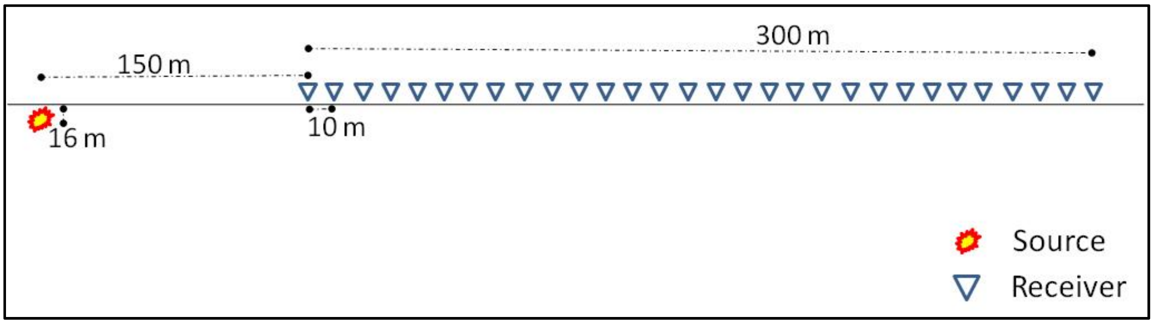

Figure 5-2. A schematic diagram of the geometry used of an off-end gather.

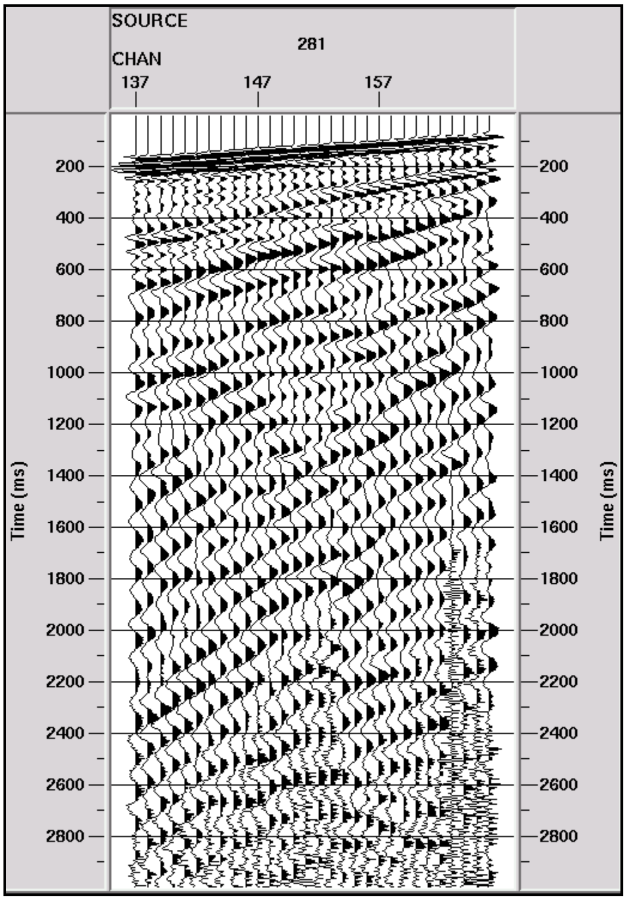

Figure 5-3. An off-end gather from Spring Coulee, to be MASW processed, with AGC applied for display.

The record lengths for the end-on gathers were reduced from 6 to 3 seconds because significant surface-wave data for the S-wave inversion are within the first 2 seconds. First P-wave arrivals are not wanted, and therefore were muted as is shown in Figure 5-4 (a). Most of the energy on that shot is due to surface waves and noise. Figure 5-4 shows the same shot gather with surface waves highlighted between two lines. The slopes of those lines correspond to velocities of 500 m/s and 1420 m/s.

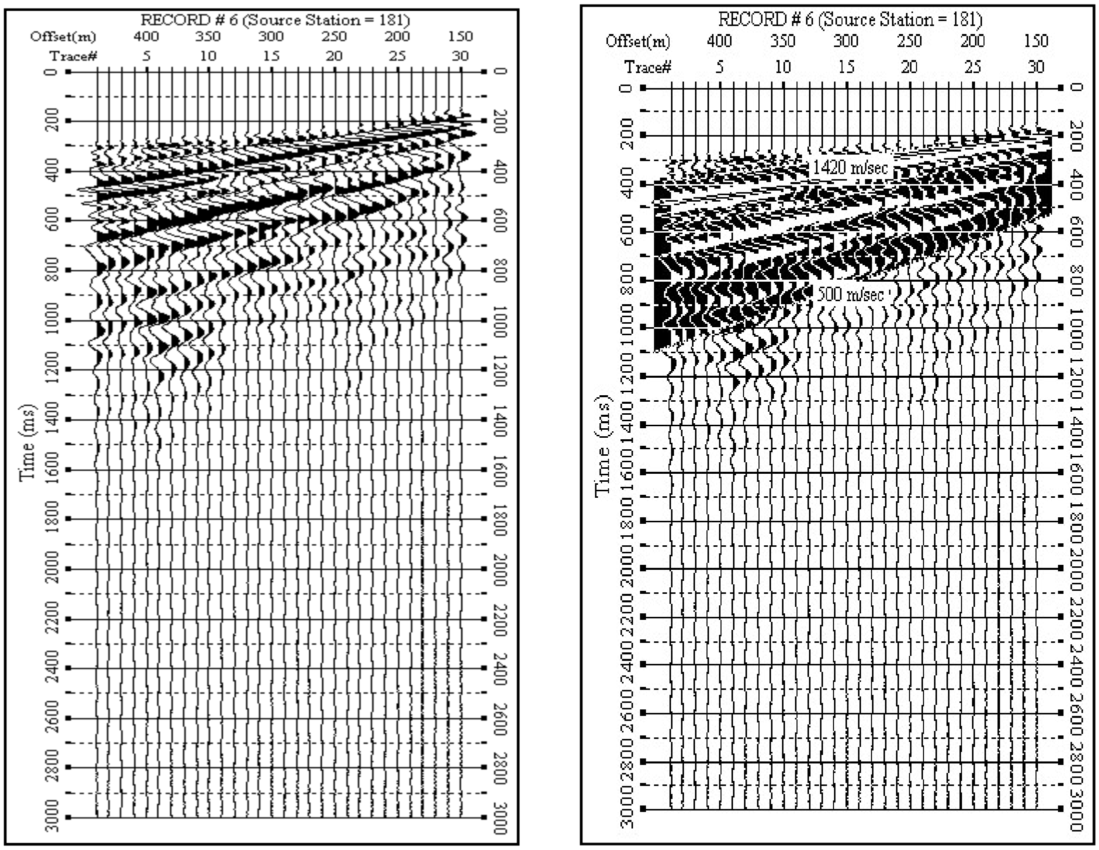

(a) **(b)**

Figure 5-4. Shot gather with first P-wave arrival muted (a), and with surface waves highlighted (b).

5.2.2 Dispersion analysis

Different modes of dispersive Rayleigh waves are separated by dispersion images. Dispersion images were calculated for all end-on vertical-component gathers using the method of Park et al. (1998)., which was described in Chapter 2. Dispersion images are then calculated for all off-end gathers. Figure 5-5 shows the dispersion image of the end-on gather shown on Figure 5-4; on such dispersion images, it is straightforward to discriminate between the fundamental mode and the 1st higher mode of the Rayleigh waves. The fundamental mode is indicated by the black dotted line, and the second mode is indicated by the pink dotted line.

From refraction analysis, the S-wave velocity of the first layer is estimated to be 420 m/s. The thickness of the first layer is about 12 m. Thereafter, substituting those values for V_s and h respectively, and 0 for n into Equation (2.10) will yield a cut-off frequency for the fundamental mode that is equal to 8.75 Hz, i.e., Raleigh waves with frequencies below 8.75 Hz will not propagate along the first layer.

The fundamental mode is the best mode to be used for inversion because this mode has more energy than the higher-order modes, and penetrates into the earth deeper than higher modes do. Therefore, the fundamental modes are picked for all dispersion images. Figure 5-6 shows the same dispersion image, as shown in Figure 5-5, but with the fundamental mode picked, and represented by the yellow dots. The fundamental mode of surface waves shows dispersive behaviour with higher phase velocities for the low frequencies. The phase velocities of the fundamental mode, as shown in Figure 5-5, range from 1100 m/s to 1550 m/s for a frequency range of 13 to 34 Hz.

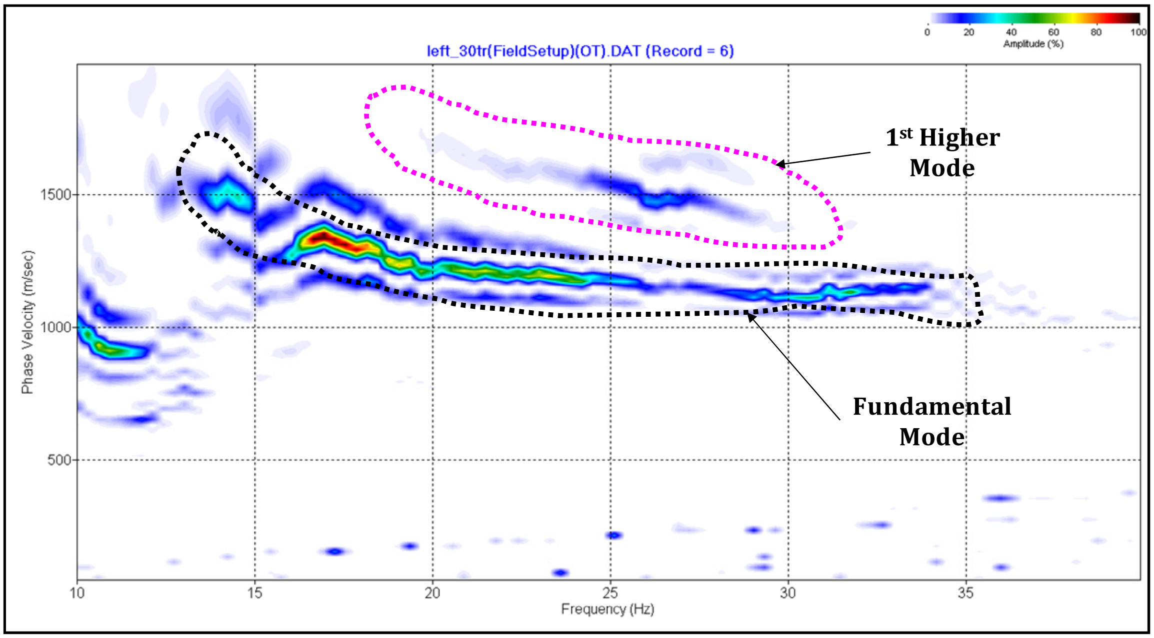

Figure 5-5. Dispersion image: fundamental mode highlighted in black, and 1st higher mode highlighted in pink.

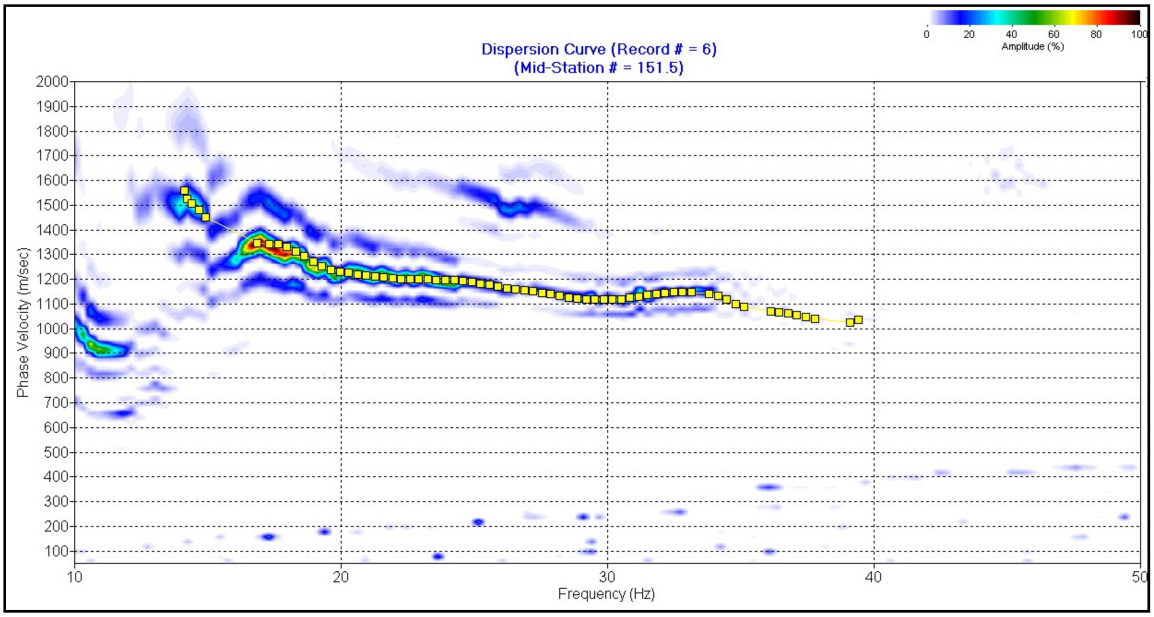

Figure 5-6. Dispersion image: fundamental mode picked and indicated by yellow squares.

5.2.3 Initial model and Inversion

The initial model is derived from the fundamental mode dispersion curve. The initial model, used here, is a 10-layer model. Another option would be an initial model that is based on P-wave data, and Poisson's ratio, similar to model (A) of Chapter One. However, I chose to use the 10-layer initial model derived from the dispersion curve for two reasons:

The first reason is that in the inversion process the velocities will be updated, with the thickness being fixed. In the previous chapter, we have seen that the velocity layering of the S-wave is independent of the velocity layering of the P-wave. Therefore, it is not wise to constrain thickness of S-wave layers to those of P-waves. For solving the statics problem and deep reflection imaging purposes, the trade-off between layer thickness and velocity makes velocity layering less serious. However, an accurate velocity value for the base of weathering would still be crucial.

The second reason is that in Chapter Two, we saw that the MASW inversion using the 10-layer S-wave initial model created from fundamental mode dispersion curve resulted in two distinct layers that accurately represented the earth model. Therefore, that is another encouraging point to favour this model over the 2-layer initial model based on P-wave velocity model.

For all dispersion images, the inversion was run allowing up to 6 updates to the S-wave velocities of the initial model. Figure 5-7 shows the initial S-wave velocity model, indicated by the dotted blue line, and the final S-wave velocity model, indicated by solid blue.

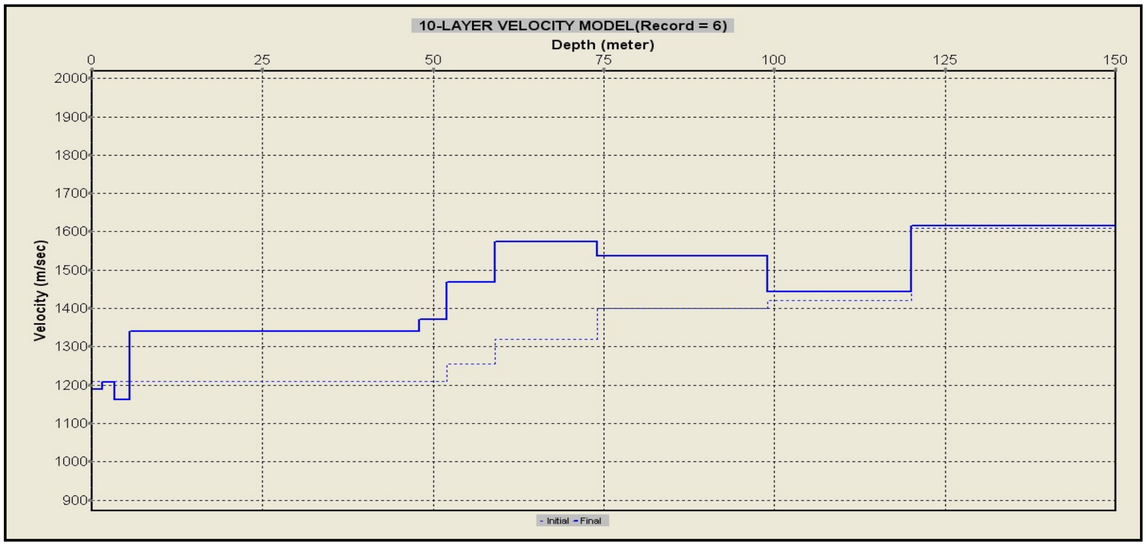

Figure 5-7. Initial model (dashed blue line) and inverted S-wave velocities (solid blue line).

5.3 Results

The S-wave velocity profile obtained by MASW processing is shown in Figure 5-8. For comparison, the S-wave velocity profile obtained by the refraction method (GLI3D) is shown in Figure 5-9. Note that the depth axis on the MASW 2-D S-wave velocity profile is referenced to the ground surface, while the elevation axis on the GLI3D velocity profile is referenced to sea level.

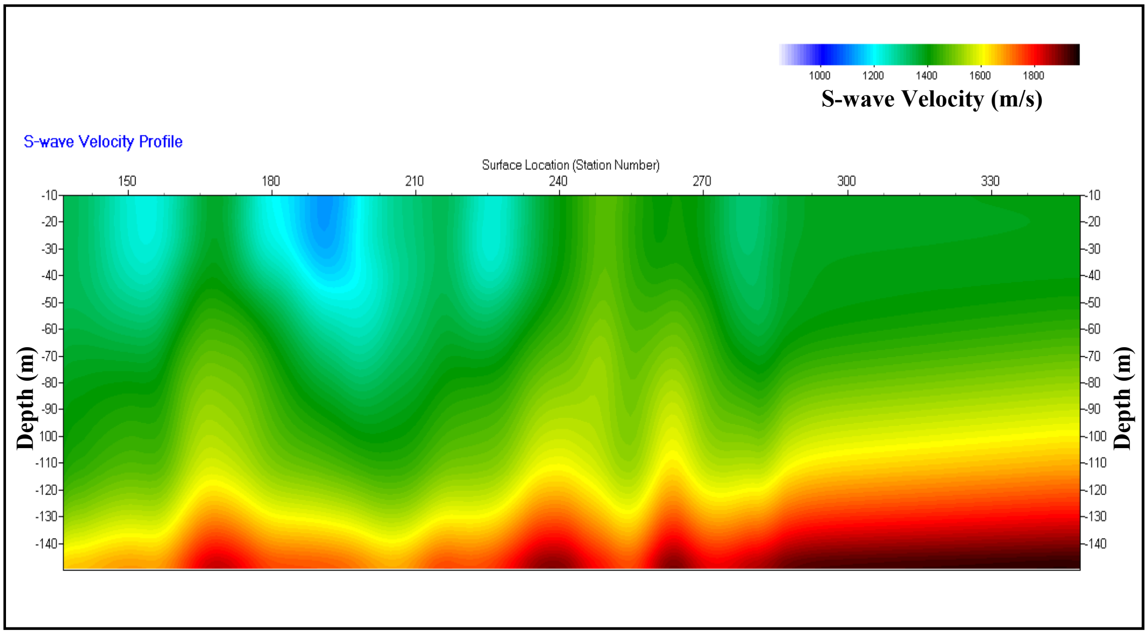

Figure 5-8. S-wave velocity profile obtained by MASW.

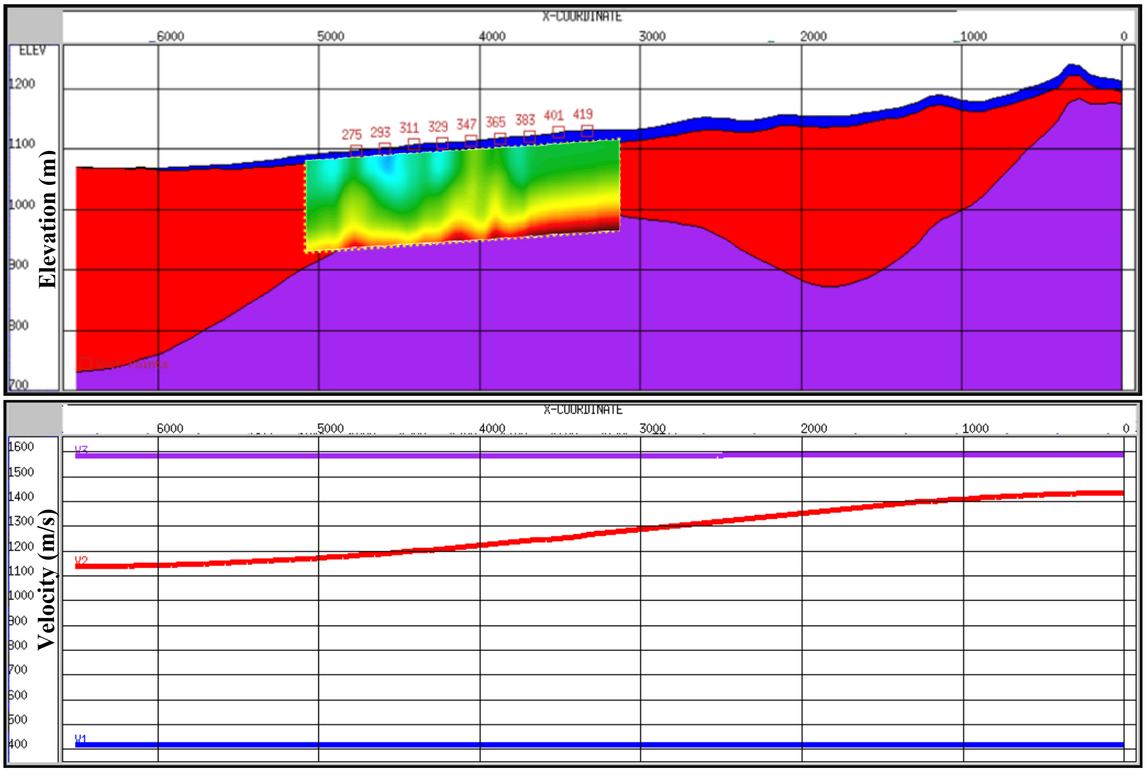

Figure 5-9. S-wave velocity profile obtained by the refraction method (GLI3D), with the section processed by MASW inserted inside the yellow box (upper), and S-wave velocity profile (lower).

A sensitivity test for the S-wave velocity profile to the initial model is presented in Appendix B. On the S-wave velocity profile obtained by MASW processing and shown on Figure 5-8, the red color indicates the S-wave velocity of the base of weathering and is about 1900 m/s. On the S-wave velocity profile obtained by the refraction analysis and shown in Figure 5-9, the base of the weathering is indicated by the purple color and has an S-wave velocity of about 1600 m/s. The second layer on Figure 5-9 (results of refraction methods) has an S-wave velocity ranging from 1180 m/s to 1280 m/s. For the velocity profile produced by MASW inversion and shown on Figure 5-7, this layer has an S-wave velocity ranging from 1400 m/s to 1600 m/s, as indicated by different grades of yellow and green colors. An important thing to keep in mind is that for any layer on Figure 5-9, there is a single velocity value and that corresponds to multiple velocity values on Figure 5-8. Even though the velocities that are obtained by MASW are higher than those that are obtained by the refraction method (GLI3D), both have a similar trend and show a strong correlation.

5.4 Discussion and conclusion

The MASW method requires a special configuration of seismic data that favours the fundamental mode of surface waves. Recording parameters of the Spring Coulee survey yielded subsets of data that were generally appropriate for the MASW method. However, a smaller receiver spacing (such as 5 m or 2.5 m) would have been more suitable.

The fundamental and the 1st higher mode of Rayleigh waves of Spring Coulee were separated easily in the dispersion images, enabling easy picking of fundamental modes. For the inversion of dispersion curves, I chose the 10-layer initial model estimated from the dispersion curve over the two-layer model based on refraction analysis of P-wave first arrivals. By this choice, I avoided constraining the thicknesses of S-wave velocity layers to the thicknesses of P-wave velocity layers (since I had already concluded that velocity layers of P waves and S waves were different).

The S-wave near-surface velocity model obtained by MASW processing has more velocity layers and higher velocity values than does the model obtained by refraction analysis of S-wave first arrivals. However, both models have the same trend and show fine correlation.

CHAPTER SIX: STATIC CORRECTIONS OF SPRING COULEE SEISMIC DATA

6.1 Introduction

The varying thicknesses and velocities of near surface (overburden and weathered) layers create serious problems for seismic reflection imaging of the deep subsurface. To improve the results of reflection imaging, static corrections are used to remove the effects of the variable, topographic near surface and replace them with a smooth or constant near surface. These corrections are constant time shifts, meaning the magnitude of the shifts do not vary with time, and they represent a coarse simplification of complex reality. Once a near-surface model is obtained, static correction process is one of the easiest processing steps. That does not play down its contribution and vital importance to our product, the seismic image (Margrave, 2005).

In this chapter, static corrections are calculated and applied to Spring Coulee data reflection dataset. P-wave statics are calculated using the refraction GLI near-surface model. Then, S-wave statics are calculated using two near-surface estimates from: (1) the GLI model, and (2) the MASW model. In chapter 4, the Common Conversion Point (CCP) for multi-component data was introduced. Here, I create and present CMP stack sections of P-wave (called PP stacked sections), and CCP stacked section of converted waves (called PS stacked sections).

6.2 Calculation of static corrections

Calculation of static corrections from a near-surface model is a simple and straightforward procedure. When calculating static corrections, it is often assumed that raypaths through the low velocity layer are close to vertical because this layer has a relatively low velocity. In some cases (relatively high near-surface velocities), the vertical raypath assumption would be a poor approximation.

A schematic representation of the Spring Coulee P-wave velocity near-surface model is shown in Figure 6-1. The P-wave velocities of the 1st and 2nd layers are α_1 and α_2 respectively. The thicknesses of the 1st and 2nd layers are h_1 and h_2 respectively. The difference between the datum elevation and the surface elevation is h_0, and the depth of the buried shot is h_s.

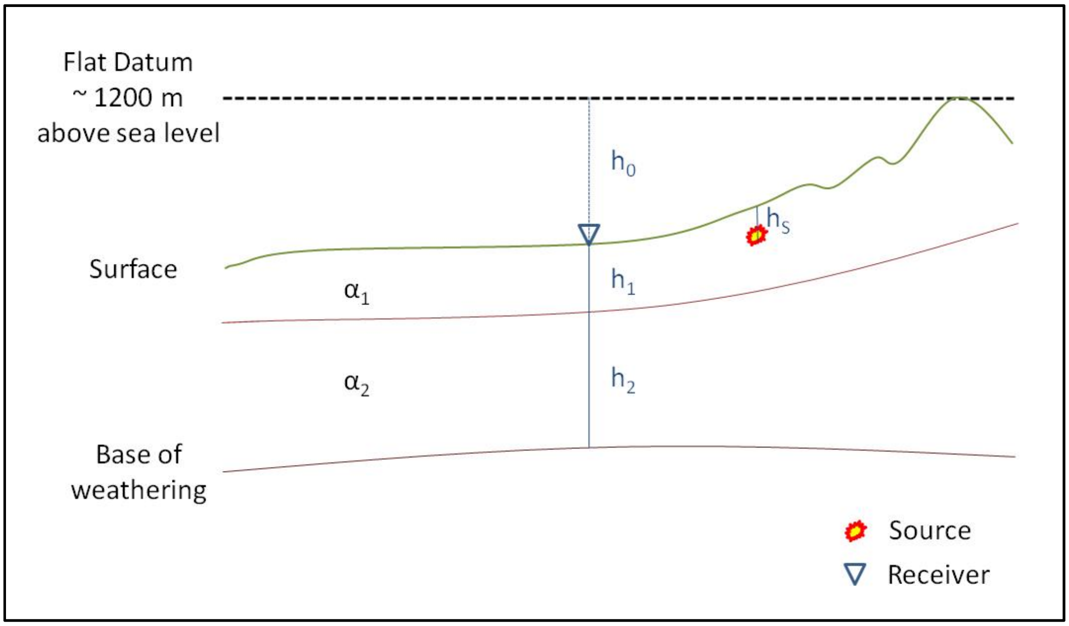

Figure 6-1. A schematic representation of Spring Coulee P-wave velocity near-surface model.

For each source and receiver location, two components of static corrections are calculated. The first component is the low-velocity layer (LVL) component, t_{LVL}. This component is required to bring the receiver or the shot down to the base of the weathering, and is always negative. The other component is the elevation correction, t_E, which is the time that a vertical ray would take to travel from the base of weathering up to the datum with the replacement velocity, V_{rep}. The replacement velocity is used to replace the varying near-surface velocity. The elevation correction is negative if the base of the weathering is below the datum, and is positive if the datum is below the base of the weathering. For the Spring Coulee model, shown in Figure 6-1, t_{LVL} is calculated as:

$$t_{LVL} = -\left(\frac{h_1}{\alpha_1} + \frac{h_2}{\alpha_2}\right). \tag{6.1}$$

And, the elevation static correction is calculated as:

$$t_E = \frac{h_0 + h_1 + h_2}{V_{rep}}. \tag{6.2}$$

Then, the datum static correction, t_{Datum}, is the sum of t_E and t_{LVL}

$$t_{Datum} = \frac{h_0 + h_1 + h_2}{V_{rep}} - \left(\frac{h_1}{\alpha_1} + \frac{h_2}{\alpha_2}\right). \tag{6.3}$$

For the buried shots of Spring Coulee, the depth of the shots should be accounted for by calculating the LVL correction of shots, $t_{LVL(shot)}$:

$$t_{LVL\,(shot)} = -\left(\frac{h_1 - h_s}{\alpha_1} + \frac{h_2}{\alpha_2}\right). \tag{6.4}$$

Refer to Appendix C for the spreadsheet used to calculate datum static corrections.

6.2.1 Converted wave statics

The calculation and removal of static corrections for multi-component seismic data is challenging and corrections for both S-waves and P waves must be calculated. An obvious solution, for calculating the S-wave corrections, would be multiplying the P-wave static correction by the P-wave to S-wave velocity ratio. However, this solution does not take into account the effect of a variable water table and other lateral inhomogeneities. Thus, it is not reliable.

To calculate S-wave static corrections using an S-wave near-surface model, the same concepts, used P-wave static corrections, are employed. S-wave near-surface models, compared to those of P-wave, often have lower velocities, different base of weathering, different velocity layering, the same datum, and the same surface elevation. The S-wave velocity is independent of pore space saturation because fluids have no resistance to shear, and the shear modulus, μ, in Equation (1.2), is therefore zero. Because the S-wave velocity in fluids is zero, the S-wave base of weathering might not be associated with the water table unlike the P-wave case (Cox, 1999).

For the multi-component survey at Spring Coulee, a dynamite source was used. The primary P-wave to S-wave conversion takes place at the geological boundaries deep below the surface. Therefore, in processing converted-wave data, P-wave static corrections must be applied for source locations, and S-wave static corrections must be applied for receiver locations.

6.2.2 Static corrections using GLI model

From the P-wave near-surface velocity model, shown in Figure 4-21, receiver datum static corrections were calculated using Equation (6.3). For the replacement velocity, V_{rep}, in this equation, a value of 3600 m/s was substituted. This is the largest value in the near-surface model and I have taken it to define the base of weathering. For the source static corrections, the depth of the shot was taken into account, as illustrated in equation (6.4). The reference datum is flat and its elevation is 1200 m above sea level, as shown in Figure 6-1. P-wave source and receiver static correction are used for the PP stacked section.

Then, from the S-wave near-surface velocity model, shown in Figure 4-22, the S-wave receiver datum static corrections were calculated using the same concept. An S-wave velocity value of 1600 m/s was substituted for the replacement velocity, V_{rep}. This value is the largest value in the S-wave near-surface velocity model and I consider it to define the base of weathering.

Figure 6-2 shows the P-wave receiver static corrections in green and S-wave receiver static corrections in blue. Static corrections for P-waves range from -25 ms to 27 ms, and those for S-waves range from -65 ms to 12 ms. Because S-wave velocities are significantly lower than those of P-waves, similar variations in thicknesses would produce larger variations in time for S-waves.

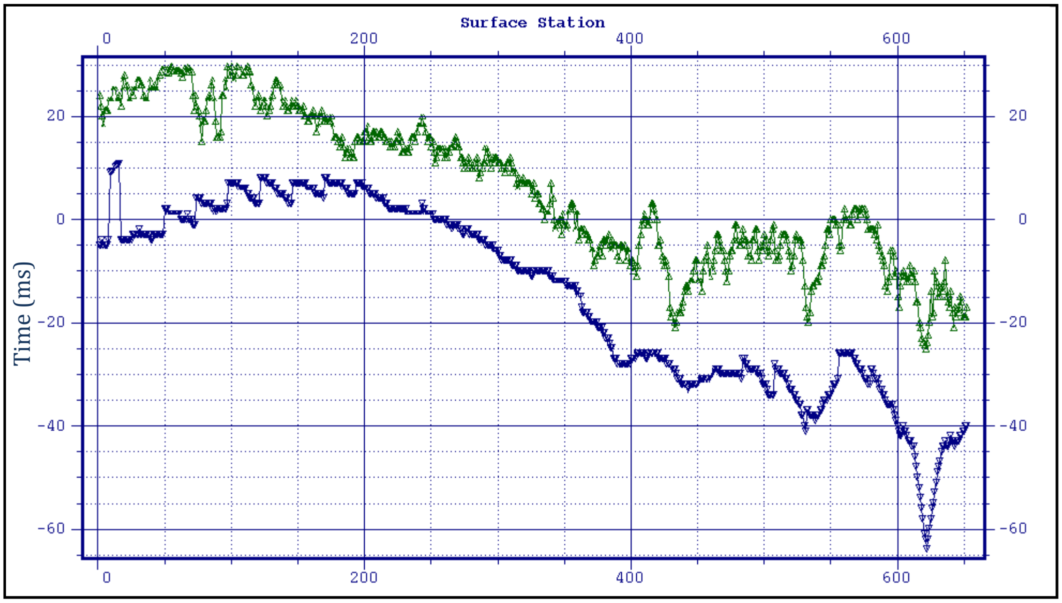

Figure 6-2. P-wave receiver statics in green and S-wave receiver statics in blue.

Though having different values, both P- and S-wave static corrections have similar trends. Changing the replacement velocity used for calculating S-wave static corrections from 1600 m/s to 1440 m/s will make P- and S-wave static corrections overlay with larger variations observed for the S-wave static corrections, as shown in Figure 6-3. Unlike S-wave static corrections of Figure 6-2, S-wave static corrections of Figure 6-3 are not accurate and will not be applied to the seismic data.

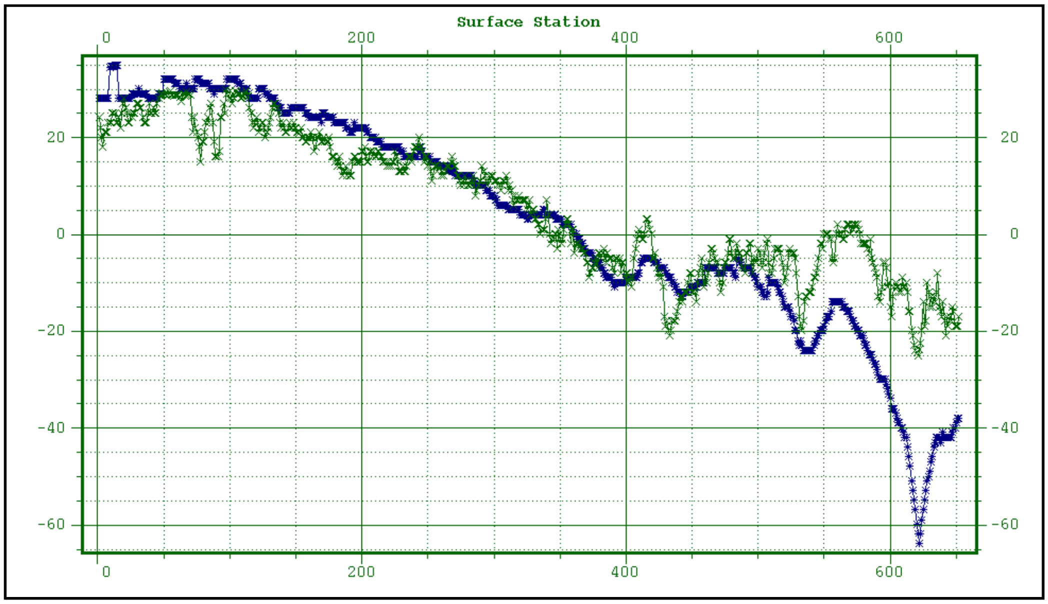

Figure 6-3. P-wave static corrections in green, and S-wave static corrections (with replacement velocity of 1440 m/s) in blue. S-wave static corrections, shown here, are not accurate and will not be applied to the seismic data.

Having calculated static corrections for P-wave and S-wave (shown in Figure 6-2), PP and PS stack sections with static corrections can be created by applying the following processing steps to vertical and radial component data:

1. Reversing polarity of traces that have negative offsets. This step is applied to radial-component data only.
2. P-S asymptotic binning with a P- to S-wave velocity ratio of 1.9. This step is applied to radial-component data only.
3. Applying total P-wave datum static corrections to source locations and receiver locations for the vertical-component data. For the radial data, the S-wave datum static corrections were applied to receiver locations, and P-wave static corrections were applied to source locations.

4. Air blast noise attenuation with the approximate velocity of energy to be attenuated being 331 m/s.
5. Surface wave noise attenuation with approximate velocity being 970 m/s.
6. Bandpass filter with corners at 10-14-60-80 Hz for vertical-component data, and at 4-10-20-30 Hz for radial-component data.
7. Spiking deconvolution.
8. Normal Moveout correction (NMO) with preliminary P-wave velocities for vertical-component data, and preliminary S-wave velocities for radial-component data. Then, post-NMO mute was applied.
9. Sorting vertical-component data by CDP, and radial-component data by CCP.
10. Stacking.

Using this processing flow, four sections were created: (1) PP stack without datum static corrections; (2) PP stack with datum static corrections; (3) PS stack without datum statics corrections; (4) PS stack with datum static corrections, and are shown Figure 6-4, Figure 6-5, Figure 6-6, and Figure 6-7 in respectively.

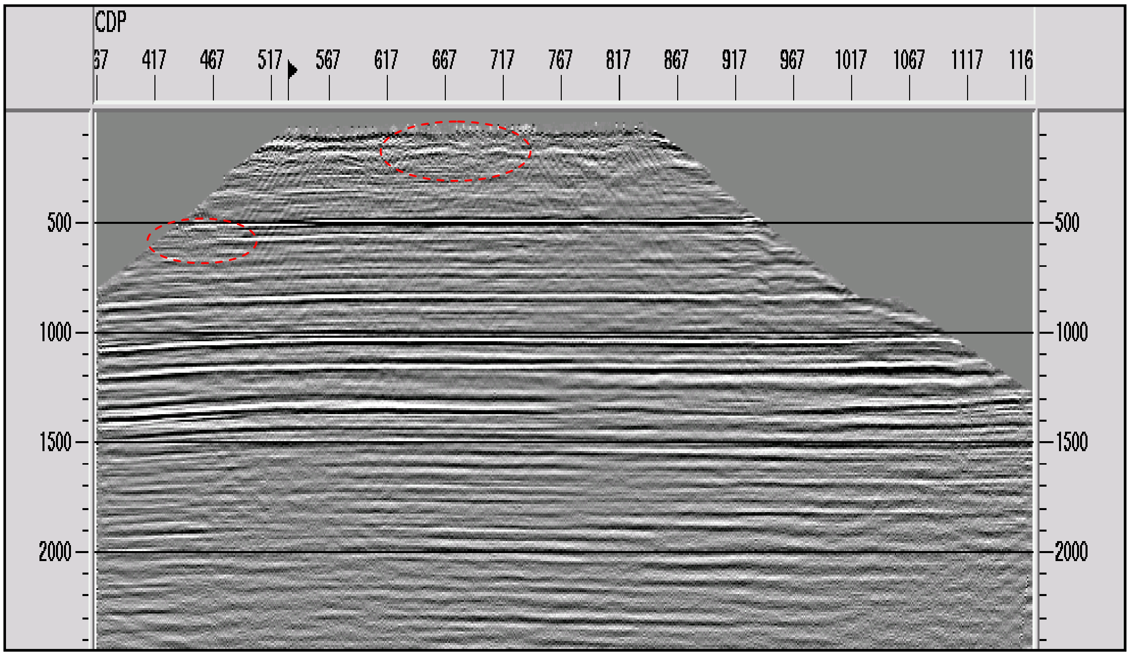

Figure 6-4. PP Stack with linear noise attenuation and spiking deconvolution applied.

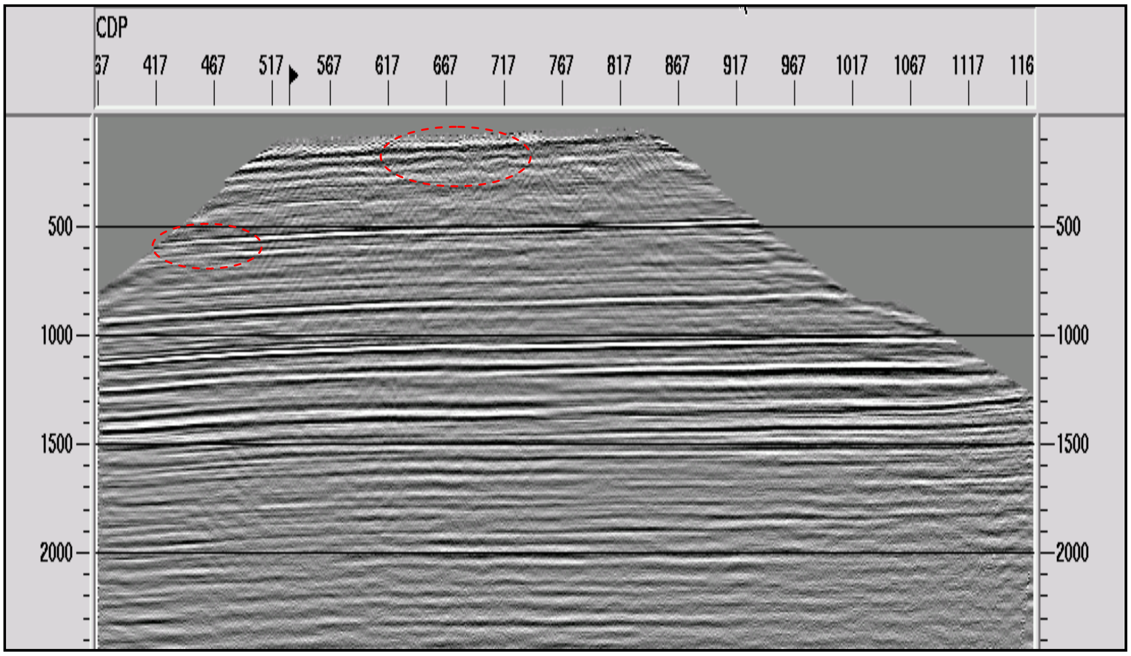

Figure 6-5. PP Stack with linear noise attenuation, spiking deconvolution, and refraction statics applied.

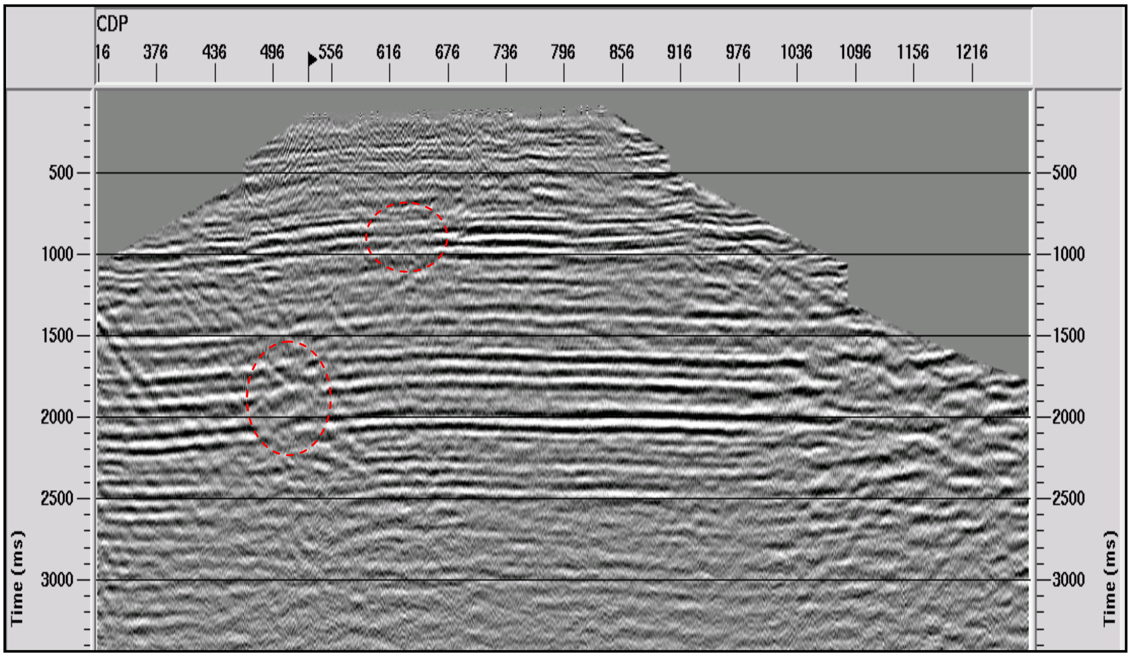

Figure 6-6. PS Stack with linear noise attenuation, and spiking deconvolution applied.

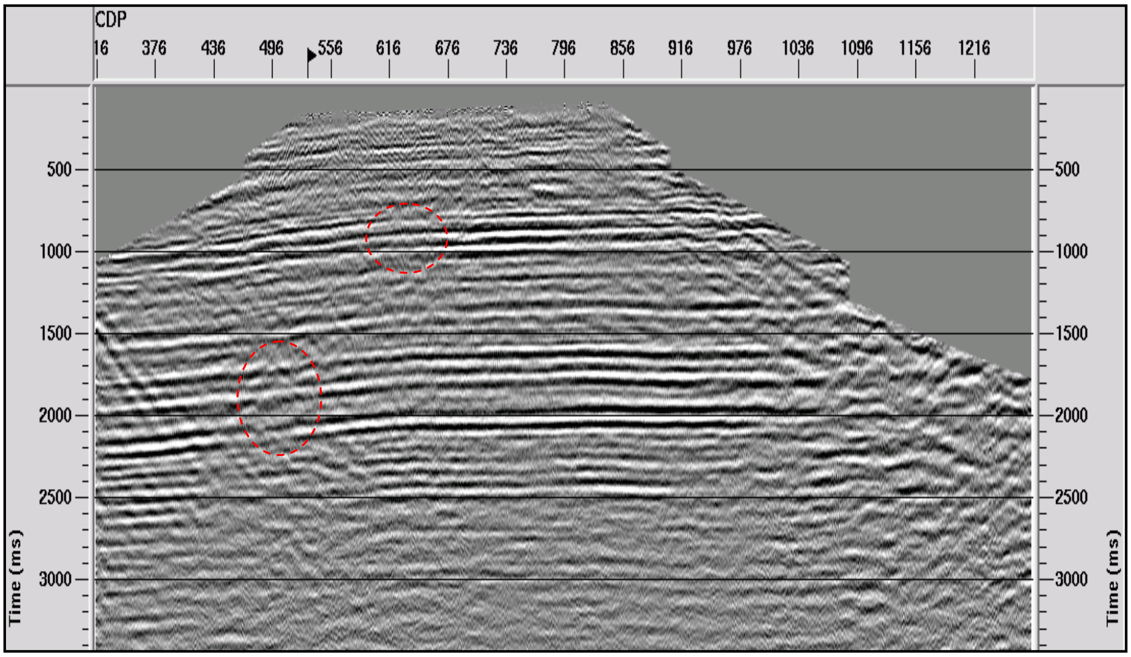

Figure 6-7. PS Stack with linear noise attenuation, spiking deconvolution, and refraction statics applied.

By comparing the PP stack sections before and after the application of the datum static corrections, the effect of static corrections is clear especially in the shallow events (~200 ms) where reflection events are stacked better. A similar conclusion can be drawn about the PS stack sections. Also, the stacking of the deeper reflection event around 800 ms is significantly improved. This event can be found around 1400 ms in the PS section, and application of static corrections also improved stacking in PS section. As well, shallow events were improved as a result of applying static corrections to PS section. Some areas where the application of static corrections improved the stacking of reflection events are indicated by dashed red circles on the PP and PS sections.

All reflection events on the PP section can be related to the PS section, as shown in Figure 6-9. This figure was obtained by stretching of the time axis of the PP section, so corresponding reflection events are matched on both PP and PS stack sections, as shown in Figure 6-8.

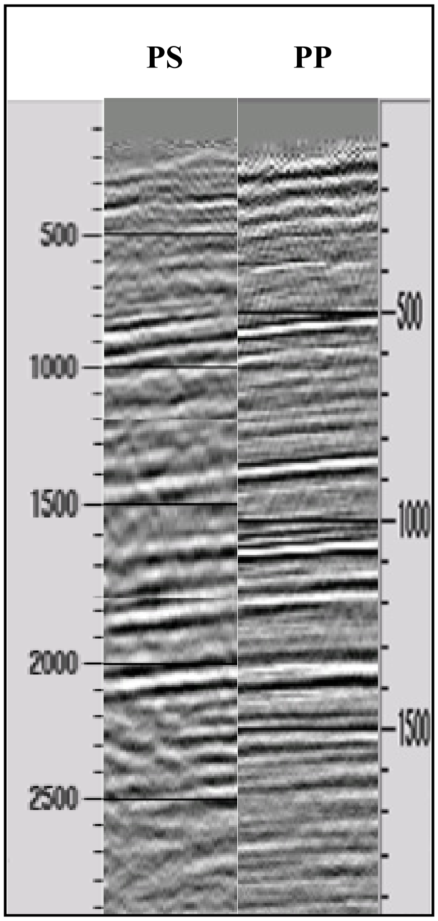

Figure 6-8. Correlating reflection events of PS (left) and PP (right) sections. Time axes are in milliseconds.

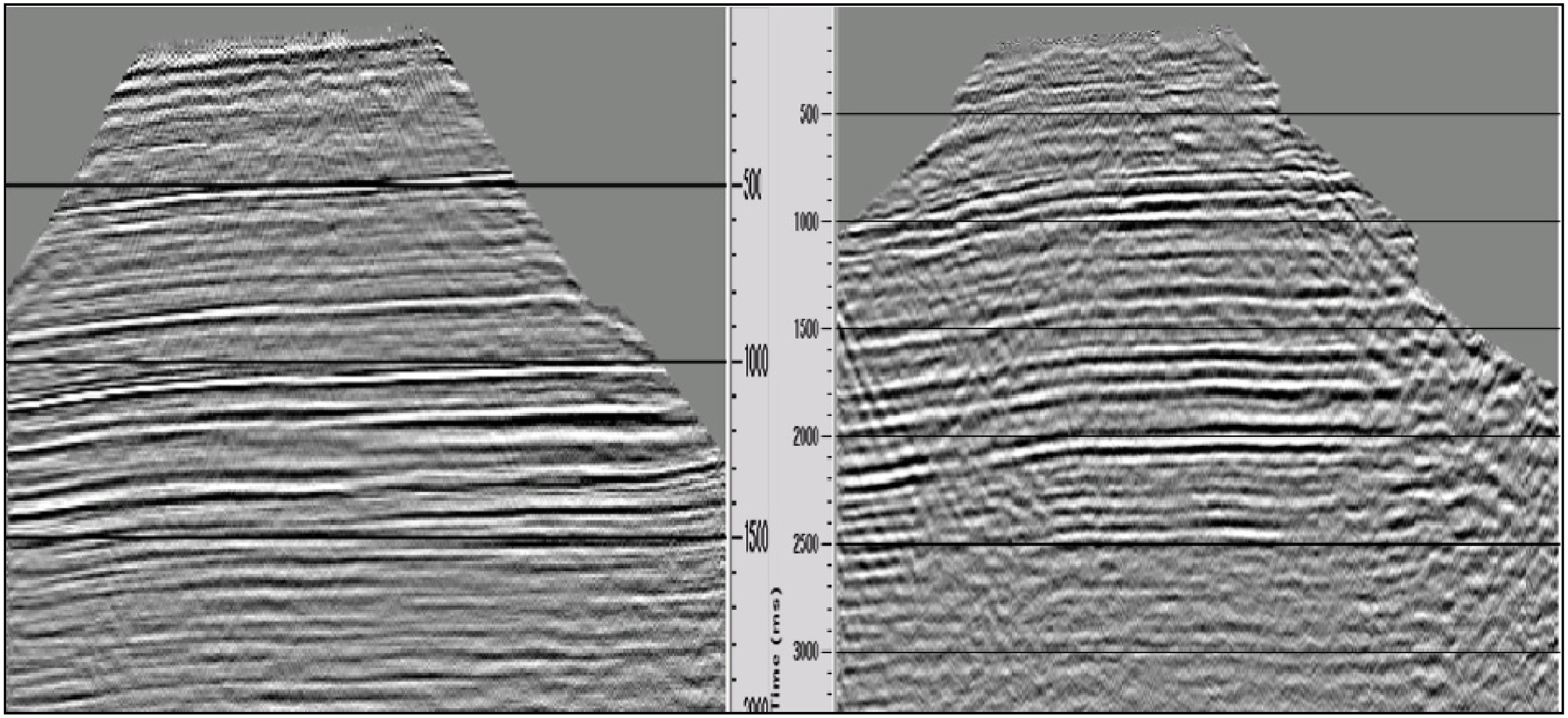

Figure 6-9: PP (left) and PS (right) stack sections with refraction statics applied. Time axes are in milliseconds.

6.3 Static corrections using MASW model

The S-wave near-surface velocity model, shown in Figure 5-8, is used to calculate receiver datum static corrections. Datum static corrections were calculated for receiver locations using Equations (6.1)-(6.3) in a Microsoft Excel worksheet, and shown in Appendix C. I have used the highest velocity of the model (~1966 m/s) for the replacement velocity. Also, as for the GLI model, I have used 420 m/s for the velocity of the shallowest layer. The total receiver datum static corrections calculated using the MASW model is shown in green on Figure 6-10. For comparison, the total receiver datum statics correction calculated using the GLI model is shown in blue on the same figure. Both have similar trend, but those of the GLI model have less variations. No short wavelength static corrections are included.

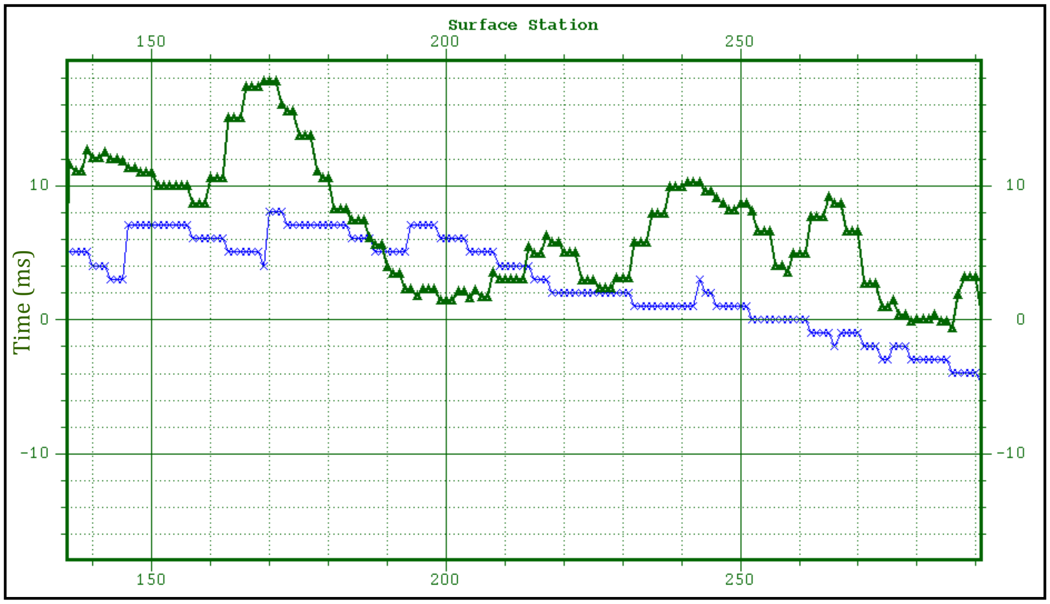

Figure 6-10. S-wave receiver statics calculated from: MASW near-surface model in green, and GLI near-surface model in blue.

S-wave datum static corrections calculated using the S-wave MASW model were applied to receiver locations, and P-wave static corrections calculated using the P-wave GLI refraction model were applied to source locations. To create the PS stack section, the same processing flow explained earlier was used. However, to observe the effect of S-wave MASW static corrections only, a significant number of traces were thrown away and only those for which static corrections were calculated using the MASW model were used. A second stack section was created for comparison, but with the application of static corrections calculated using the S-wave GLI refraction model. Moreover, there are no short wavelength static corrections in both sections.

The PS stack section created with statics from the S-wave MASW model is shown on the upper part of Figure 6-11. The PS stack section created with statics from the S-wave GLI refraction model is shown on the lower part of the Figure 6-9. Comparing both sections, I consider that the stack quality using S-wave static corrections calculated from the MASW model is very comparable to the stack quality using S-wave statics calculated from the GLI refraction model. The same data, but without static corrections, is shown in Figure 6-12. Applying static corrections improves the stacking of reflection events significantly.

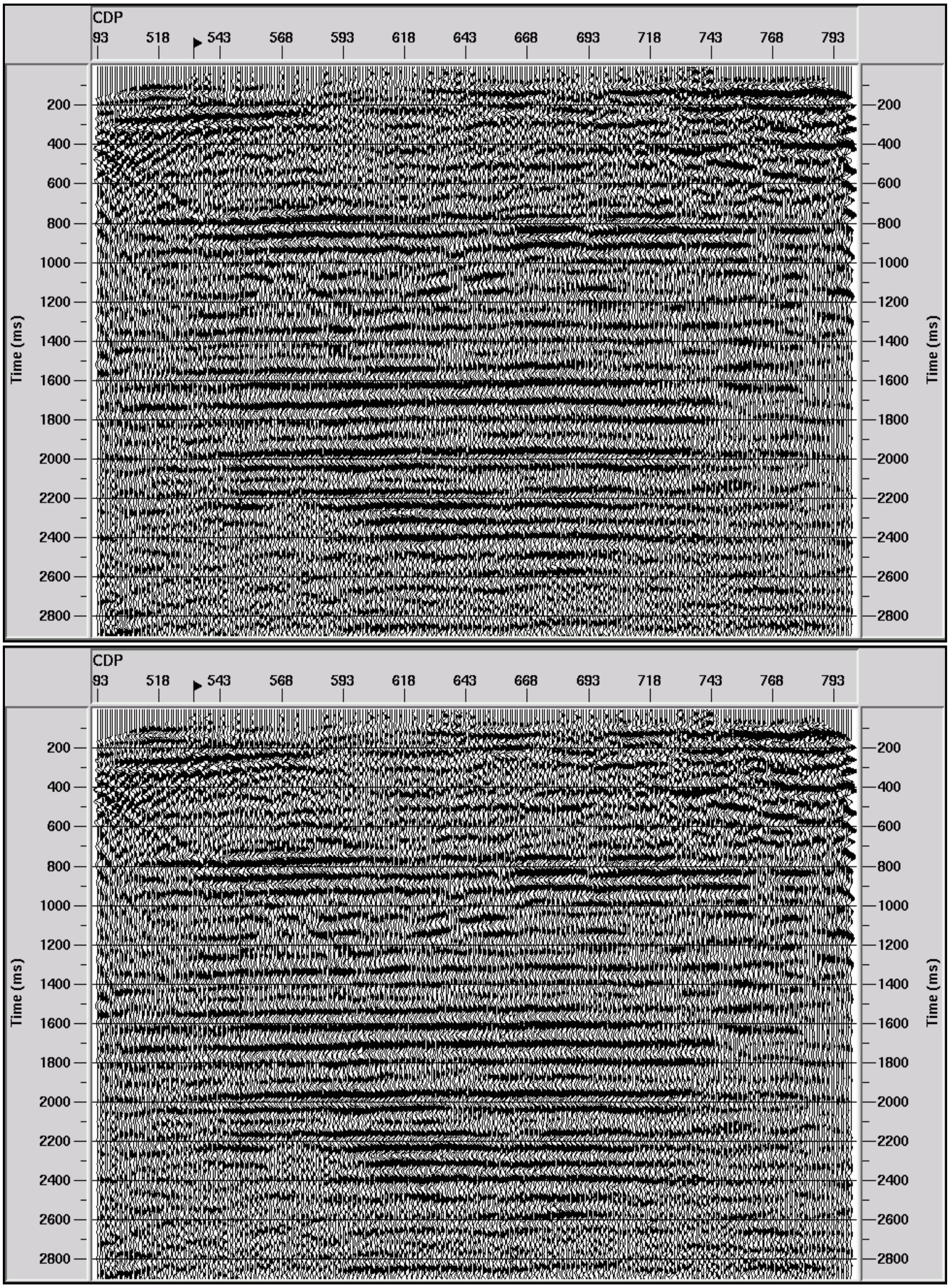

Figure 6-11. PS stack after applying static corrections calculated from: MASW (upper) and GLI (lower) models.

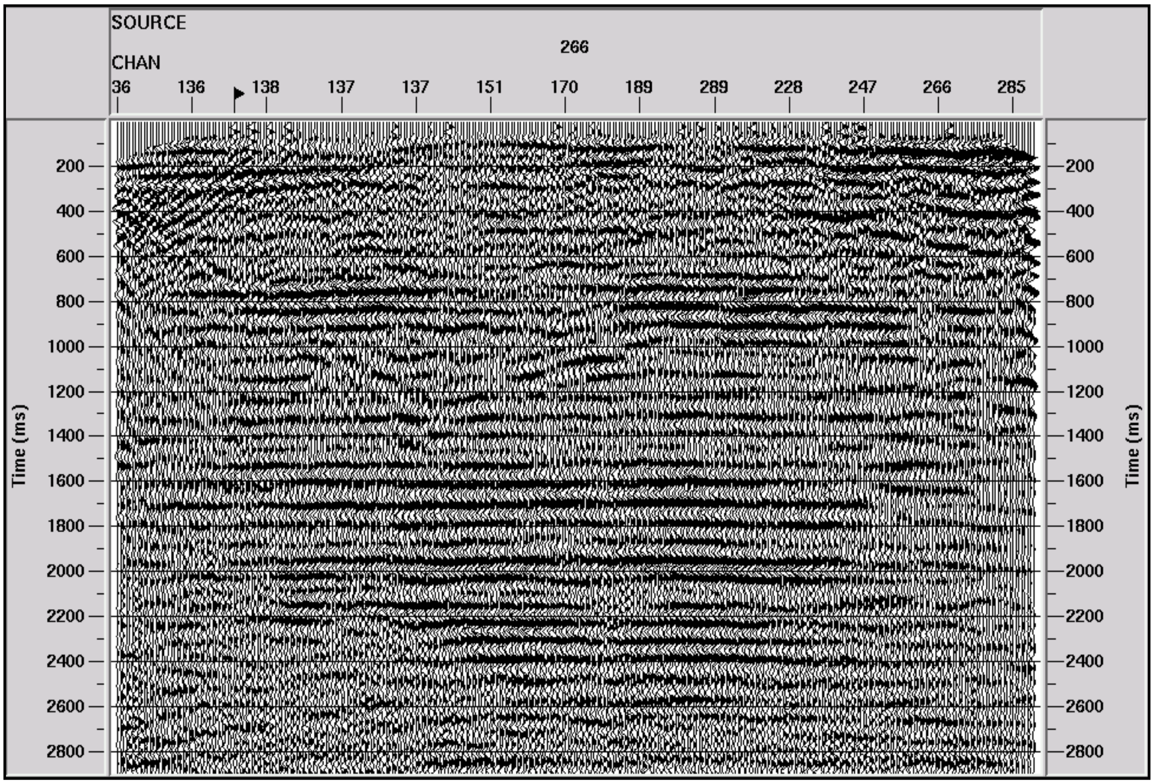

Figure 6-12. PS stack (data shown in Figure 6-11) without static corrections.

Three sections from Figure 6-11 and Figure 6-12 are shown side-by-side in Figure 6-13 to compare PS stacked data without static correction applied, with static corrections correction calculated from the MASW model applied, and with static corrections calculated from the GLI model applied. Some areas with obvious differences between the three sections are indicated by the red rectangles.

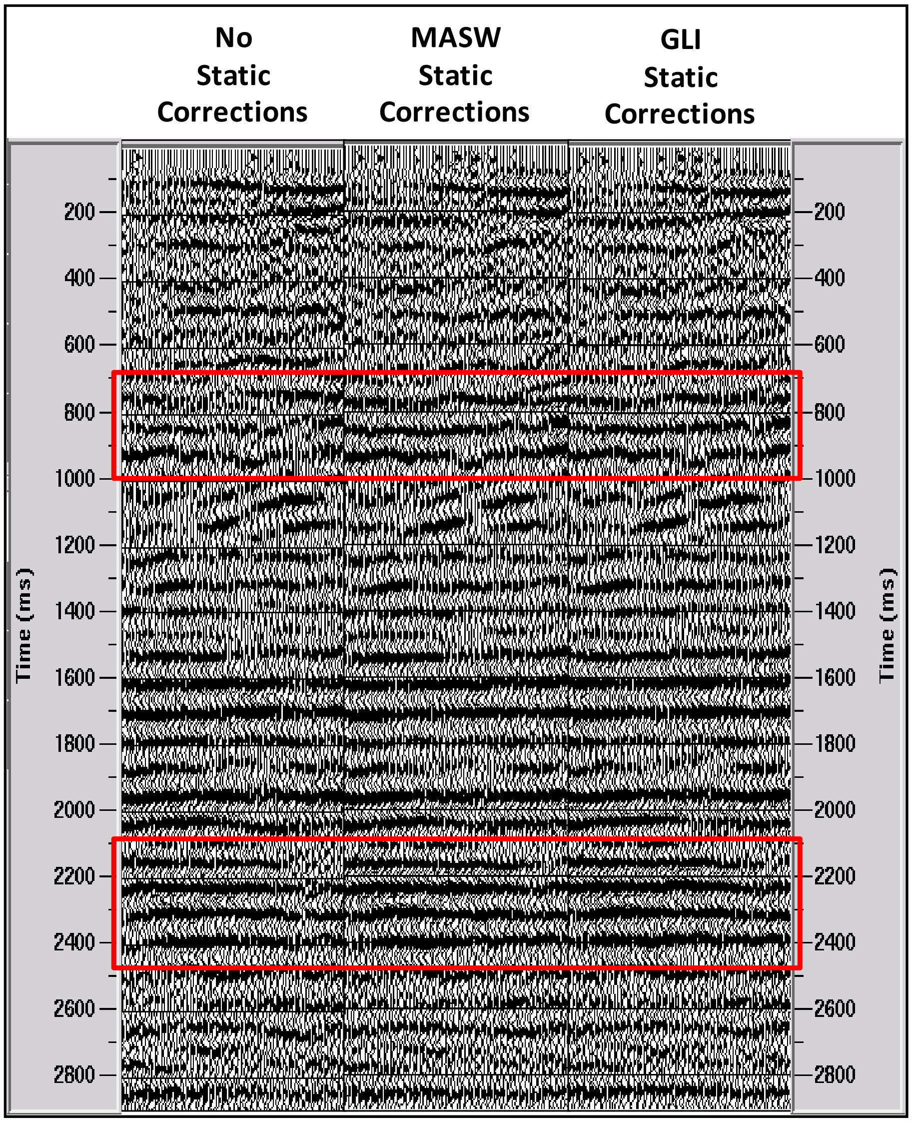

Figure 6-13. Side-by-side comparison of PS stacks: without static corrections (left), with static corrections of MASW model applied (middle), and with static corrections of GLI model applied (right). Some areas with obvious difference between the three sections are indicated by the red rectangles.

6.4 Discussion and conclusion

Unlike solving for near-surface velocity models, calculating static corrections is a simple procedure. Static corrections, although simple to calculate, are crucially important to creating reflection seismic images. Reflection events stack better after applying static corrections.

In multi-component surveys, calculating static corrections is one of the most challenging processing steps. In forming PS stack sections from multi-component surveys, static corrections require near-surface velocity models for both P-waves and S-waves. Because the conversion to S-wave happens at some geological boundaries below the surface, P-wave static corrections must be applied to source locations, and S-wave static corrections must be applied to receiver locations.

For the Spring Coulee survey, static corrections for the converted waves were calculated for two different near-surface S-wave velocity models: the GLI refraction model, and the MASW model. GLI refraction models are common and widely used for calculating both P and S static corrections. On the other hand, the MASW method for obtaining near-surface S-wave velocity models is mostly used for geotechnical purposes. I have used it successfully in this chapter to get near-surface S velocity models from Raleigh wave data to calculate receiver statics for converted wave reflections. The quality of the PS section obtained by applying S-wave MASW model static corrections is at least as good as the quality of that obtained by applying S-wave GLI refraction model statics.

CHAPTER SEVEN: CONCLUSIONS

Variations in the thicknesses and comparatively low velocities of the near-surface overburden and weathered layers significantly degrade the seismic reflection sections. Therefore, static corrections must be calculated from near-surface velocity models to correct for the near-surface effect. Although simple to calculate, these corrections are essential because they improve the signal-to-noise ratio of reflection seismic data and remove time structure effects on seismic time sections. After applying static corrections, reflection events from intersecting 2D lines or overlapping 3D survey blocks tie better because all data are corrected to the same datum. Also, the application of static corrections improves other processing steps, such as velocity analysis.

To obtain accurate static corrections, acquisition and processing must invest in the near-surface model. In this thesis, two methods for characterizing near-surface layers were utilized. The first method is GLI refraction analysis of first arrival times, a widely used and well-proven method for obtaining near-surface velocity models for both P- and S-waves. The second is the MASW method. The MASW method is based on the dispersion properties of Rayleigh waves, and mainly used for geotechnical engineering purposes. In this thesis, I applied the MASW method to obtain near-surface S-wave velocity models of Spring Coulee, and used this model to calculate S-wave static corrections.

Finite-difference modeling techniques are useful tools that geophysicists use for testing their earth models, and the methods by which they obtain their earth models. Elastic finite-difference methods were used to numerically model synthetic seismic traces through an earth model. Then, the inverse problem of finding the earth model from the synthetic data was solved by the inversion of Rayleigh-wave dispersion-curves for S-wave velocities, and refraction analysis for P-wave velocities. The inversion of the synthetic Rayleigh-wave dispersion curves using two different initial S-wave velocity models was done to test the effect of the starting model on the final model. The outcome of the test indicated that the final result did not depend greatly on the initial model as long as the initial model was geologically realistic.

Beside the synthetic data, the MASW method was applied to two datasets. The first dataset comprises 2D shallow refraction seismic data acquired by the 2007 University of Calgary Geophysics Field School on the Rothney Astrophysical Observatory property near Priddis, Alberta. The lithology of the near-surface geology on this site was described using drill cuttings from an offset well (about 2.5 m away from the 2D seismic line). The other dataset is 2D multi-component reflection seismic data acquired in Spring Coulee by CREWES for hydrocarbon exploration. The objective was to compare the near-surface S-wave velocity model obtained by this method to the model obtained by the Generalized Linear Inverse method (of first-arrival times), and to use these models later for static correction. The GLI method was applied to P-wave first arrivals from the vertical component data, and to S-wave first arrivals from the radial component data. The resulting P- and S-wave velocity models at the Spring Coulee site had different velocity layering and base of weathering.

Three near-surface velocity models (GLI refraction P-wave model, GLI refraction S-wave model, and MASW S-wave model) were used to calculate three sets of static corrections. Those static corrections were applied to create PP and PS stack sections.

For converted wave PS sections, the effectiveness in improving the quality of reflection events by applying S-wave statics from the MASW model is similar to the effectiveness of using S-wave statics from the GLI refraction model. Identifying and picking S-wave first arrivals is difficult and time consuming. Unfortunately, automatic picking programs do not work well for S-wave refractions. Confusing S-waves with Rayleigh waves is also a problem. The MASW method is a potential alternative to the GLI of first arrival times method for modeling S-wave velocities of the near surface.

REFERENCES

Al-Eqabi G. I., and Herrmann R. B., 1993, Ground Roll: A potential tool for constraining shallow shear wave structure: Geophysics, **58**, 713-719.

Al-Husseini, M. I., J. B. Glover, and Barley, B. J., 1981, Dispersion patterns of the ground roll in eastern Saudi Arabia: Geophysics, **46**, 121-137.

Anderson, N., Chen, G., Kociu, S., Luna, R., Thitimakorn, T., Malovichko, A., Malovichko, D., and Shylakov, D., 2003, Vertical Shear-wave Velocity Profiles Generated From Spectral Analysis of Surface Waves: Field Examples: Missouri Department of Transportation, Development and Technology report, RDT 03-006.

Brown, G. C. and Mussett, A. E., 1981, The inaccessible earth, George Allen and Unwin, London, UK.

Bullen, K. E., 1963, An introduction to the theory of seismology, Cambridge University Press.

Castagna, J.P., Batzle, M.L., and Kan, T.K., 1993. Rock physics –The link between rock properties and AVO response, in Offset-Dependent Reflectivity – Theory and Practice of AVO Analysis, J.P. Castagna and M. Backus, eds. Investigations in Geophysics, No. 8, Society of Exploration Geophysicists, Tulsa, Oklahoma, 135-171.

Cox, M., 1999, Static Corrections for Seismic Reflection Surveys: SEG, Tulsa, OK.

Dobrin, M. B., 1951, Dispersion in seismic surface waves: Geophysics, **16**, 63-80.

Dorman, J., and Ewing, M., 1962, Numerical inversion of seismic surface wave dispersion data and crust-mantle structure in the New York–Pennsylvania area: J. Geophys. Res., **67**, 5227–5241.

Dorman, J., Ewing, W. M., and Olivier J., 1960, Study of the shear-velocity distribution in the upper mantle by mantle Rayleigh waves: Bulletin of the Seismological Society of America, **50**, 87-115.

Ewing, W. M., and Jardetzky, W. S., Press, F., 1957, Elastic waves in layered media, McGraw Hill Book Co. Inc., New York.

Farrell, R. C., and Euwema, R. N., 1984, Refraction statics: Proceedings of the IEEE, **72**, 1316-1329.

Grant, F. S., and West, G. F., 1965, Interpretation theory in applied geophysics: New York, McGraw-Hill Book Co., Inc.

Grasby, S.E., 2006, Paskapoo Formation – Alberta's most heavily used aquifer: The Fossil Water report, **4**, 1-3.

Geological Survey Division, 1951, Geological Map of Alberta: Geological Survey of Canada, Map 1002A, Scale 1:1,267,200.

Hampson, D., and Russell, B., 1984, First-break interpretation using generalized linear inversion: J. Can. Soc. Expl. Geophys., 20, 40–54.

Hampson-Russell Software Services Ltd., 2004, GLI3D theory.

Haskell, N. A., 1953, The dispersion of surface waves on multilayered media: Bull. Seis Soc. Am*.,* **43**,17-34.

Keilis-Borok, V. I., 1989, Seismic Surface Waves in a Laterally Inhomogeneous Earth, Kluwer Academic Publishers, Dordrecht, 293-304.

Krebes, E., 1989, Seismic Theory and Methods: Geophysics 551 course notes, University of Calgary, 4.1-4.18.

Knopoff, L., 1972, Observation and inversion of surface wave dispersion: Tectonophysics, **13**, 497-519

Kovach, R. L., 1978, Seismic surface waves and crust and upper-mantle structure: Rev. Geophys and Space Phys., **16**, 1-13.

Lin, Y., 2007, Characterizing V_S Profiles by the SASW Method and Comparison with Other Seismic Methods: Ph.D. thesis, University of Texas at Austin.

Manning, P. M., 2007, Techniques to enhance the accuracy and efficiency of finite-difference modelling for the propagation of elastic waves: Ph.D. thesis, University of Calgary.

Margrave, G. F., 2000, New seismic modeling facilities in Matlab: CREWES Research Report, **12**.

Margrave, G. F., 2005, Methods of seismic data processing: Geophysics 557 course notes, University of Calgary.

McMechan, G. A., and Yedlin, M. J., 1981, Analysis of dispersive waves by wave field transformation: Geophysics, **46**, 869–874.

Miller, G. F., and Pursey, H., 1955, On the partition of energy between elastic waves in a semi-infinite solid: Proc. R. Soc., **A233**, 55-69.

Mokhtar, T. A., Herrmann, R. B., and Russell, R. D., 1988, Seismic velocity and Q model for the shallow structure of the Arabian shield from short-period Rayleigh waves: Geophysics: **54**, 1379-1387.

Park, C. B., 2006, SurfSeis 2.0 User's Manual: Kansas Geological Survey.

Park, C. B., Millar, R. D., and Xia, J., 1998, Imaging dispersion curves of surface waves, Presented at the 68th Ann. Mtg of SEG, New Orleans, Expanded Abstract, 1377-1380.

Park, C. B., Millar, R. D., and Xia, J., 1999, Multichannel analysis of surface waves: Geophysics: **64**, 800-808.

Pelton, J. R., 2005, Near-Surface Seismology—Surface-Based Methods: Soc. Explor. Geophys., Investigations in Geophysics No. 13, Dwain K. Butler, ed., Near-surface Geophysics, 242-247.

Rayleigh, L., 1887, On waves propagated along the plane surface of an elastic solid: Proc. R. Soc. London, **17**, 4-11.

Richart, F. E., Hall, J. R., and Woods, R. D., 1970, Vibrations of soils and foundations: Prentice-Hall, Inc.

Russell, B. H., 1993, Static Corrections: International Human Resource Development Cooperation.

Sheriff, R. E., 1991, Encyclopedic dictionary of exploration geophysics: Society of Exploration Geophysicists.

Sheriff, R. E., and Geldart, L. P., 1982, Exploration seismology, History, theory and data acquisition, Vol. 1: Cambridge University Press.

Sheriff, R. E., and Geldart, L. P., 1995, Exploration Seismology, 2nded.: Cambridge University Press.

Strobbia, C., 2003, Surface wave methods acquisition, processing and inversion: PhD Thesis, Politecnico di Torino, Turin, Italy.

Stokoe II, K. H., Wright, G. W., Bay, J. A., and Roesset, J. M., 1994, Characterization of geotechnical sites by SASW method, in Woods, R. D., Editor, Geophysical characterization of sites: Oxford Publishers.

Sezawa K., 1927, Dispersion of elastic waves propagated on the surface of stratified bodies and on curved surfaces. Bull. of the Earthquake-Inst: Imperial Univ. Tokyo, **3**, 1-18.

Thomson, W. T., 1950, Transmission of elastic waves through a stratified solid medium: J. Appl. Phys., 21,89-93.

Xia, J., Miller, R. D., and Park, C. B., 1999, Estimation of near-surface shear-wave velocity by inversion of Rayleigh wave: Geophysics, **64**, 691– 700.

Xu, C. Q., 2004, Multi-channel techniques for near-surface cavity imaging using Rayleigh waves: M.Sc. Thesis, Dalhousie University.

Yordkayhun, S., Juhlin, C., Giese, R., and Cosma, C., 2007, Shallow velocity–depth model using first arrival traveltime inversion at the CO2SINK site, Ketzin, Germany: Journal of Applied Geophysics, **63**, 68-79.

Williams, E. P., 1951, St. Mary River formation in Spring Conlee-Magrath area, Alberta, Canada: Am. Assoc. Petroleum Geologists Bull., v. 35, p. 888-898.

APPENDIX A: FINITE-DIFFERENCE MODELING

The acoustic finite-difference method uses the second-order finite-difference approximation for the wavefield second time derivative in the acoustic wave equation. The variable velocity scalar wave equation in two dimensions, (x,z), is

$$\nabla^2\psi(x,z,t)=\frac{1}{v^2(x,z)}\frac{\partial^2\psi(x,z,t)}{\partial t^2}, \tag{A.1}$$

where the 2-dimensional Laplacian is

$$\nabla^2\psi=\frac{\partial^2\psi}{\partial x^2}+\frac{\partial^2\psi}{\partial z^2}. \tag{A.2}$$

The second time derivative of the wavefield $\psi(x,z,t)$ in Equation (A.1) can be approximated using the second-order finite-difference approximation,

$$\frac{\partial^2\psi}{\partial t^2}\approx\frac{\psi(t+\Delta t)-2\psi(t)+\psi(t-\Delta t)}{\Delta t^2}, \tag{A.3}$$

where Δt is the time interval. Equation (A.3) can be substituted into Equation (A.1), and the scalar wave equation is rewritten as

$$\nabla^2\psi(x,z,t)=\frac{1}{\Delta t^2 v^2(x,z)}[\psi(x,z,t+\Delta t)-2\psi(x,z,t)+\psi(x,zt-\Delta t)]. \tag{A.4}$$

Equation (4) is solved for $\psi(x,z,t+\Delta t)$,

$$\psi(x,z,t+\Delta t)=\left[2+\Delta t^2 v^2(x,z)\nabla^2\right]\psi(x,z,t)-\psi(t-\Delta t). \tag{A.5}$$

The wavefield at $t+\Delta t$ can be approximated, using Equation (A.5), if earlier wavefields at t and $t-\Delta t$ are known. These wavefields are called snapshots, and are two-dimensional matrices in computer simulation. $\Delta t^2 v^2(x,z)\nabla^2$ requires Laplacian computation of the current wavefield. The five-point Laplacian, and nine-point Laplacian implement ∇^2 using second-order finite-difference operators and fourth-order finite-difference operators respectively.

Source locations are chosen by placing appropriate impulses in the two input wavefields, $\psi(x,z,t)$ and $\psi(x,z,t-\Delta t)$. At each receiver location $\psi(x,z,t)$ is computed using Equation (A.5), and samples are extracted to form the recorded traces. Using Equation (A.5) in time-stepping simulation, the amplitudes of the wavefield grow through time without bound under some circumstances, and certain stability conditions are needed. These conditions are

$$\frac{v_{\max}\Delta t}{\Delta x} \le \begin{cases} \dfrac{1}{\sqrt{2}} & 2^{nd} - order\,Laplacian \\ \\ \sqrt{\dfrac{3}{8}} & 4^{th} - order\,Laplacian. \end{cases} \tag{A.6}$$

Therefore, time and space sample rates are not chosen independently (Margrave, 2000).

APPENDIX B: INVERSION OF RAYLEIGH-WAVE FIRST HIGHER MODE DISPERSION CURVES OF PRIDDIS SEISMIC DATA FOR S-WAVE VELOCITIES

Using the MASW method, the Rayleigh-wave dispersion curves of the 1st higher mode, instead of the fundamental mode, are picked and inverted here for S-wave velocities. The data, used here, is part of Priddis seismic line shown earlier in Chapter Three of this thesis. The part used for this study is indicated by the blue segment (a-a') on the elevation profile shown in Figure B-1. A dispersion image of the shot gather, shown earlier in Figure 3-8, is created and shown in Figure B-2. Then, the dispersion curve of the 1st higher mode is picked and indicated by the blue squares on the dispersion image. This dispersion curve is inverted using an initial model indicated by the dashed blue line in Figure B-3. The solid blue line, in Figure B-3, shows the inversion results. Finally, a 2-D S-wave velocity profile is created and shown in Figure B-4.

In Chapter Three, another 2-D S-wave velocity profile was created from the inversion of the Rayleigh-wave fundamental-mode dispersion curves and shown in Figure 3-11. Comparing Figure B-4 and Figure 3-11, the velocity range is similar but the velocities are different. Surface-wave methods use the fundamental-mode dispersion curve for the inversion of S-wave velocities because this mode has more energy than the higher-order modes, and penetrates into the earth deeper than higher modes do. Therefore, we believe that S-wave velocities of Figure 3-11 are closer to the real S-wave velocities than those of Figure B-4.

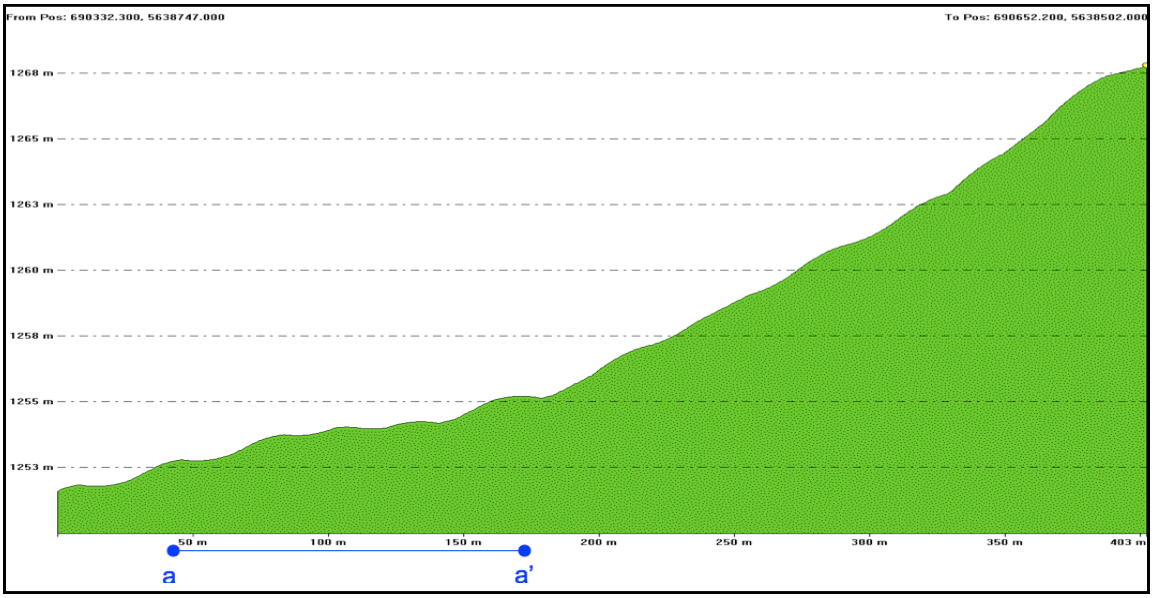

Figure B-1. Elevation profile. The blue line indicates the portion of the line, for which S-wave velocities will be profiled by the MASW method here.

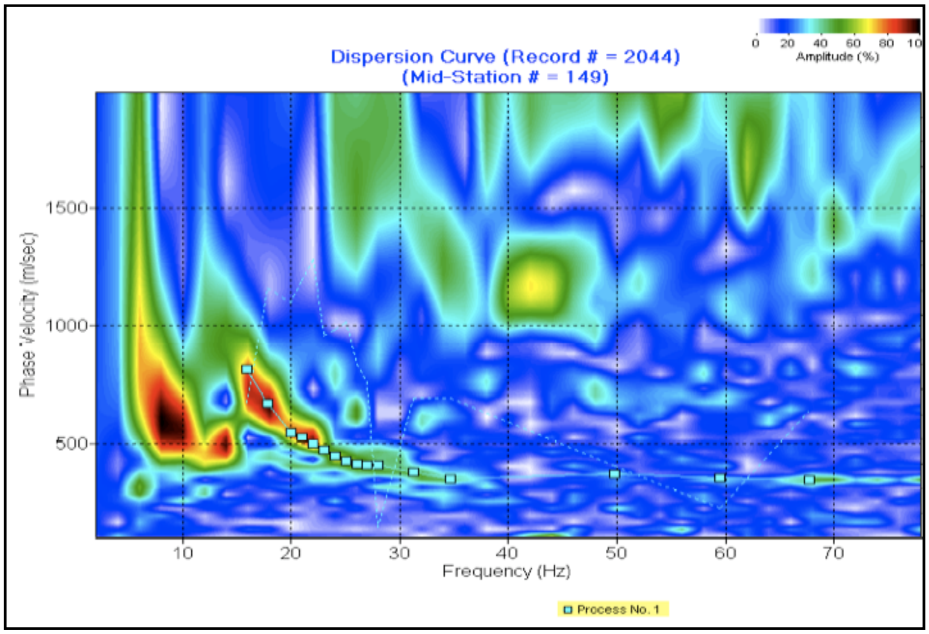

Figure B-2. Dispersion curve of the shot gather shown in Figure 3-8. First higher mode is picked and indicated by the light blue squares.

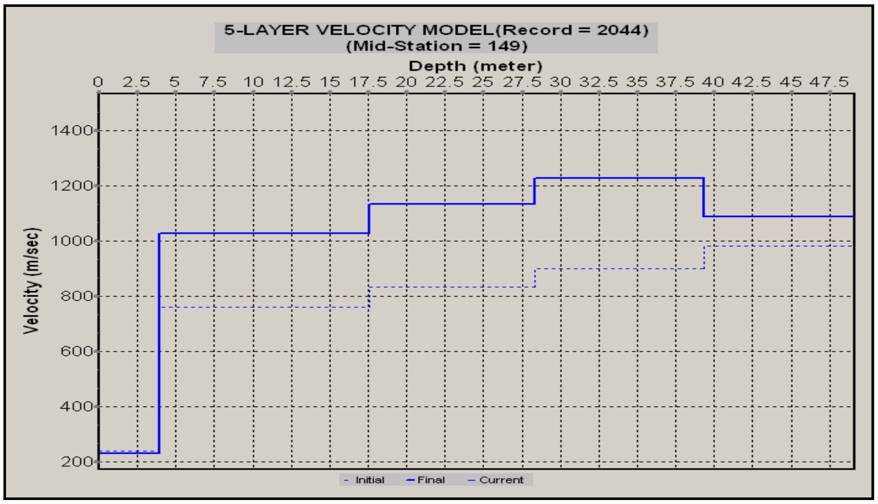

Figure B-3. Inverted S-wave velocity indicated by the solid blue and initial S-wave velocity indicated by the dashed blue line.

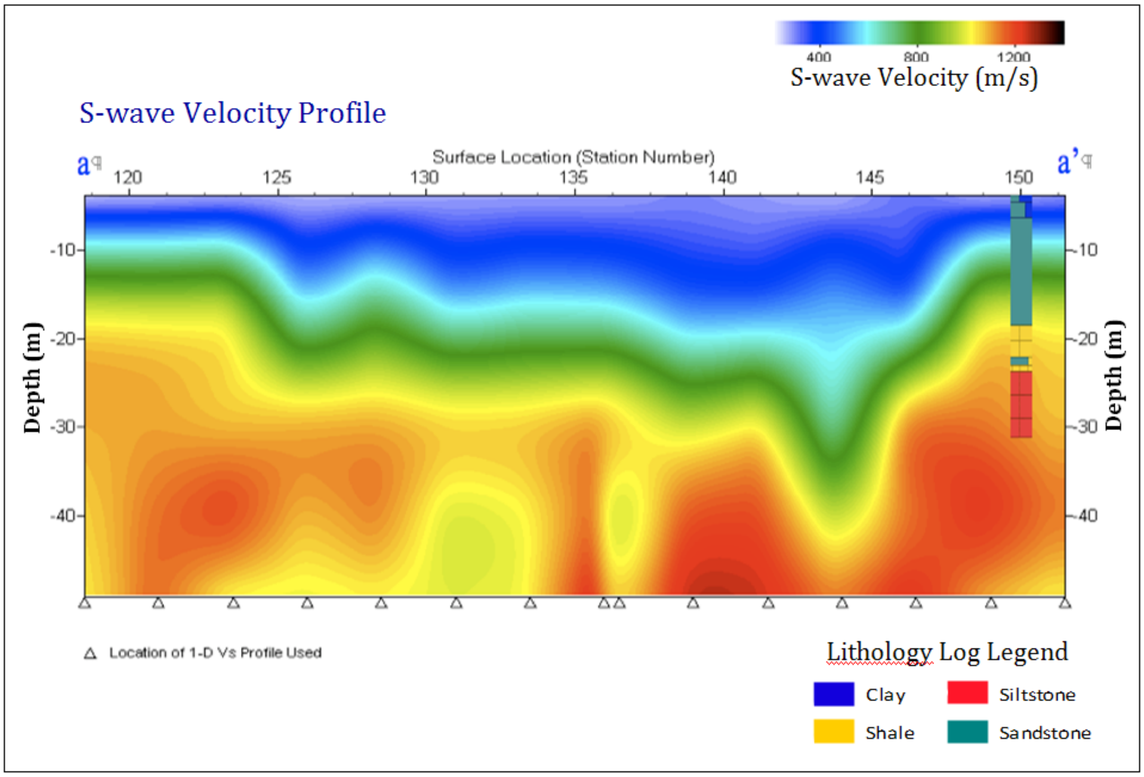

Figure B-4. S-wave velocity two-dimensional profile. The lithology log is inserted is at station number 150.

APPENDIX C: SENSITIVITY OF SPRING COULEE S-WAVE MASW ESTIMATES TO THE INITIAL MODEL

Different initial models are tested to examine the effect of the initial model on the inverted S-wave velocity model that is used for the static corrections. The effects of different velocities and various numbers of layers are tested. Only one parameter at a time is changed. The results are compared to each other and to the model shown in Figure 5-8.

First, the number of layers is changed with a constant S-wave velocity of 1300 m/s. Three-, 5-, 7-, 10-, and 20-layer initial models with constant S-wave velocity (1300 m/s) are shown in Figures C-1, C-2, C-3, C-4 and C-5 respectively. Models of fewer layers have coarser velocity grids as can be seen in Figures C-1, C-2, and C-3 where the numbers of layers are 3, 5, and 7 respectively. Figures C-4 and C-5 are very similar to Figure 5-8. For the 20-layer initial model, the fixed S-wave velocities were changed from 1300 m/s (Figure C-5) to 1600 m/s (Figure C-6) and 1000 m/s (Figure C-7). Using 1000 m/s and 1600 m/s for the initial model did not change the inversion results significantly. It appears that too few layers can influence the final result. However, given sufficient flexibility in the number of model layers (around 10), the velocity estimate in Figure 5-8 seems to be fairly stable.

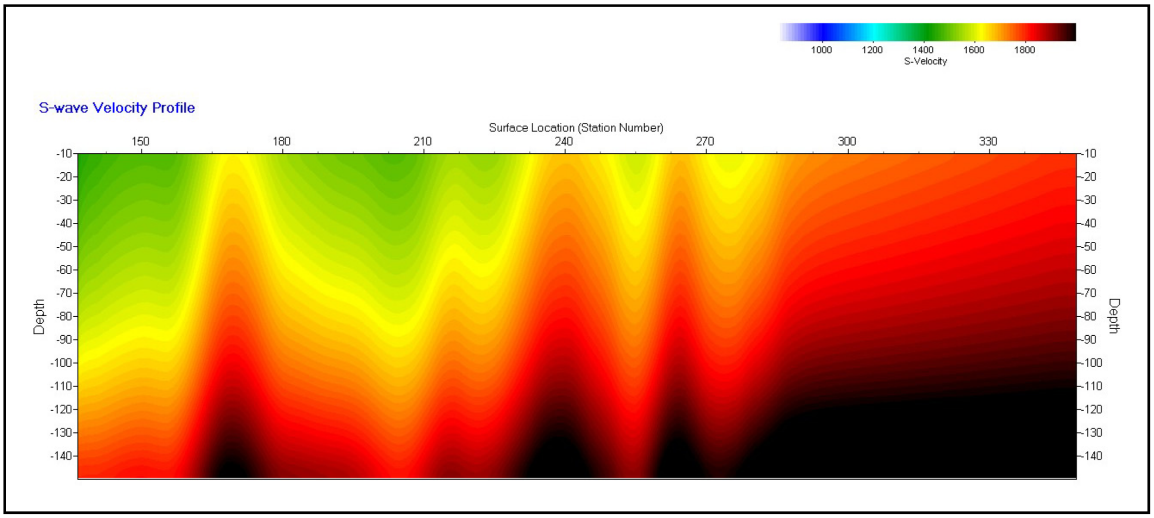

Figure C-1. MASW S-wave velocity model obtained by using 3-layer fixed initial velocity (~1300 m/s) model.

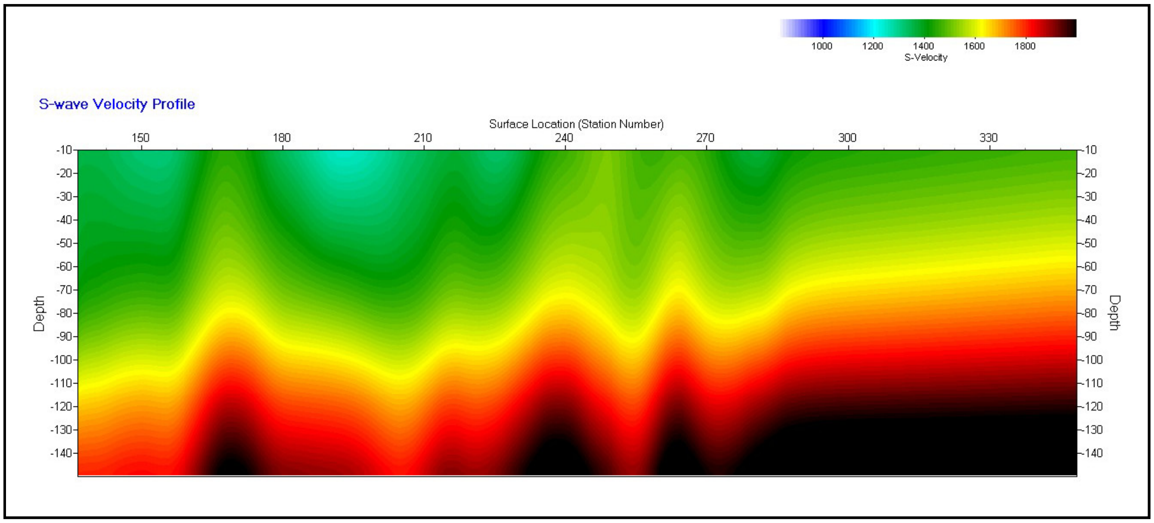

Figure C-2. MASW S-wave velocity model obtained by using 5-layer fixed initial velocity (~1300 m/s) model.

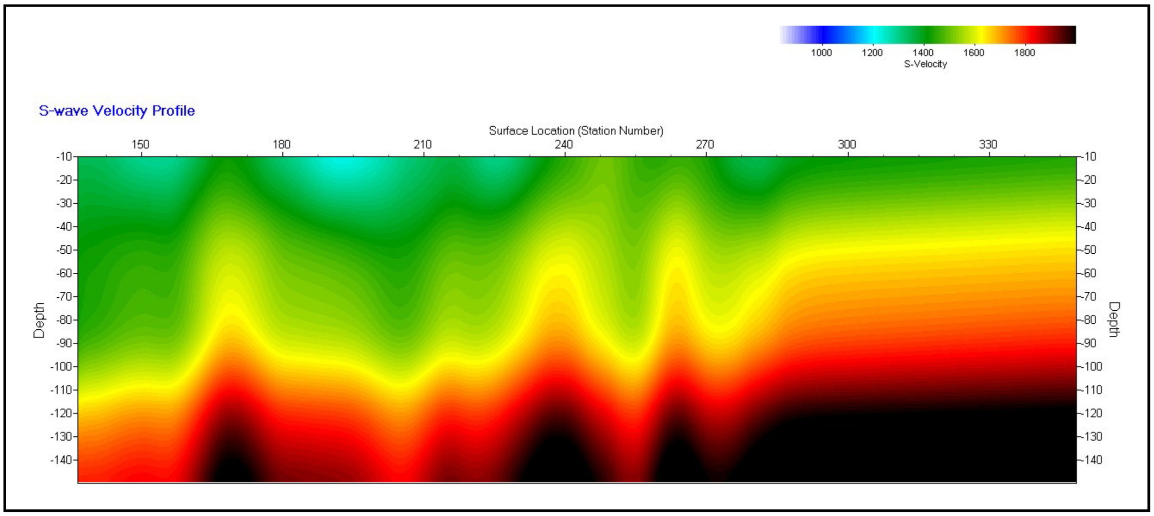

Figure C-3. MASW S-wave velocity model obtained by using 7-layer fixed initial velocity (~1300 m/s) model.

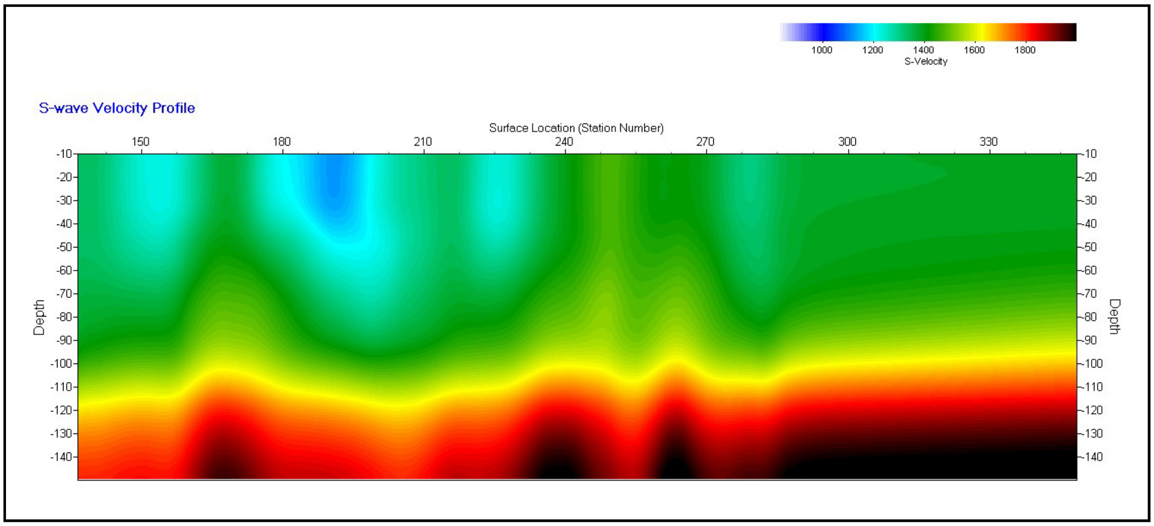

Figure C-4. MASW S-wave velocity model obtained by using 10-layer fixed initial velocity (~1300 m/s) model.

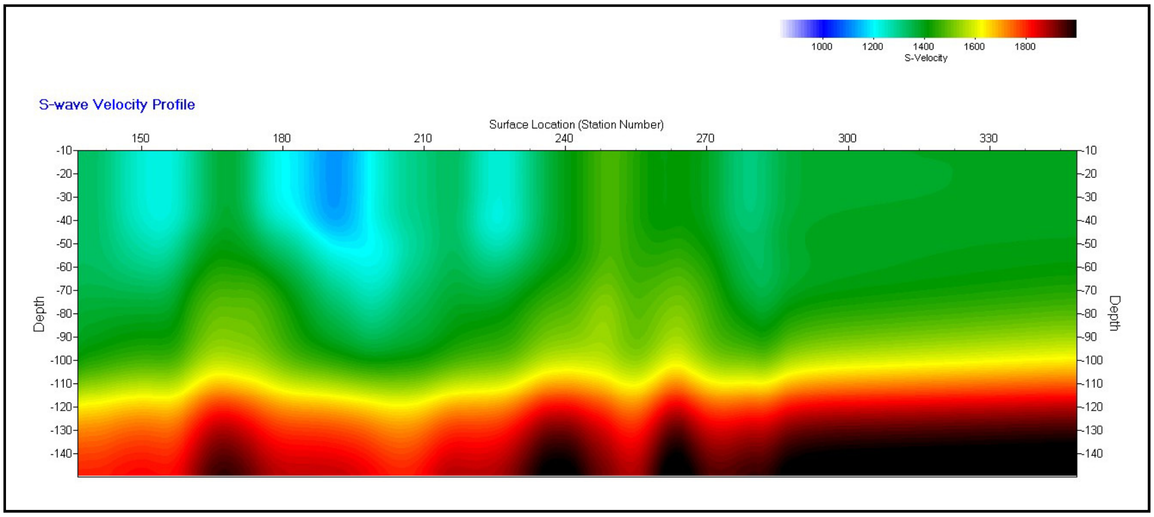

Figure C-5. MASW S-wave velocity model obtained by using 20-layer fixed initial velocity (~1300 m/s) model.

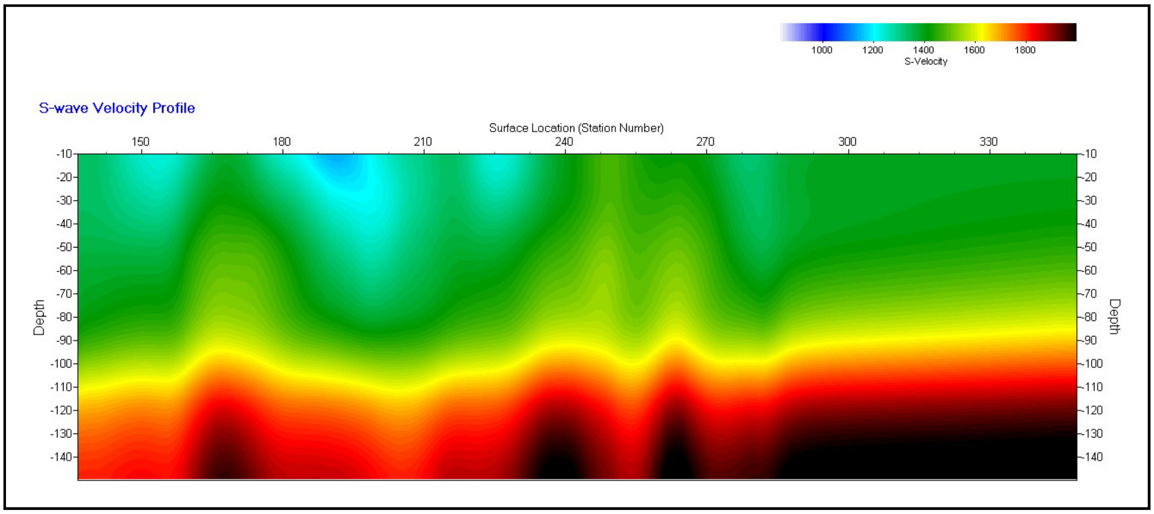

Figure C-6. MASW S-wave velocity model obtained by using 20-layer fixed initial velocity (~1600 m/s) model.

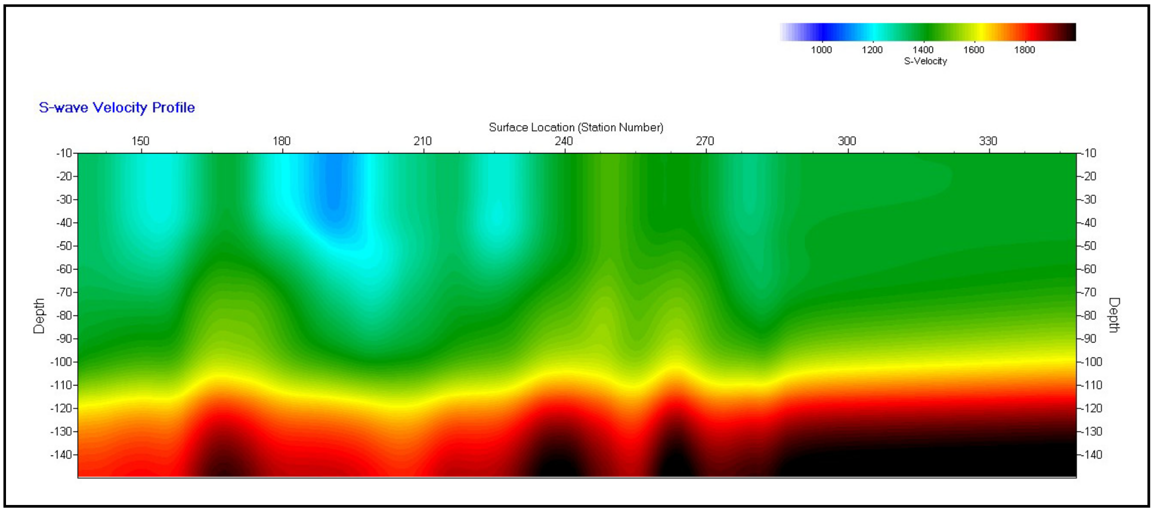

Figure C-7. MASW S-wave velocity model obtained by using 20-layer fixed initial velocity (~1000 m/s) model.

APPENDIX D: CALCULATION OF STATIC CORRECTIONS FROM MASW S-WAVE VELOCITY NEAR-SURFACE MODEL

Table D-1. Calculation of static corrections from the MASW S-wave velocity model, shown in Figure 5-8. Replacement velocity is 1966 m/s.

Station	Depth (m)	Thickness (m)	Velocity (m/s)	Time (s)	LVL Statics (ms)	Surface Elevation (m)	Elevation Statics (ms)	Total Datum Statics (ms)
136	10	10	420	0.02381				
136	13.08	3.08	1337.7	0.002303				
136	22.16	9.084	1337.4	0.006792				
136	33.52	11.354	1336.8	0.008493				
136	47.71	14.193	1337.1	0.010615				
136	65.45	17.741	1352.2	0.01312				
136	87.63	22.177	1377.1	0.016104				
136	115.3	27.72	1398.3	0.019824				
136	150	34.651	1637.7	0.021158	122.218	1087	133.722	11.504037
139	10	10	420	0.02381				
139	13.08	3.08	1337.9	0.002302				
139	22.16	9.084	1337.6	0.006791				
139	33.52	11.354	1336.6	0.008495				
139	47.71	14.193	1340.4	0.010588				
139	65.45	17.741	1367.3	0.012975				
139	87.63	22.177	1402.1	0.015816				
139	115.3	27.72	1448.2	0.019141				
139	150	34.651	1668.5	0.020768	120.687	1088	133.214	12.526998
142	10	10	420	0.02381				
142	13.08	3.08	1336.3	0.002305				
142	22.16	9.084	1336	0.006799				
142	33.52	11.354	1335.4	0.008502				
142	47.71	14.193	1343	0.010568				
142	65.45	17.741	1372.7	0.012924				
142	87.63	22.177	1408.9	0.01574				
142	115.3	27.72	1466	0.018908				
142	150	34.651	1672.9	0.020713	120.269	1089	132.705	12.435943
145	10	10	420	0.02381				
145	13.08	3.08	1296.8	0.002375				

145	22.16	9.084	1298	0.006999				
145	33.52	11.354	1305.1	0.0087				
145	47.71	14.193	1324.1	0.010719				
145	65.45	17.741	1369	0.012959				
145	87.63	22.177	1419.2	0.015627				
145	115.3	27.72	1479.2	0.01874				
145	150	34.651	1687.3	0.020537	120.464	1090	132.197	11.732627
148	10	10	420	0.02381				
148	13.08	3.08	1247.2	0.002469				
148	22.16	9.084	1249	0.007273				
148	33.52	11.354	1265	0.008975				
148	47.71	14.193	1300.1	0.010917				
148	65.45	17.741	1364.1	0.013006				
148	87.63	22.177	1427	0.015541				
148	115.3	27.72	1496.4	0.018524				
148	150	34.651	1707.8	0.02029	120.806	1091	131.688	10.882009
151	10	10	420	0.02381				
151	13.08	3.08	1219	0.002527				
151	22.16	9.084	1222.2	0.007432				
151	33.52	11.354	1244	0.009127				
151	47.71	14.193	1290.3	0.010999				
151	65.45	17.741	1360.1	0.013044				
151	87.63	22.177	1428.7	0.015522				
151	115.3	27.72	1497.1	0.018515				
151	150	34.651	1707.6	0.020293	121.269	1092	131.18	9.9105801
154	10	10	420	0.02381				
154	13.08	3.08	1213.2	0.002539				
154	22.16	9.084	1216.5	0.007467				
154	33.52	11.354	1237.8	0.009173				
154	47.71	14.193	1287.5	0.011024				
154	65.45	17.741	1360.1	0.013044				
154	87.63	22.177	1431.7	0.01549				
154	115.3	27.72	1498.6	0.018497				
154	150	34.651	1710.1	0.020263	121.305	1092	131.18	9.8747525
157	10	10	420	0.02381				
157	13.08	3.08	1211	0.002543				
157	22.16	9.084	1214.8	0.007478				
157	33.52	11.354	1234.5	0.009197				
157	47.71	14.193	1283.7	0.011056				

157	65.45	17.741	1354.1	0.013102				
157	87.63	22.177	1416.8	0.015653				
157	115.3	27.72	1481.5	0.018711				
157	150	34.651	1687.3	0.020537	122.086	1093	130.671	8.5852198
160	10	10	420	0.02381				
160	13.08	3.08	1251.3	0.002461				
160	22.16	9.084	1255	0.007238				
160	33.52	11.354	1293.9	0.008775				
160	47.71	14.193	1337.9	0.010608				
160	65.45	17.741	1400.3	0.01267				
160	87.63	22.177	1439.4	0.015407				
160	115.3	27.72	1501.1	0.018467				
160	150	34.651	1708.8	0.020277	119.713	1094	130.163	10.449651
163	10	10	420	0.02381				
163	13.08	3.08	1322.6	0.002329				
163	22.16	9.084	1327.8	0.006841				
163	33.52	11.354	1363.9	0.008325				
163	47.71	14.193	1413	0.010044				
163	65.45	17.741	1478.6	0.011998				
163	87.63	22.177	1521.3	0.014578				
163	115.3	27.72	1580.1	0.017543				
163	150	34.651	1800	0.019251	114.718	1095	129.654	14.93595
166	10	10	420	0.02381				
166	13.08	3.08	1374.5	0.002241				
166	22.16	9.084	1380.8	0.006579				
166	33.52	11.354	1411.7	0.008043				
166	47.71	14.193	1449.1	0.009794				
166	65.45	17.741	1485.1	0.011946				
166	87.63	22.177	1549.1	0.014316				
166	115.3	27.72	1624.1	0.017068				
166	150	34.651	1866.6	0.018564	112.361	1095	129.654	17.29376
169	10	10	420	0.02381				
169	13.08	3.08	1408.2	0.002187				
169	22.16	9.084	1413.6	0.006426				
169	33.52	11.354	1421.2	0.007989				
169	47.71	14.193	1454.6	0.009757				
169	65.45	17.741	1504.5	0.011792				
169	87.63	22.177	1552.3	0.014287				
169	115.3	27.72	1633	0.016975				

169	150	34.651	1900.4	0.018234	111.457	1096	129.146	17.688516
172	10	10	420	0.02381				
172	13.08	3.08	1383.7	0.002226				
172	22.16	9.084	1386.6	0.006551				
172	33.52	11.354	1395.2	0.008138				
172	47.71	14.193	1422.8	0.009975				
172	65.45	17.741	1468.6	0.012081				
172	87.63	22.177	1517.9	0.01461				
172	115.3	27.72	1603.8	0.017284				
172	150	34.651	1874.8	0.018483	113.157	1096	129.146	15.988948
175	10	10	420	0.02381				
175	13.08	3.08	1293.1	0.002382				
175	22.16	9.084	1302.7	0.006973				
175	33.52	11.354	1338.1	0.008485				
175	47.71	14.193	1408.8	0.010075				
175	65.45	17.741	1472.2	0.012051				
175	87.63	22.177	1511.9	0.014669				
175	115.3	27.72	1576.6	0.017582				
175	150	34.651	1827.1	0.018965	114.991	1097	128.638	13.646369
178	10	10	420	0.02381				
178	13.08	3.08	1212.4	0.00254				
178	22.16	9.084	1224.1	0.007421				
178	33.52	11.354	1276.7	0.008893				
178	47.71	14.193	1363.9	0.010406				
178	65.45	17.741	1445.3	0.012275				
178	87.63	22.177	1487.5	0.014909				
178	115.3	27.72	1546.5	0.017924				
178	150	34.651	1778.6	0.019482	117.661	1097	128.638	10.976364
181	10	10	420	0.02381				
181	13.08	3.08	1172.3	0.002627				
181	22.16	9.084	1188.7	0.007642				
181	33.52	11.354	1245.3	0.009117				
181	47.71	14.193	1329.6	0.010675				
181	65.45	17.741	1402	0.012654				
181	87.63	22.177	1448.6	0.015309				
181	115.3	27.72	1519.1	0.018248				
181	150	34.651	1745.4	0.019853	119.935	1098	128.129	8.1937511
184	10	10	420	0.02381				
184	13.08	3.08	1193.5	0.002581				

184	22.16	9.084	1203.6	0.007547				
184	33.52	11.354	1248.1	0.009097				
184	47.71	14.193	1307	0.01086				
184	65.45	17.741	1370.7	0.012943				
184	87.63	22.177	1431.9	0.015488				
184	115.3	27.72	1516.8	0.018276				
184	150	34.651	1760.6	0.019681	120.282	1099	127.621	7.3382023
187	10	10	420	0.02381				
187	13.08	3.08	1158.4	0.002659				
187	22.16	9.084	1168.4	0.007775				
187	33.52	11.354	1209	0.009391				
187	47.71	14.193	1268.5	0.011188				
187	65.45	17.741	1348.3	0.013158				
187	87.63	22.177	1416.9	0.015652				
187	115.3	27.72	1514.8	0.018299				
187	150	34.651	1761.4	0.019673	121.605	1099	127.621	6.0151331
190	10	10	420	0.02381				
190	13.08	3.08	1111.7	0.002771				
190	22.16	9.084	1118.6	0.008121				
190	33.52	11.354	1164	0.009754				
190	47.71	14.193	1230.8	0.011531				
190	65.45	17.741	1313.5	0.013506				
190	87.63	22.177	1407	0.015762				
190	115.3	27.72	1512	0.018333				
190	150	34.651	1759.6	0.019692	123.28	1100	127.112	3.8324739
193	10	10	420	0.02381				
193	13.08	3.08	1095.2	0.002812				
193	22.16	9.084	1102.4	0.00824				
193	33.52	11.354	1138.5	0.009972				
193	47.71	14.193	1207.7	0.011752				
193	65.45	17.741	1294.9	0.013701				
193	87.63	22.177	1393.5	0.015915				
193	115.3	27.72	1501.5	0.018462				
193	150	34.651	1754.8	0.019746	124.411	1101	126.604	2.1926235
196	10	10	420	0.02381				
196	13.08	3.08	1150.1	0.002678				
196	22.16	9.084	1155.9	0.007859				
196	33.52	11.354	1174	0.009671				
196	47.71	14.193	1222.8	0.011607				

196	65.45	17.741	1289.4	0.01376				
196	87.63	22.177	1382.9	0.016036				
196	115.3	27.72	1490.1	0.018603				
196	150	34.651	1745	0.019857	123.881	1102	126.095	2.2142301
199	10	10	420	0.02381				
199	13.08	3.08	1213.6	0.002538				
199	22.16	9.084	1218.1	0.007457				
199	33.52	11.354	1203.6	0.009433				
199	47.71	14.193	1214.9	0.011682				
199	65.45	17.741	1258.1	0.014102				
199	87.63	22.177	1358.2	0.016329				
199	115.3	27.72	1478	0.018755				
199	150	34.651	1726.5	0.02007	124.175	1103	125.587	1.4118531
202	10	10	420	0.02381				
202	13.08	3.08	1259.5	0.002445				
202	22.16	9.084	1259.8	0.007211				
202	33.52	11.354	1237	0.009178				
202	47.71	14.193	1238.2	0.011463				
202	65.45	17.741	1276.1	0.013902				
202	87.63	22.177	1362	0.016282				
202	115.3	27.72	1466.2	0.018906				
202	150	34.651	1704.6	0.020328	123.526	1103	125.587	2.0612847
205	10	10	420	0.02381				
205	13.08	3.08	1283.9	0.002399				
205	22.16	9.084	1281.7	0.007088				
205	33.52	11.354	1260	0.009011				
205	47.71	14.193	1258.1	0.011281				
205	65.45	17.741	1307.3	0.013571				
205	87.63	22.177	1378.4	0.016089				
205	115.3	27.72	1455.6	0.019043				
205	150	34.651	1679.3	0.020634	122.926	1104	125.078	2.152693
208	10	10	420	0.02381				
208	13.08	3.08	1317.9	0.002337				
208	22.16	9.084	1314.4	0.006911				
208	33.52	11.354	1311.7	0.008656				
208	47.71	14.193	1323.2	0.010727				
208	65.45	17.741	1346.8	0.013173				
208	87.63	22.177	1393.1	0.015919				
208	115.3	27.72	1463.9	0.018936				

208	150	34.651	1680.4	0.020621	121.089	1105	124.57	3.4811719
211	10	10	420	0.02381				
211	13.08	3.08	1310.5	0.00235				
211	22.16	9.084	1308.3	0.006943				
211	33.52	11.354	1306.4	0.008691				
211	47.71	14.193	1319.1	0.01076				
211	65.45	17.741	1348.1	0.01316				
211	87.63	22.177	1396.5	0.015881				
211	115.3	27.72	1475.1	0.018792				
211	150	34.651	1715.2	0.020203	120.589	1107	123.553	2.9637061
214	10	10	420	0.02381				
214	13.08	3.08	1340.7	0.002297				
214	22.16	9.084	1339.6	0.006781				
214	33.52	11.354	1340.5	0.00847				
214	47.71	14.193	1350	0.010513				
214	65.45	17.741	1371.6	0.012935				
214	87.63	22.177	1423.4	0.01558				
214	115.3	27.72	1514.9	0.018298				
214	150	34.651	1774.5	0.019528	118.212	1107	123.553	5.3409887
217	10	10	420	0.02381				
217	13.08	3.08	1352.8	0.002277				
217	22.16	9.084	1352.6	0.006716				
217	33.52	11.354	1355.2	0.008378				
217	47.71	14.193	1366.3	0.010388				
217	65.45	17.741	1394.5	0.012723				
217	87.63	22.177	1447.2	0.015324				
217	115.3	27.72	1540	0.018				
217	150	34.651	1798.2	0.019269	116.884	1108	123.045	6.1601239
220	10	10	420	0.02381				
220	13.08	3.08	1333.1	0.00231				
220	22.16	9.084	1328	0.00684				
220	33.52	11.354	1334	0.008511				
220	47.71	14.193	1350.1	0.010513				
220	65.45	17.741	1394	0.012727				
220	87.63	22.177	1451.6	0.015278				
220	115.3	27.72	1537.5	0.01803				
220	150	34.651	1770.7	0.019569	117.588	1109	122.536	4.9480388
223	10	10	420	0.02381				
223	13.08	3.08	1249.2	0.002466				

223	22.16	9.084	1244.4	0.0073				
223	33.52	11.354	1259.9	0.009012				
223	47.71	14.193	1300.9	0.01091				
223	65.45	17.741	1373.4	0.012917				
223	87.63	22.177	1447.6	0.01532				
223	115.3	27.72	1526.3	0.018161				
223	150	34.651	1748.7	0.019816	119.711	1109	122.536	2.8255834
226	10	10	420	0.02381				
226	13.08	3.08	1202.3	0.002562				
226	22.16	9.084	1196.8	0.007591				
226	33.52	11.354	1217.1	0.009329				
226	47.71	14.193	1283.7	0.011056				
226	65.45	17.741	1370.1	0.012949				
226	87.63	22.177	1453.4	0.015259				
226	115.3	27.72	1531.4	0.018102				
226	150	34.651	1768	0.019599	120.256	1109	122.536	2.2804386
229	10	10	420	0.02381				
229	13.08	3.08	1222.4	0.00252				
229	22.16	9.084	1223.8	0.007423				
229	33.52	11.354	1244.7	0.009122				
229	47.71	14.193	1309.2	0.010841				
229	65.45	17.741	1384.9	0.012811				
229	87.63	22.177	1457.9	0.015212				
229	115.3	27.72	1544	0.017954				
229	150	34.651	1797.2	0.019281	118.972	1110	122.028	3.0560749
232	10	10	420	0.02381				
232	13.08	3.08	1288.3	0.002391				
232	22.16	9.084	1291.1	0.007036				
232	33.52	11.354	1306	0.008694				
232	47.71	14.193	1354.1	0.010481				
232	65.45	17.741	1419.5	0.012498				
232	87.63	22.177	1488.7	0.014897				
232	115.3	27.72	1589.7	0.017437				
232	150	34.651	1860.4	0.018626	115.87	1111	121.519	5.649355
235	10	10	420	0.02381				
235	13.08	3.08	1343	0.002293				
235	22.16	9.084	1346.6	0.006746				
235	33.52	11.354	1355.7	0.008375				
235	47.71	14.193	1389.2	0.010216				

235	65.45	17.741	1451.6	0.012222				
235	87.63	22.177	1523.9	0.014552				
235	115.3	27.72	1624.5	0.017064				
235	150	34.651	1886.4	0.018369	113.648	1111	121.519	7.8717015
238	10	10	420	0.02381				
238	13.08	3.08	1383.3	0.002227				
238	22.16	9.084	1385.5	0.006556				
238	33.52	11.354	1392.6	0.008153				
238	47.71	14.193	1416.9	0.010017				
238	65.45	17.741	1471.1	0.01206				
238	87.63	22.177	1552	0.014289				
238	115.3	27.72	1660.6	0.016693				
238	150	34.651	1940.4	0.017858	111.663	1111	121.519	9.8565098
241	10	10	420	0.02381				
241	13.08	3.08	1420.5	0.002168				
241	22.16	9.084	1421.8	0.006389				
241	33.52	11.354	1426.1	0.007961				
241	47.71	14.193	1443.3	0.009834				
241	65.45	17.741	1484.6	0.01195				
241	87.63	22.177	1547	0.014336				
241	115.3	27.72	1643	0.016871				
241	150	34.651	1917.9	0.018067	111.386	1111	121.519	10.132745
244	10	10	420	0.02381				
244	13.08	3.08	1428	0.002157				
244	22.16	9.084	1428.8	0.006358				
244	33.52	11.354	1433.5	0.00792				
244	47.71	14.193	1451.7	0.009777				
244	65.45	17.741	1485.8	0.011941				
244	87.63	22.177	1543.4	0.014369				
244	115.3	27.72	1638.8	0.016915				
244	150	34.651	1900.1	0.018236	111.483	1112	121.011	9.5279854
247	10	10	420	0.02381				
247	13.08	3.08	1474.4	0.002089				
247	22.16	9.084	1475	0.006159				
247	33.52	11.354	1479	0.007677				
247	47.71	14.193	1495.3	0.009492				
247	65.45	17.741	1527.4	0.011615				
247	87.63	22.177	1540.8	0.014393				
247	115.3	27.72	1591.5	0.017418				

247	150	34.651	1800.4	0.019246	111.898	1113	120.502	8.6044415
250	10	10	420	0.02381				
250	13.08	3.08	1497.6	0.002057				
250	22.16	9.084	1498.6	0.006062				
250	33.52	11.354	1502.3	0.007558				
250	47.71	14.193	1516.3	0.009361				
250	65.45	17.741	1545.7	0.011477				
250	87.63	22.177	1545.1	0.014353				
250	115.3	27.72	1586.5	0.017472				
250	150	34.651	1795.5	0.019298	111.447	1114	119.994	8.5466516
253	10	10	420	0.02381				
253	13.08	3.08	1490	0.002067				
253	22.16	9.084	1489.8	0.006097				
253	33.52	11.354	1492.5	0.007607				
253	47.71	14.193	1498.5	0.009471				
253	65.45	17.741	1515.2	0.011709				
253	87.63	22.177	1511.7	0.01467				
253	115.3	27.72	1543.2	0.017963				
253	150	34.651	1773.6	0.019537	112.932	1115	119.485	6.5535497
256	10	10	420	0.02381				
256	13.08	3.08	1430.3	0.002153				
256	22.16	9.084	1429.7	0.006354				
256	33.52	11.354	1431.6	0.007931				
256	47.71	14.193	1437.8	0.009871				
256	65.45	17.741	1450.9	0.012227				
256	87.63	22.177	1476.1	0.015024				
256	115.3	27.72	1522.6	0.018206				
256	150	34.651	1733.1	0.019994	115.57	1115	119.485	3.915632
259	10	10	420	0.02381				
259	13.08	3.08	1407.8	0.002188				
259	22.16	9.084	1406.7	0.006457				
259	33.52	11.354	1420.2	0.007995				
259	47.71	14.193	1444.2	0.009827				
259	65.45	17.741	1472.6	0.012047				
259	87.63	22.177	1505.9	0.014727				
259	115.3	27.72	1564.1	0.017723				
259	150	34.651	1792.4	0.019332	114.106	1116	118.977	4.8706442
262	10	10	420	0.02381				
262	13.08	3.08	1390.5	0.002215				

262	22.16	9.084	1391.5	0.006528				
262	33.52	11.354	1408.9	0.008059				
262	47.71	14.193	1446.9	0.009809				
262	65.45	17.741	1504.5	0.011792				
262	87.63	22.177	1574.8	0.014082				
262	115.3	27.72	1664.6	0.016653				
262	150	34.651	1930.9	0.017945	110.892	1117	118.469	7.5761446
265	10	10	420	0.02381				
265	13.08	3.08	1418.5	0.002171				
265	22.16	9.084	1421	0.006393				
265	33.52	11.354	1436.9	0.007902				
265	47.71	14.193	1475.2	0.009621				
265	65.45	17.741	1522.9	0.01165				
265	87.63	22.177	1599.1	0.013868				
265	115.3	27.72	1698.2	0.016323				
265	150	34.651	1966.8	0.017618	109.355	1117	118.469	9.1131258
268	10	10	420	0.02381				
268	13.08	3.08	1416.8	0.002174				
268	22.16	9.084	1420	0.006397				
268	33.52	11.354	1427.8	0.007952				
268	47.71	14.193	1464.7	0.00969				
268	65.45	17.741	1505.9	0.011781				
268	87.63	22.177	1563	0.014188				
268	115.3	27.72	1644	0.016861				
268	150	34.651	1913.3	0.018111	110.964	1119	117.452	6.4875329
271	10	10	420	0.02381				
271	13.08	3.08	1395.4	0.002207				
271	22.16	9.084	1397.3	0.006501				
271	33.52	11.354	1405	0.008081				
271	47.71	14.193	1428.4	0.009936				
271	65.45	17.741	1456.8	0.012178				
271	87.63	22.177	1494.1	0.014843				
271	115.3	27.72	1565.9	0.017702				
271	150	34.651	1814.5	0.019096	114.355	1120	116.943	2.5884084
274	10	10	420	0.02381				
274	13.08	3.08	1357.9	0.002268				
274	22.16	9.084	1359.5	0.006682				
274	33.52	11.354	1375.4	0.008255				
274	47.71	14.193	1402	0.010124				

274	65.45	17.741	1430.9	0.012399				
274	87.63	22.177	1464	0.015148				
274	115.3	27.72	1560.9	0.017758				
274	150	34.651	1812.7	0.019116	115.559	1121	116.435	0.8754166
277	10	10	420	0.02381				
277	13.08	3.08	1299.2	0.002371				
277	22.16	9.084	1300.8	0.006983				
277	33.52	11.354	1316.1	0.008627				
277	47.71	14.193	1338.8	0.010601				
277	65.45	17.741	1390.7	0.012757				
277	87.63	22.177	1468.1	0.015106				
277	115.3	27.72	1575.6	0.017593				
277	150	34.651	1842.4	0.018808	116.655	1120	116.943	0.2882329
280	10	10	420	0.02381				
280	13.08	3.08	1294.7	0.002379				
280	22.16	9.084	1297.9	0.006999				
280	33.52	11.354	1310.2	0.008666				
280	47.71	14.193	1326.6	0.010699				
280	65.45	17.741	1375.6	0.012897				
280	87.63	22.177	1468.1	0.015106				
280	115.3	27.72	1592.7	0.017405				
280	150	34.651	1873.4	0.018496	116.456	1121	116.435	-0.021161
283	10	10	420	0.02381				
283	13.08	3.08	1305.1	0.00236				
283	22.16	9.084	1309	0.00694				
283	33.52	11.354	1315.5	0.008631				
283	47.71	14.193	1324.5	0.010716				
283	65.45	17.741	1372.8	0.012923				
283	87.63	22.177	1459.1	0.0152				
283	115.3	27.72	1596	0.017369				
283	150	34.651	1901.9	0.018219	116.166	1121	116.435	0.2688499
286	10	10	420	0.02381				
286	13.08	3.08	1345.6	0.002289				
286	22.16	9.084	1349.4	0.006732				
286	33.52	11.354	1353.8	0.008386				
286	47.71	14.193	1343.3	0.010566				
286	65.45	17.741	1368.4	0.012965				
286	87.63	22.177	1443.8	0.01536				
286	115.3	27.72	1578.2	0.017565				

286	150	34.651	1882	0.018411	116.084	1123	115.418	-0.666645
287	10	10	420	0.02381				
287	13.08	3.08	1368.4	0.002251				
287	22.16	9.084	1371.2	0.006625				
287	33.52	11.354	1376.3	0.00825				
287	47.71	14.193	1375.1	0.010321				
287	65.45	17.741	1410	0.012582				
287	87.63	22.177	1493.1	0.014853				
287	115.3	27.72	1626.7	0.017041				
287	150	34.651	1938.5	0.017875	113.607	1123	115.418	1.8109326
288	10	10	420	0.02381				
288	13.08	3.08	1383.2	0.002227				
288	22.16	9.084	1385.1	0.006559				
288	33.52	11.354	1390.5	0.008165				
288	47.71	14.193	1394.1	0.01018				
288	65.45	17.741	1430.4	0.012403				
288	87.63	22.177	1527.3	0.01452				
288	115.3	27.72	1666.6	0.016633				
288	150	34.651	1944	0.017824	112.32	1123	115.418	3.0976159